Universidad de Concepción
Facultad de Ciencias Físicas y Matemáticas
Departamento de Física

Caracterización de regiones de formación estelar de alta masa: G353, L1482, y Vela

Tesis presentada por Rodrigo Hernán Álvarez Gutiérrez
al Departamento de Astronomía para obtener
el grado de Doctor en Física

Profesora Guía: Amelia Stutz
Comisión: Roberto Galván-Madrid
Rodrigo Herrera-Camus
Rodrigo Reeves

2024

Departamento de Física

Acknowledgement

I thank my family, friends, and professors for all of their support during these years. Specifically, without my family I wouldn't be here.

Resumen

El campo de la formación estelar a alta masa aún no es entendido del todo. Procesos tales como campos magnéticos, feedback estelar, e intrincados campos de velocidad agregan complejidad a la caracterización de estas regiones. Observatorios como ALMA, APEX, y el 30m de IRAM nos permiten acceder a escalas espaciales y espectrales pequeñas. En este contexto redujimos las observaciones de N_2H^+ de las 15 regiones del large program ALMA-IMF, y nos enfocamos en el análisis de la cinemática del gas denso del protocúmulo G353.41. Esta región está a una distancia de $\sim 2\,$kpc, arraigado en un filamento de gran escala ($\sim 8\,$pc) y con una masa $\sim 2.5 \times 10^3\,M_\odot$ en 1.3×1.3 pc^2. Extrajimos la componente aislada de la emisión de N_2H^+ y ajustamos tres componentes de velocidad Gaussianas para identificar estructuras a escalas pequeñas. Identificamos varios gradientes de velocidad a escalas grandes ($\sim 1\,$pc) y pequeñas($\sim$0.2 pc). Medimos nueve pares convergentes de gradientes de velocidad (VGs) los cuales llamamos "V-shapes" ($\sim 20\,$km s^{-1} pc^{-1}). Estos están en su mayoría localizados en filamentos y algunos están asociados a cores en el punto de convergencia. Interpretamos estos V-shapes como movimientos del gas hacia regiones mas densas, alimentando a los cores situados en la cercanía. Estimamos los tiempos asociados a estos V-shapes como VG^{-1}. Estos tiempos son de alrededor de 67 kyr. Derivamos la taza de acreción de masa en estas estructuras, estando en el rango de $(0.35 - 8.77) \times 10^{-4}$ $M_\odot$ yr^{-1}. Estos movimientos del gas conlleva al colapso del filamento y la formación de nuevos cores. Sugerimos que el protocúmulo está colapsando a escalas grandes, pero la velocidad de colapso es mas lenta en comparación a solo caída libre. Por lo tanto, estos datos son consistentes con que el protocúmulo está bajo una contracción gravitatoria y rápida formación de cores dentro del mismo. Esto sugiere la formación de múltiples generaciones de estrellas a lo largo de la vida del protocúmulo. También analizamos la cinemática de las regiones L1482 south y Vela, dos sistemas masivos filamentarios dentro de 1 kpc. Tanto HCO^+ como $C^{18}O$ presentan emisión a escalas grandes, ambas con una discontinuidad en la posición del cúmulo NGC 1579. El campo de velocidad de ambos trazadores presenta múltiple gradientes de velocidad ("V-shapes"), siendo estos posibles indicadores de colapso gravitacional producto de movimientos del gas a escalas pequeñas hacia zonas mas densas. Esto también lo vemos en Vela, donde estos movimientos son a lo largo del filamento. Medimos el perfil de linea de masa de Vela y del filamento que contiene al protocúmulo G353. Vemos que el perfil de vela está ubicado en el medio de nuestro diagrama, entre estructuras en Orión, mientras que el filamento G353 tiene el perfil mas alto de nuestra muestra. Posiblemente las regiones ubicadas en la parte de arriba o abajo nuestro diagrama son jóvenes o presentan formación estelar muy ineficientes, y a medida que estas regiones forman estrellas, sus perfiles se mueven al medio de la distribución.

Abstract

High mass star formation is a field not yet fully understood. Processes such as magnetic fields, stellar feedback, and intricate velocity fields add complexity to the characterization of these environments. Instruments such as ALMA, APEX, and the IRAM 30m allow us to access small spatial and spectral scales. In this work we analyze data obtained using these facilities with the goal to characterize massive star forming structures. In this context we imaged the N_2H^+ observations of all 15 ALMA-IMF Large Program regions, and then we focused on the analysis of the dense gas kinematics of the G353.41 protocluster, with a spatial resolution of ~ 0.02 pc. G353.41, at a distance of ~ 2 kpc, is embedded in a larger-scale ($\sim$ 8 pc) filament and has a mass of $\sim 2.5 \times 10^3$ $M_\odot$ within 1.3×1.3 pc^2. We extracted the N_2H^+ (1−0) isolated line component and decomposed it by fitting up to three Gaussian velocity components to identify velocity structures at small scales. We measured nine converging "V-shaped" velocity gradients (VGs; $\sim 20\,\mathrm{km\,s^{-1}\,pc^{-1}}$) that are well resolved (sizes $\sim$ 0.1 pc), mostly located in filaments, which are sometimes associated with cores near their point of convergence. We interpret these V-shapes as inflowing gas feeding the regions near cores. The timescales associated with the V-shapes is VG^{-1}, and we interpret them as inflow timescales, with an average inflow timescale of $\sim$ 67 kyr. We derived mass accretion rates in the range of $(0.35 - 8.77) \times 10^{-4}$ $M_\odot$ yr^{-1}. We suggest that the protocluster is collapsing on large scales, but the velocity signature of collapse is slow compared to pure free-fall. Thus, these data are consistent with a comparatively slow global protocluster contraction under gravity, and faster core formation within, suggesting the formation of multiple generations of stars over the protocluster's lifetime. We also analyze the kinematic of the L1482 south and Vela regions, two massive filamentary systems within 1 kpc. In L1482 we detect in both HCO^+ and $C^{18}O$ present large scale emission with a common discontinuity at the location of the NGC 1579 star cluster. In the velocity field of both tracers there are multiple V-shapes which might indicate the presence of small scale gas flows along the filament towards denser regions. These V-shapes are also present in our APEX data of Vela, where these features are present along the filament. We increased the line-mass profiles sample by analyzing the mass distribution of Vela and the G353 parent filament. We see that the line-mass profile of Vela is located at the middle of our diagram, between structures in Orion, while the parent filament of G353 has the largest M/L profile from the probed environments. This suggest that regions located at the top (G353) or bottom (L1482) of this diagram are young or present an inefficient star formation rate, possible moving towards the middle of this diagram as they evolve.

Contents

List of Tables

List of Figures

Chapter 1

Introduction

High mass star formation environments host complex dynamical processes such as turbulence, feedback, magnetic fields, intricate velocity fields, among others (Álvarez-Gutiérrez et al., 2021; Fissel et al., 2019; González Lobos & Stutz, 2019; Soler, 2019; Stutz & Gould, 2016). This complexity makes these regions hard to model given the high compute power required, where the results do not capture velocity fields seen in the data, such as wave-like oscillations, the slingshot mechanism, or filamentary rotation (Álvarez-Gutiérrez et al., 2021; González Lobos & Stutz, 2019; Liu et al., 2019; Stutz & Gould, 2016). In order to study high mass star formation we are required to probe small spatial scales which are only accessible by characterizing Galactic environments. Facilities such as ALMA, APEX, and the IRAM 30m allow highly precise measurements of the velocities of stellar objects as well as the gas kinematics. In our galaxy we know from Miville-Deschênes et al. (2017) that the mass distribution of molecular clouds peaks at $\sim 10^5\,M_\odot$, suggesting that this mass value is ideal (most common) to study high mass star formation (Fig. 1.1). A few massive Galactic star forming regions that comply with the requirements presented above are the G353 filament, California, and the Vela molecular cloud (Álvarez-Gutiérrez et al., 2021, 2024; Fissel et al., 2019; Hill et al., 2011; Lada et al., 2017, 2010; Motte et al., 2022). In this thesis we analyze the mass distribution and kinematics of these environments.

The California and Vela molecular clouds host star clusters while the G353 filament hosts an embedded cluster. While star clusters have been studied extensively over many decades at comparatively short wavelengths, their precursors, protoclusters, have not been studied in depth until recently. Protoclusters (or embedded clusters) are the gas-dominated maternal environments in which star clusters are born and whose stellar constituents will ultimately populate the field of our Galaxy. Protoclusters are distinct entities from star clusters. Both are defined as relatively compact configurations in which the gravity is strong enough to influence the dynamics of their constituents. But in the latter, there is little to no gas, and the gravity of the cluster is dominated by the stars themselves. In protoclusters, in contrast, gravity is dominated by the cold gas in which the stars themselves are forming (Csengeri et al., 2017; Motte et al., 2018; Stutz, 2018; Stutz & Gould, 2016). Protoclusters are more accessible now than ever before thanks to ALMA and its exquisitely high-resolution interferometric millimeter-wave data tracing the cold gas in which the stars form (Liu et al., 2020a; Motte et al., 2022; Sanhueza

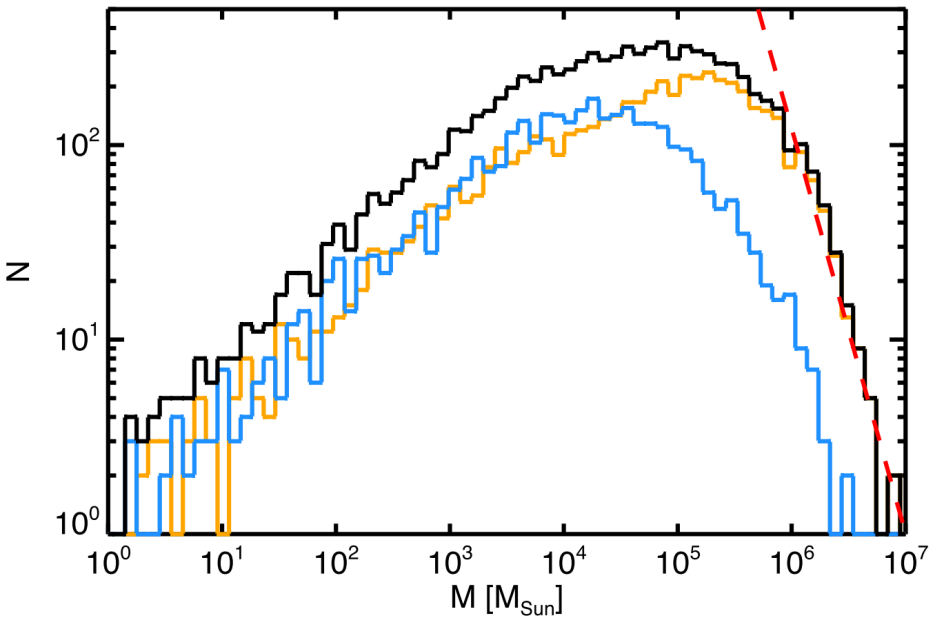

Figure 1.1: Histogram of the masses of Galactic molecular clouds. The distribution peaks at $\sim 10^5\,M_\odot$. Figure from Miville-Deschênes et al. (2017).

et al., 2019). Inside protoclusters, we witness the ongoing conversion of gas into compact and extremely dense stars, a process mediated by gas filaments (Álvarez-Gutiérrez et al., 2021; González Lobos & Stutz, 2019; Stutz, 2018) feeding gas structures called "cores" (André et al., 2010; Kuznetsova et al., 2015, 2018; Stutz & Kainulainen, 2015). Cores are compact gas mass concentrations, often defined to be of a size matching the resolution limit of the observations. In this case, we define cores to be in the order $\sim$ 2 kau.

These environments can be characterized in multiple ways by studying their constituent parts such as the stars and YSO population, gas kinematics, as well as their dust mass distribution (Álvarez-Gutiérrez et al., 2021, 2024; González Lobos & Stutz, 2019; Reyes-Reyes et al., 2024; Stutz, 2018; Stutz & Gould, 2016; Stutz & Kainulainen, 2015). A recent technique to analyze the velocity field in star forming environments was presented in González Lobos & Stutz (2019). This approach consists in modeling the gas radial velocities to then create position-velocity (PV) diagrams where the color of each point represents their integrated intensity. In Fig. 1.2 we see the striking difference between the traditional (left) and intensity-weighted (right) methods for the L1482 filament (Álvarez-Gutiérrez et al., 2021). The traditional technique consists on collapsing a spatial axis by estimating the total or average intensity. This results in diagrams that capture the large scale velocity distribution while loosing the details of the small scale structures. The intensity weighted PV technique removes the noise, recovers the small scale distributions, while maintaining the large scale velocity field of the region. As presented in previous work Álvarez-Gutiérrez et al. (2021, 2024); González Lobos & Stutz (2019), this approach allow the clear identification of small scale structures. As we present in Álvarez-Gutiérrez

et al. (2024), structures identified in the intensity-weighted PV diagrams, such as the V-shapes, appear to be signatures of gas flows that might increase the star formation activity in a region.

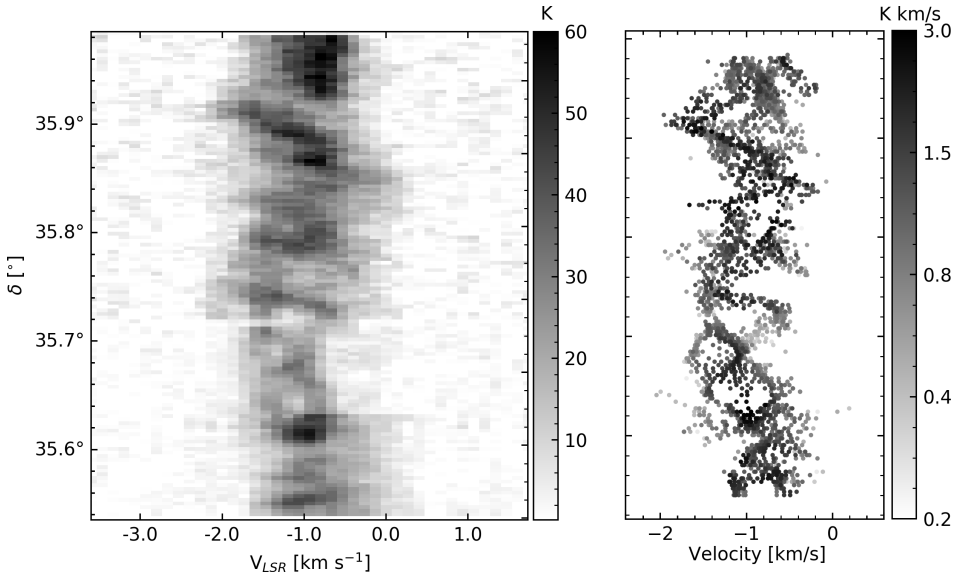

Figure 1.2: Position-velocity diagrams of the $C^{18}O$ L1482 data. **Left:** Traditional PV diagram obtained by taking the average value along one spatial axis, in this case right ascension. We observe large scale structure but these are hard to identify given the low visual clarity from this approach. **Right:** Intensity-weighted PV diagram. First we model the $C^{18}O$ emission using Gaussians, from which we then derive their integrated intensities, indicated by the color of each point. From the fitting we also obtain the centroid velocity which is displayed along the horizontal axis. Compared to the left panel we see a noticeable improvement regarding visual clarity given that noise is removed in the fitting process.

By estimating the line-mass (M/L) profile of multiple filamentary structures we are able to compare them in terms of density and possible evolutionary state. In papers such as Álvarez-Gutiérrez et al. (2021); Reyes-Reyes et al. (2024); Stutz & Gould (2016) they measure the M/L profile of a variety of structures in Orion, as well as the L1482 and G351.77 filaments, probing different mass ranges as well as star formation activity. As presented later in this thesis (see § 4.3) we measure the line mass (M/L) profile of the filament hosting the G353.41 protocluster as well as the Vela region. These profiles are presented in Fig. 1.3. We see that the regions at the top are the filament hosting massive protoclusters, where active star formation has not yet started. At the middle of the diagram there are regions where star formation is active, while at the bottom the L1482 filament is less dense and presents less active star forming activity. This may indicate an evolutionary progression towards star formation, where active star forming environments are located at the middle, while less active regions are located at the top and bottom of this diagram. The lack of star formation activity in these latter regions might be associated to them being in a young evolutionary but also be caused by external factors such as magnetic fields, negatively impacting their star formation efficiency (Reyes-Reyes et al., 2024).

In this thesis I cover my work during my PhD program, focused on the characterization of high mass star forming regions, in which I specifically study the G353 protocluster, as well as the L1482 and

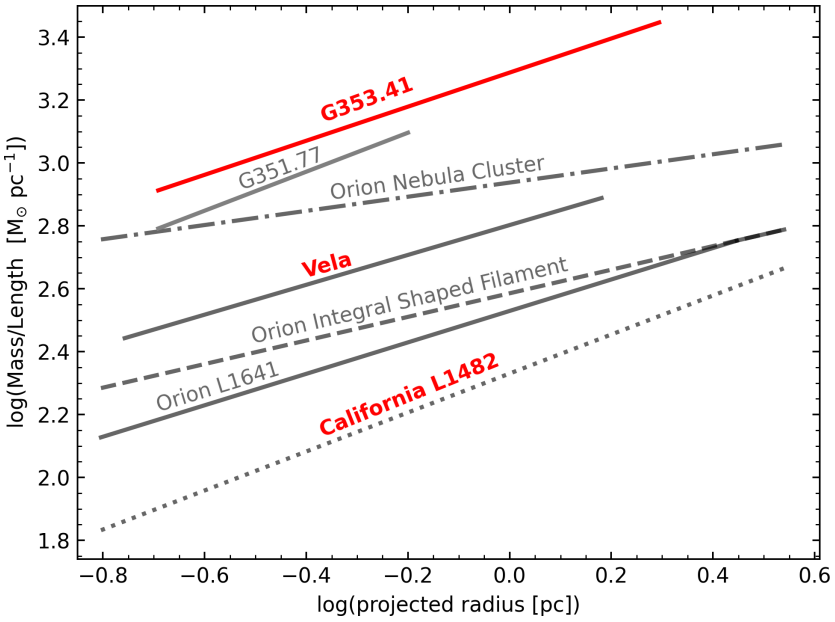

Figure 1.3: M/L profiles of multiple Galactic star forming filaments. In red we highlight the three main regions studied in this thesis. We include the M/L profile of G351 presented in Reyes-Reyes et al. (2024). Figure adapted from Álvarez-Gutiérrez et al. (2021).

Vela filaments. We observe dense and diffuse gas tracers such as N_2H^+ and $C^{18}O$ to map the velocity field in these environments using facilities such as ALMA, APEX, and the IRAM 30m. The high spatial and spectral resolution provided by these instruments, in combination with recent kinematics analysis techniques give us the opportunity of characterizing the velocity field at small and large scales.

We start by imaging the 15 ALMA-IMF Large Program (LP) (Motte et al., 2022). This large program contains a multitude of spectral lines which were observed using the Total Power antennas and the 7m and 12m arrays. Specifically we imaged the N_2H^+ line emission and we also extracted the N_2H^+ hyperfine isolated component. These data will be published in a future paper (Stutz et al. in prep.). The imaging and extraction procedure is described in Chapter 2. After the imaging we focus on the kinematical characterization of the G353 protocluster, a massive ($2.5 \times 10^3\,M_\odot$) star forming region embedded in a large scale filament. By creating an intensity-weighted position-velocity (PV) diagram we are able to identify and characterize nine V-shaped converging velocity gradients. We suggest that these are the product of inflow motions in the gas, mostly along filaments, towards denser regions inside the protocluster. At large scales we model the protocluster as an sphere under gravitational infall and we find that the velocities match the traditional PV diagram. We describe our analysis in detail in Chapter 3 and subsections therein.

Complementary projects include on-going kinematic analysis of the L1482 (Álvarez-Gutiérrez et al., 2021) and the Vela filaments, as well as the characterization of the mass distribution of Vela and the parent filament of the G353 protocluster. These projects are presented in Chapter 4. The L1482 filament is located in the California molecular cloud (CMC) at $\sim 500\,pc$. This cloud is as massive as Orion ($10^5\,M_\odot$) but present an order of magnitude less YSOs. This difference in star formation

activity can be explained by the cloud being less dense than Orion (Álvarez-Gutiérrez et al., 2021). Specifically we mapped the south extent of L1482 using the IRAM 30m radiotelescope tracing $C^{18}O$, HCO^+, and N_2H^+. We found a large discontinuity in the filament at the location of a star cluster. We identify multiple V-shaped VG that might suggest gravitational collapse at small scale as suggested in (Álvarez-Gutiérrez et al., 2024). We look at the YSO astrometry in the region using Gaia and APOGEE data. We find that most of the YSO follow the gas velocities traced by $C^{18}O$ and some sources are clumped at the location of the star cluster, where there is a filamentary discontinuity in the gas. We also used APEX 12m radiotelescope to observe the central and south part of Vela in $C^{18}O$, ^{13}CO, and ^{12}CO $(2-1)$. This structure has a mass of $\sim 8 \times 10^4\,M_\odot$ and is located at $\sim 1\,pc$ (Fissel et al., 2019). In $C^{18}O$, the filament located at the central region of Vela is well described by one velocity component and two components appear near the north and south. We identify two V-shaped VG. These are located along the filamentary structure. We also compare the filament hosting the G353 protocluster and Vela with other massive star forming regions by estimating their M/L profiles. We suggest that young or inefficient environment, such as being affected by magnetic fields, are located at the bottom (L1482) or top of our diagram (G353 parent filament), while more active regions are located in the middle (Vela, Orion). These analyses are presented in Chapter 4 and the summary of our findings in Chapter 5.

Chapter 2

Imaging of the ALMA-IMF N_2H^+ (1-0) targets

The ALMA-IMF Large Program[1] (LP) maps 15 dense, nearby (2 − 5.5 kpc), and massive ($2 - 32$) $\times$ 10^3 $M_\odot$ Milky Way protoclusters down to $\sim$2 kau scales (Motte et al., 2022), at a matched spatial resolution. ALMA-IMF provides a large protocluster sample in order to test the universality of the stellar initial mass function (IMF) (Bastian et al., 2010; Offner et al., 2014). The ALMA-IMF LP also provides a vast catalog of molecular lines, in bands 3 ($2.6 - 3.6$ mm) and 6 ($1.1 - 1.4$ mm). This rich molecular treasure trove allows for a detailed kinematical characterization of the gas, protostellar cores, and young stellar objects (YSOs) present in these protoclusters. The current publicly available ALMA-IMF data include, but are not limited to, continuum maps (Díaz-González et al., 2023; Ginsburg et al., 2022a), 12 m data cubes of all spectral windows (Cunningham et al., 2023), core catalogs (Louvet et al., 2023; Pouteau et al., 2023), and hot core and outflow catalogs (Armante et al., 2024; Bonfand et al., 2024; Cunningham et al., 2023; Nony et al., 2023; Towner et al., 2024, Valeille-Manet et al. in prep). The data products derived from the ALMA-IMF LP allow us to constrain the different star-forming environments, in which we can analyze column densities, temperatures, outflow masses, core properties, and multi-tracer gas kinematics. This approach offers a thorough characterization of the processes taking place in these regions.

Motte et al. (2022) present a method of classifying these 15 protoclusters based on their evolutionary stage, assuming that they exhibit more H II regions as they evolve. They take into account the flux ratio between the 1 mm to 3 mm continuum maps ($S^{cloud}_{1.3\ mm}/S^{cloud}_{3\ mm}$), and the free-free emission at the frequency of H41α ($\sum^{free-free}_{H41\alpha}$). They find that as protoclusters evolve, $S^{cloud}_{1.3\ mm}/S^{cloud}_{3\ mm}$ decreases, while $\sum^{free-free}_{H41\alpha}$ increases (Motte et al., 2022, see their Fig. 3). Using these constraints, they group their 15 protocluster as being in a young, intermediate, or evolved evolutionary state.

The N_2H^+ (1−0) transition (ν = 93.173809 GHz), given its high critical density, n_{crit} = 2×10^5 cm^{-3} (Ungerechts et al., 1997), allows us to access the dense gas kinematics present in the innermost parts of star-forming regions (Álvarez-Gutiérrez et al., 2021; Bergin et al., 2002; Caselli et al., 2002a;

[1]Proposal ID 2017.1.01355.L, PIs: Motte, Ginsburg, Louvet, Sanhueza

Chen et al., 2019; González Lobos & Stutz, 2019; Hacar et al., 2018; Lippok et al., 2013; Storm et al., 2014; Tafalla et al., 2004). The J = 1→0 transition presents seven hyperfine components (Caselli et al., 2002a, 1995; Cazzoli et al., 1985). The kinematic analysis of this complex emission can be simplified by considering only the well-separated isolated component (93.17631 GHz; $F_1, F = 0, 1 \rightarrow 1, 2$; Cazzoli et al., 1985). Such simplification is convenient to study the complex velocity fields found at the center of filaments. These regions present the densest environments for star formation, usually presenting multiple, blended velocity components, in which the velocity distributions exhibit twists, turns, spirals, and wave-like patterns (Álvarez-Gutiérrez et al., 2021; Csengeri et al., 2011; Fernández-López et al., 2014; González Lobos & Stutz, 2019; Henshaw et al., 2020; Liu et al., 2019; Olguin et al., 2023; Redaelli et al., 2022; Sanhueza et al., 2021; Stutz & Gould, 2016). Recent techniques, such as the intensity-weighted PV diagrams (Álvarez-Gutiérrez et al., 2021; González Lobos & Stutz, 2019), allow us to characterize processes such as infall, outflow, or rotation present in these environments, in which high spatial and spectral resolution studies open a window onto the small-scale gas kinematics of star-forming regions. In addition to the PV diagrams, we can create position-position-velocity (PPV) diagrams, in order to identify coherent structures that might be both spatially and kinematically associated (Chen et al., 2019; Henshaw et al., 2019, 2020; Redaelli et al., 2022; Sanhueza et al., 2021).

Here we focused on the imaging of these 15 regions traced by N_2H^+ (1−0). We obtain the combination of the N_2H^+ 7 m and 12 m (from now on called "7m+12m") measurement sets of all 15 fields using the publicly available ALMA-IMF reduction pipeline [2] described in Ginsburg et al. (2022b). For the imaging, we used the scripts provided by the ALMA-IMF repository. We aimed for an uniform set of cleaning parameters, avoiding imaging artifacts such as divergences. For all the fields, the choose that:

- The pixel scale is ∼2.5 times the minor axis of the beam,
- We set the cleaning threshold to 2 sigma,
- The scales are (0, 3, 6, 12),
- The gain is set to 0.06,
- The cyclefactor is set to 5,
- We set pblimit to the value of pbmask listed in Table 2.1.

After we obtained the final 7m+12m primary beam corrected data products, we subtract the continuum emission using the CASA task "imcontsub"[3]. Once we have the continuum subtracted 7m+12m data, we combine them with the Total Power data using the CASA task "feather"[4]. For the feathering of G327, W43-MM2, W43-MM3, and W51-IRS2 we use the 7m+12m JvM primary beam corrected data. We present the normalized moment zero map of each region in Fig. 2.1. Relevant information regarding the data products, such as beam sizes and RMS, are listed in Table 2.1.

[2] https://github.com/ALMA-IMF/reduction
[3] https://casa.nrao.edu/docs/taskref/imcontsub-task.html
[4] https://casa.nrao.edu/docs/taskref/feather-task.html

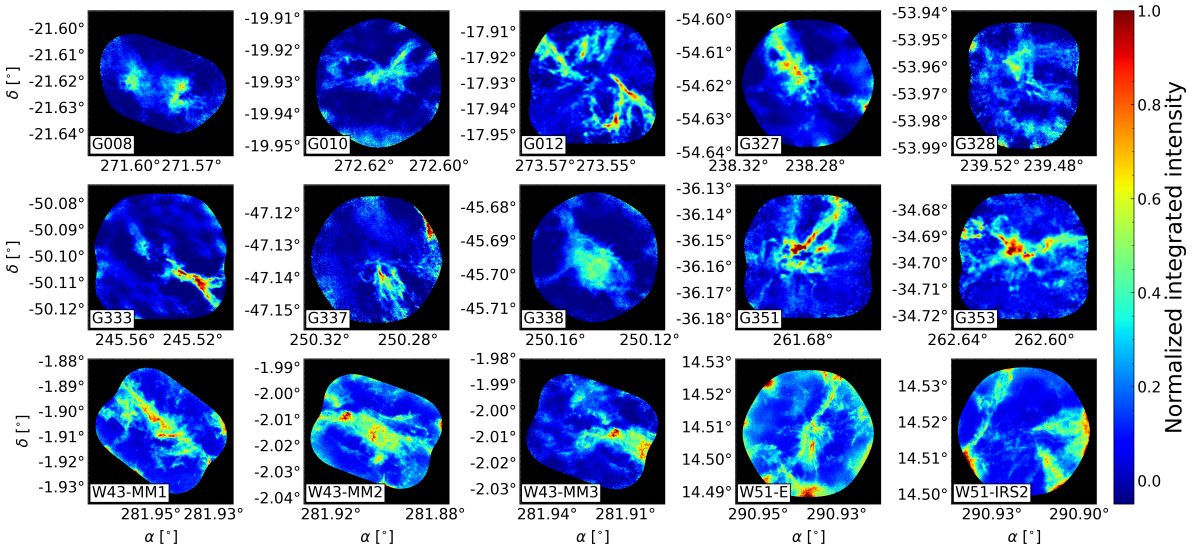

Figure 2.1: Moment zero maps of the 15 ALMA-IMF regions. We indicate the name of each region at the bottom left corner of each panel. Their integrated intensities are normalized by the value at 5σ from the mean integrated intensity of each region.

2.1 Isolated component extraction

We generalize the procedure presented in Álvarez-Gutiérrez et al. (2024) (see § 3.3) for all ALMA-IMF targets. This procedure depends on the signal-to-noise ratio (SNR) of the isolated component. We take the mean N_2H^+ spectrum of each region and estimate the velocity at the valley (V_{valley}) between the isolated and the main line components. Now, to determine the SNR of each spectra we take the peak intensity up until V_{valley} divided by the RMS determined in emission-free channels.

Below we list the SNR set for each region:

- SNR = 4 for G008, G010, G333, G337, G338, W43-MM2, W43-MM3, W51-E,
- SNR = 5 for G012, G328, G351, G353, W43-MM1,
- SNR = 7 for G327,
- SNR = 4, 6, and 8 for W51-IRS2.

For spectra with a SNR < SNR threshold, we make the extraction of the bluer velocities up until the location of the mean intensity valley. For spectra with SNR > SNR threshold, instead of using the mean dip as a velocity limit, we choose among different velocity guesses, in order to choose the one that captures the bluer velocities and the isolated component, while excluding the rest of the N_2H^+ emission. For W51-IRS2, the mean spectrum of the cube presents emission in a velocity range of $\sim 40\,km\,s^{-1}$, and we can't use a fixed value for V_{valley}. For this region we define $V_{valley} = V_{\text{main peak}} - 4\,km\,s^{-1}$, where $V_{\text{main peak}}$ is different for each spectrum in the cube.

Table 2.1: Relevant cube information

Field	Pixel scale ["]	BMIN ["]	BMAJ ["]	BPA [°]	RMS[a] [K]	RMS[b] [K]	RMS velocity range [km/s]	V_{LSR}[c] [km/s]	Pbmask
G008	0.34	0.85	1.11	76.61	1.03	2.10	13 – 21 , 51 – 62	37.6	0.20
G010	0.19	0.42	0.55	-77.45	2.08	4.07	-30 – -19 , 9 – 25	-2.0	0.18
G012	0.84	2.11	2.60	89.29	0.31	0.57	12 – 21 , 49 – 62	37	0.15
G327	0.27	0.65	0.80	59.14	0.42	0.77	-70 – -59 , -32 – -20	-45	0.23
G328	0.45	1.19	1.30	71.91	0.84	1.55	-68 – -60 , -29 – -18	-43	0.20
G333	0.56	1.15	1.24	70.55	0.51	0.97	-72 – -61 , -38 – -22	-47	0.10
G337	0.35	0.82	0.91	89.02	0.99	1.88	-65 – -51 , -26 – -15	-40	0.18
G338	0.23	0.60	0.64	-54.83	2.05	3.46	-87 – -78 , -44 – -37	-62	0.25
G351	0.76	2.07	2.32	-81.12	0.37	0.67	-28 – -18 , 9 – 22	-3.0	0.20
G353	0.72	1.96	2.29	80.19	0.37	0.68	-43 – -32 , 0 – 7	-18	0.18
W43-MM1	0.24	0.65	1.05	-84.30	0.56	0.97	72 – 81 , 112 – 122	97	0.22
W43-MM2	0.14	0.35	0.45	-72.87	0.70	1.22	66 – 75 , 106 – 114	90	0.25
W43-MM3	0.2	0.52	0.71	78.61	0.38	0.67	73 – 78 , 107 – 121	97	0.25
W51-E	0.14	0.36	0.40	-68.37	2.45	4.60	25 – 36 , 78 – 85	55	0.18
W51-IRS2	0.14	0.37	0.41	-70.26	1.19	1.85	16 – 35 , 80 – 93	55	0.30

Notes. [a] RMS value at the peak of the RMS distribution. [b] Mean RMS. [c] Obtained from https://raw.githubusercontent.com/ALMA-IMF/reduction/master/reduction/imaging_parameters.py.

Each velocity guess has an associated weight defined for most fields as:

$$w = (I_{normed} * 0.2 + dV_{normed} * 0.8)^{-1}, \quad (2.1)$$

Where the "normed" subscript indicates that the parameter array is divided by its minimum value, ensuring that the guess with the smallest "I" and "dV" will have a weight of 1.

For better results in specific regions, we define the weights as:

- $w = (I_{normed} * 0.5 + dV_{normed} * 0.5)^{-1}$ for G010,
- $w = (I_{normed} * 0.9 + dV_{normed} * 0.1)^{-1}$ for G327, W43-MM2, and W43-MM3,
- $w = (I_{normed} * 0.3 + dV_{normed} * 0.7)^{-1}$ for W51-IRS2.

The data products will be published in Stutz et al. (in prep), and for each field, these data contain:

- A data cube that only contains the isolated component, masked with a SNR cut above the thresholds mentioned above ('region-name'_isolated_component_cleaned_snr.fits).
- A data cube with the isolated component without SNR masking. As described above, for isolated components with SNR below the threshold, we extract the spectra until the mean dip ('region-name'_isolated_component.fits).
- An auxiliary data cube that contains the used mask, the selected I, dV, and weight, and the I, dV, and weight of the guesses.

Chapter 3

Dense gas kinematics of the G353 protocluster

3.1 Introduction

Out of the 15 ALMA-IMF regions imaged in chapter 2, we analyze the G353.41 protocluster (hereafter G353; see Fig. 3.1), and in particular, on the dense gas kinematics observationally accessible from the protocluster scale ($2.9\,\mathrm{pc}^2$) to the core scale. We trace this dense and cold gas using the N_2H^+ (1-0) line observed with ALMA. Given that N_2H^+ is detected at high column densities ($N(H_2) \gtrsim 10^{22}\,\mathrm{cm}^{-2}$; Tafalla et al., 2021), we gain access to the inner dense gas "skeleton" of the protocluster structure, free from confusion induced by lower-density gas. Meanwhile, ALMA permits us to obtain the resolution needed to trace structures down to the core scales at which individual or small numbers of stars may be forming.

In Fig. 3.1 we indicate the ALMA-IMF N_2H^+ (1−0) coverage of G353 (centered at α,δ (J2000) = (17:30:26.28,−34:41:49.7) and its parent filament (dark lane traced by ATLASGAL 870 μm emission; Schuller et al., 2009) with light green and gray contours, respectively. Motte et al. (2022) classify this protocluster as being in an intermediate evolutionary state, located at ∼2 kpc, and hosting a total mass of 2.5×10^3 $M_\odot$. They describe G353 as isolated, without obvious interaction with massive nearby stellar clusters. Using moment maps derived from the N_2H^+ (1−0) 12 m dataset, they suggest the presence of multiple velocity components, indicating a complex velocity field. They propose that G353 is composed of filaments interacting at the central hub. As is presented in Bonfand et al. (2024), this region is an outlier in the ALMA-IMF hot core sample. Only one weak, low-mass (< 2 $M_\odot$) compact methyl formate source is detected and it lacks strong emission from complex organic molecules. They state that this protocluster is in a chemically poor stage, in which further characterization of this region is required.

In this project we investigate the N_2H^+ dense gas kinematics of G353 from large (protocluster) to small (cores) scales. In § 3.2 we present the data. In § 3.3 we introduce our N_2H^+ isolated extraction procedure. In § 3.4 we model and decompose the multiple velocity components found in the N_2H^+

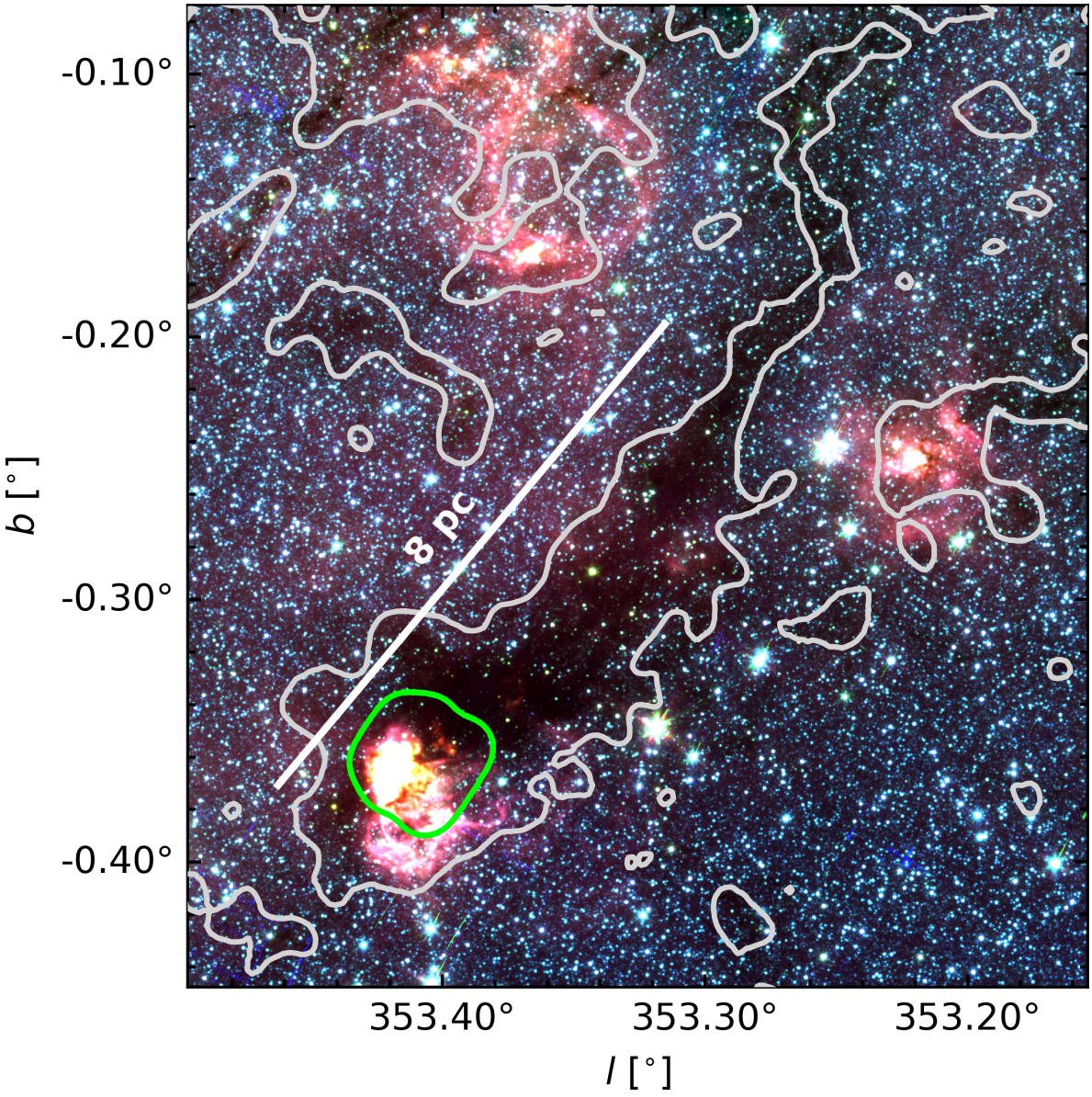

Figure 3.1: Composite image of G353: IRAC 3.6 μm (in blue), 4.5 μm (green), and 5.8 μm (red). We indicate the ALMA-IMF N_2H^+ (1−0) coverage with a light green contour. We highlight ATLASGAL emission (870 μm) at 40 mJy beam^{-1} with the gray contour, corresponding roughly to a *Herschel*-derived $N(H)$ of $\sim$ 5.5 $\times$ 10^{22} cm^{-2}.

isolated component spectra. In § 3.5 we show our gas kinematic analysis, from protocluster to core scales. In § 3.6 we show that G353 might be under gravitational collapse at small and large scales. In § 3.7 we estimate mass accretion rates for multiple velocity gradients (VGs) characterized in our N_2H^+ data. We discuss our results in § 3.8, and we present our summary and conclusions in § 5.

3.2 Data

3.2.1 ALMA-IMF data

As presented in § 2 we make use of the N_2H^+ (1−0) 12 m, 7 m, and Total Power observations described in Motte et al. (2022) for our analysis, providing robust uv plane coverage. We use 12 m datacubes from Cunningham et al. (2023) to compare the shock tracers SiO $(5-4)$ and CO $(2-1)$ to our N_2H^+ kinematic analysis. We use DCN and N_2H^+ data to determine core velocities (§ 3.4.2). To determine total masses in specific regions we use the $N(H_2)$ map from Díaz-González et al. (2023).

3.2.2 Core properties from published catalogs

We use the cores catalog[1] from Louvet et al. (2023). These cores were identified using the `getsf` algorithm, specialized in source extraction on regions with complex filamentary structures (Men'shchikov, 2021). This procedure was done using the 1.3 mm continuum maps, smoothed at a common resolution of ∼2700 au, obtaining a total of 45 sources for G353. We also use the DCN core velocities (15 sources, Cunningham et al., 2023) and the SiO outflow catalog (16 sources, Towner et al., 2024) in order to look for correlation between the N_2H^+ gas kinematics and cores/outflows position and properties. It is worth mentioning that, within a radius of 0.3 pc from the center of G353 (Motte et al., 2022), we find 60% of the 1.3 mm cores (27 sources), and ∼ 70% of the cores with DCN velocities and SiO outflows (11 sources from each catalog). Of these 11 outflows, 7 are "red" 3 are "blue" (monopolar), and 1 is "bipolar" (Towner et al., 2024). The presence of these sources might imply a complex velocity field in this region, given that cores and outflows disturb the kinematics of the surrounding gas.

[1] Available at `www.almaimf.com`

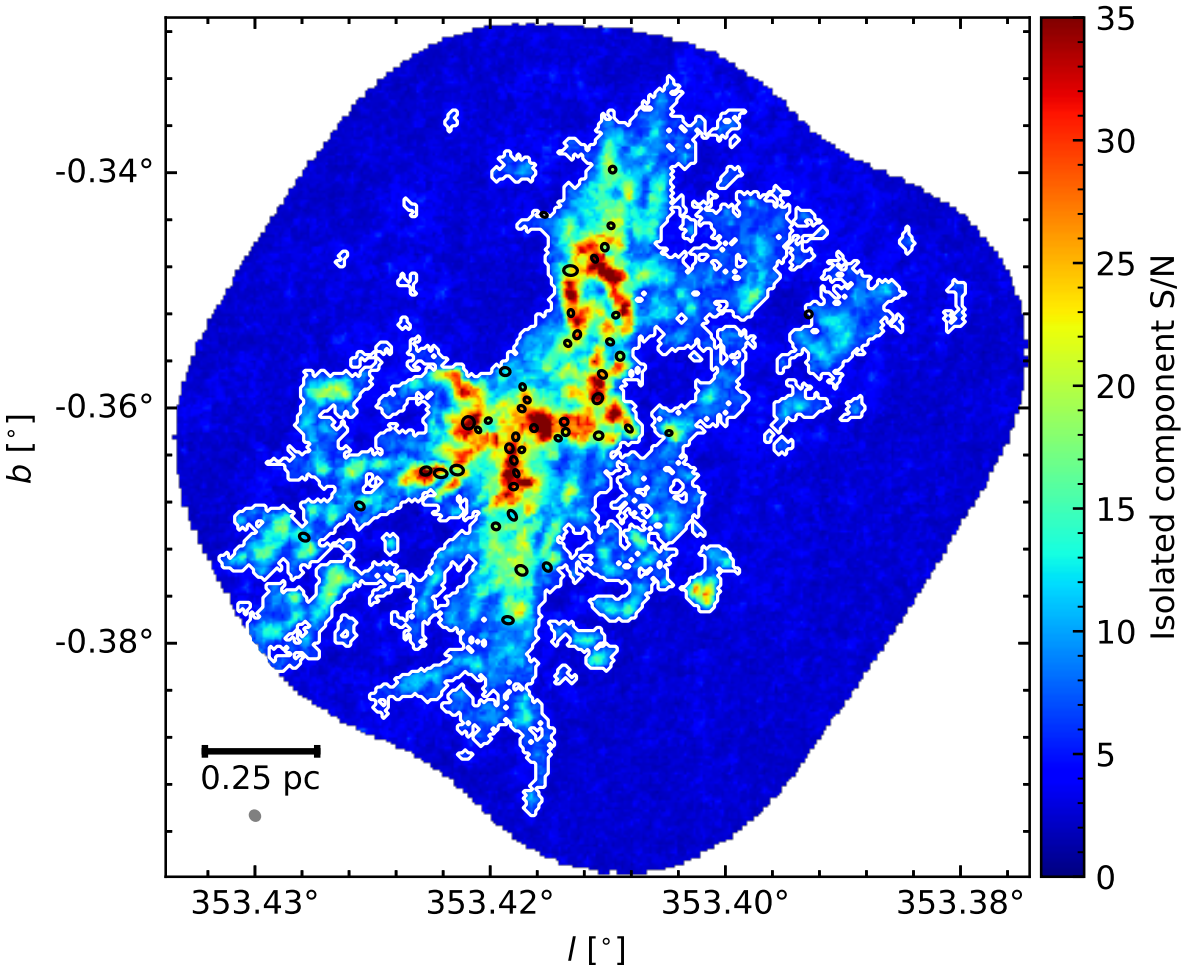

Figure 3.2: G353 N_2H^+ isolated component S/N map. The white contour indicates the location of data with an isolated component S/N $\geq$ 5. We show the location of the 1.3 mm cores presented in Louvet et al. (2023) with black ellipses and are located in regions with S/N $\geq$ 15. We indicate the beam size of these data with a gray ellipse at the bottom left corner. Outside the S/N contour we make a rough extraction of the isolated component (see text). For data inside the S/N contours, we implement a procedure based on detection of peaks and valleys, to individually extract high ($\geq$ 5) S/N isolated components (see § 3.3).

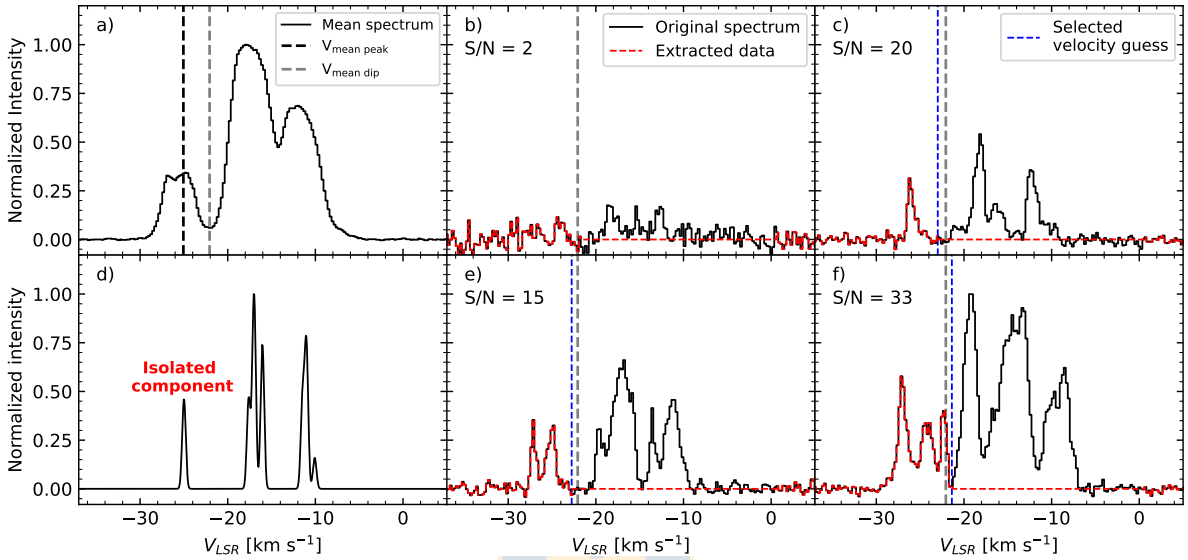

Figure 3.3: N_2H^+ spectra involved in our isolated component extraction procedure. **Panel a):** Normalized average N_2H^+ spectrum (solid black line) over the entire region. We show the location of the mean peak of the isolated component (dashed black line) and the "mean dip" (dashed gray line), see text. **Middle and right panels:** Normalized example spectra (within a pixel) of the N_2H^+ isolated velocity component extraction procedure (see § 3.3). We show G353 N_2H^+ spectra with solid black lines and the extracted isolated component, along with emission-free channels, with dashed red lines. **Panel d):** Expected N_2H^+ emission for an excitation temperature of 15 K, an opacity of 1, velocity centroid of $-17\,\mathrm{km\,s^{-1}}$, and a line width of $0.2\,\mathrm{km\,s^{-1}}$. We see the seven hyperfine components characteristic of this tracer, in which the most blueshifted corresponds to the isolated component. To derive this emission we use "n2hp_vtau" model from `PySpecKit`. In panels b), c), e), and f) we indicate $V_{mean\ dip}$ with a dashed gray line. We present data with S/N < 5 in panel b), in which we make a rough extraction based on the $V_{mean\ dip}$. We show data with S/N ≥ 5 in panels c), e), and f), presenting clear single, double, and triple N_2H^+ isolated velocity components, respectively. In these examples we represent the selected velocity guess that separates the isolated component emission from the main line emission with dashed blue lines. The offset positions (Δl, Δb) of the spectra in panels b), c), e), and f) are (0.68 pc, 0.27 pc), (0.12 pc, -0.28 pc), (-0.08 pc, 0.47 pc), and (0.16 pc, -0.07 pc), respectively. These offsets are estimated relative to the center of the region (see § 3.1).

3.3 N_2H^+ isolated component analysis and filament extraction

The N_2H^+ (1−0) transition is characterized by its hyperfine emission composed by seven components (Caselli et al., 1995, see their Fig. 1). We present an ideal example of N_2H^+ emission in Fig. 3.3, panel d. In this work we refer to the triplet of hyperfine components that present the highest intensities as the main N_2H^+ components, located at the center of the line emission at ν_{rest} = 93.173806 GHz. We refer to the most blueshifted hyperfine component as the isolated component, at ν_{rest} = 93.17631 GHz, shifted by $\sim -8\,\mathrm{km\,s^{-1}}$ relative to the main N_2H^+ component (see Table 1 from Cazzoli et al., 1985).

3.3.1 Isolated component identification and extraction

We developed an algorithm to extract only the isolated hyperfine component from every pixel in the feathered datacube. This is in order to reduce the complexity of our data, given that it may contain multiple velocity components in addition to the hyperfine line emission. Considering that the N_2H^+ emission moves in velocity across the protocluster, our approach is to find the velocity where the emission of the isolated component ends and remove the rest of the line emission. We also preserve the emission-free channels, at low ($-43\mathrm{km\,s^{-1}}$ to $-31.5\mathrm{km\,s^{-1}}$) and high ($0.7\mathrm{km\,s^{-1}}$ to $6.7\mathrm{km\,s^{-1}}$) velocities, to improve future RMS estimations if needed. It should be noted that in the procedures described below, we use `find_peaks`[2] to detect peaks and valleys in the different spectra.

Our extraction approach is separated into two procedures, for low and for high signal-to-noise ratio (S/N) data (see Fig. 3.2, and text below). In order to determine which data have low or high S/N, we obtained the mean spectrum over all the spatial pixels of the cube, which serves as a guide to determine the velocity at the "mean dip" ($V_{mean\ dip}$ = -22 $\mathrm{km\,s^{-1}}$, dashed gray line in Fig. 3.3 panel "a"). This velocity represents the mean location of the intensity valley between the isolated and the main components of the N_2H^+ emission. We defined $\Delta V_{mean} = 3.2\,\mathrm{km\,s^{-1}}$ as the difference between $V_{mean\ dip}$ and the velocity at the peak of the mean isolated component $V_{mean\ peak}$ (dashed black line in Fig. 3.3 panel "a"), used in our velocity guesses for the high S/N extraction procedure (see below).

To create a S/N map of the isolated component, we first measured the RMS noise in emission-free channels ($-43\,\mathrm{km\,s^{-1}}$ to $-31.5\,\mathrm{km\,s^{-1}}$), and the peak intensity in the channels range in which the mean isolated component is located ($-43\,\mathrm{km\,s^{-1}}$ to $V_{mean\ dip}$). This approach allows us to exclude the emission of the main line components. We encountered spurious emission at the edges of the S/N map. We adopted the procedure from Towner et al. (2024) by using the image processing techniques implemented by `binary_erosion`[3] (1 iteration) and `binary_propagation`[4] to clean the data for further analysis. `binary_erosion` allows us to remove the spurious emission in the outskirt of the map, although this approach also removes high S/N edges of our protocluster. Then, we used `binary_propagation` on the cleaned S/N map, using the original S/N map mask, to restore only the protocluster edges. To test our cleaning approach we computed the total integrated intensity using the Python package `SpectralCube`[5] in the range of $-31.5\,\mathrm{km\,s^{-1}}$ to $V_{mean\ dip}$ using the original and

[2] https://docs.scipy.org/doc/scipy/reference/generated/scipy.signal.find_peaks.html
[3] https://docs.scipy.org/doc/scipy/reference/generated/scipy.ndimage.binary_erosion.html
[4] https://docs.scipy.org/doc/scipy/reference/generated/scipy.ndimage.binary_propagation.html
[5] https://github.com/radio-astro-tools/spectral-cube

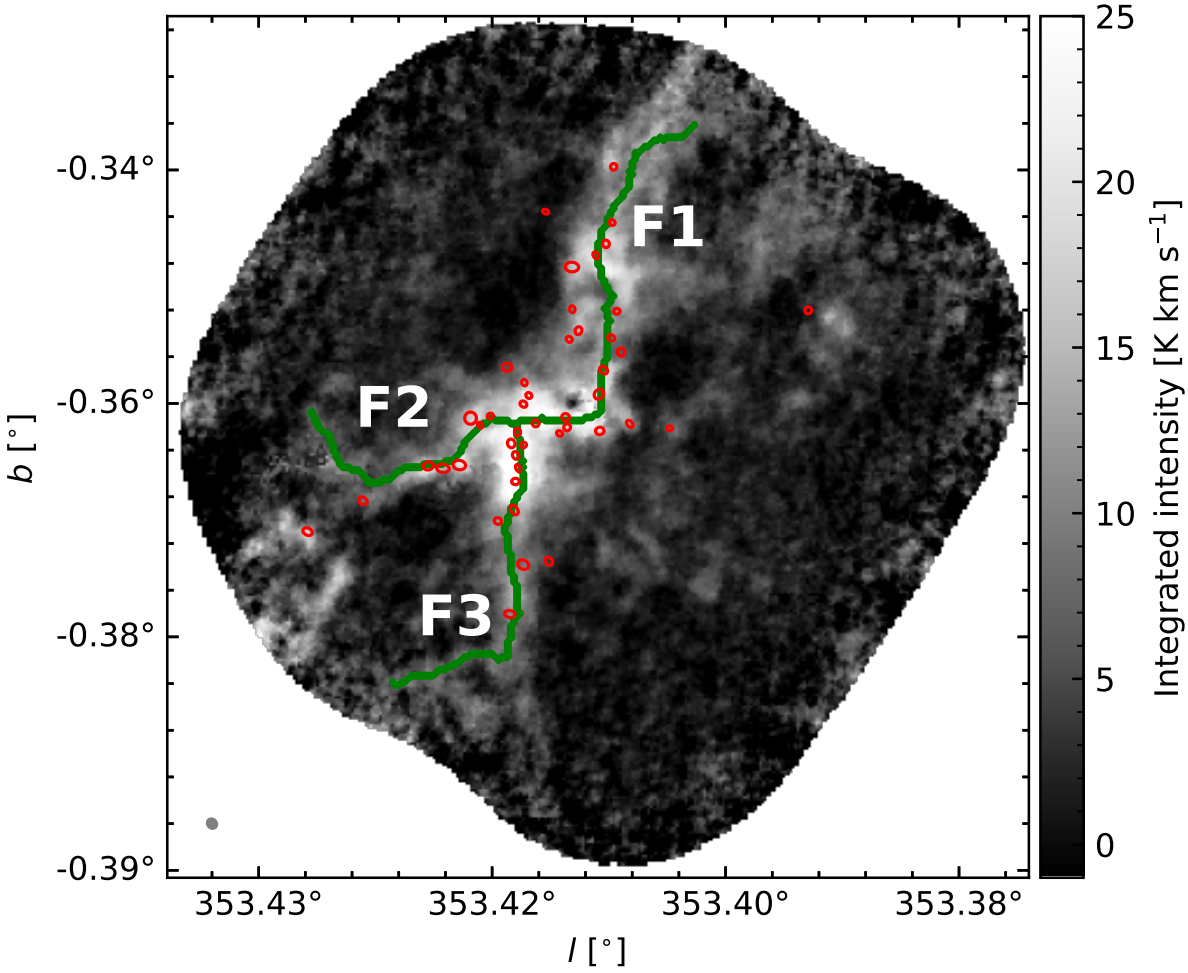

Figure 3.4: Moment 0 map of the extracted N_2H^+ isolated component emission. We use the `FilFinder` Python package to identify the main filamentary structure present in G353 (see Appendix A). We identify three filaments (F1, F2, and F3; green lines) converging toward the central hub. The location of most of the 1.3 mm cores (red ellipses), projected in the POS, lie on top of the spine of these filaments, specially in the hub.

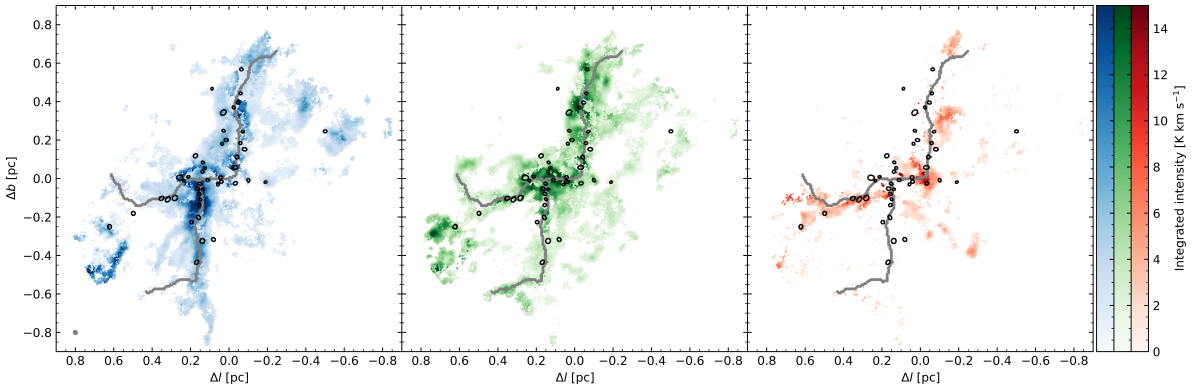

Figure 3.5: Spatial distribution of the modeled N_2H^+ isolated velocity components. We indicate the main filament structure with green lines (see Fig. 3.4). In blue, green, and red we indicate the first, second, and third velocity components, respectively. We indicate the beam size of these data with a gray ellipse at the bottom left corner. The emission of the first and second components is more extended and intense than the third, most red-shifted velocity component. The 1.3 mm cores match regions with high integrated intensity, mostly traced by the first and second velocity components.

cleaned S/N mask. We estimated that the removed spurious emission accounts for ∼2% of the total integrated intensity for data with S/N> 5.

In Fig. 3.2 we show the N_2H^+ isolated component S/N map, where at S/N values ≥ 5 we capture the cloud emission while excluding noise (white contour). We set our isolated component S/N threshold to 5, in order to use one of the two extraction procedures (see below). In this section we refer to high (low) S/N spectrum if its isolated component S/N $\geq$ 5 ($<$ 5). For low S/N spectra, we extracted all the channels in the velocity range from $-$ 43km s^{-1} up until $V_{mean\ dip}$ (panel "b" in Fig. 3.3). We take this approach given that for low S/N data we cannot identify peaks in the N_2H^+ emission in a reliable manner. For high S/N spectra the extraction procedure consists of creating different velocity guesses that represent the location of the intensity valley, similar to the definition of $V_{mean\ dip}$ (Fig. 3.3). Then, we selected a velocity guess based on its associated weight (see description below). This approach is described in detail here:

- First, we implemented a rolling average along each spectrum. This is in order to smooth over intensity bumps that might result in false positives for the detection of peaks and valleys. For this procedure, we averaged considering two channels before and after each velocity.

- After smoothing, for each spectrum we identified the isolated component peak using `find_peaks`. We called the velocity associated with this peak $V_{isolated\ component}$. In the case of multiple velocity components it represents the most blueshifted one. We found the intensity valley between the isolated component and the N_2H^+ main line emission by inverting the spectrum and finding the first peak which is the inverted intensity valley. We defined the associated velocity to this intensity valley as $V_{first\ minima}$.

- We created three velocity guesses based on the properties of each spectrum in our cube (see points below). These are the 1^{st} guess: $V_{isolated\ component} + \Delta V_{mean}$. 2^{nd} guess: $V_{first\ minima}$, In the

case of multiple isolated components this guess might incorrectly capture the intensity valley after the first isolated component. In that case, the other guesses are needed for a reliable isolated component extraction. 3^{rd} guess: $\mathrm{V}_{mean\ dip} + \Delta\mathrm{V}_{mean}$ to provide a velocity cut further away from the $\mathrm{V}_{mean\ dip}$. This guess is mainly useful in the case where multiple isolated components cover a velocity range larger than the one probed by the other two guesses.

- From each velocity guess we estimated two parameters to later decide which one to use. One is the absolute value of its associated intensity "I_i" (i.e., intensity at the guess velocity), and the other is distance in velocity "dV_i" to the mean dip. The i subscript represents the guess associated with these parameters. We save the parameters of each guess in the lists "I" and "dV".

- We normalized these lists by their minimum value ensuring that the guess with the smallest "I_i" and "dV_i" will have a weight (w) of 1, defined in Eq 3.1. We do not encounter divergences in this normalization given these parameters are not exactly zero.

$$w = (I_{norm} \times 0.2 + dV_{norm} \times 0.8)^{-1}, \tag{3.1}$$

  in which the "norm" subscript indicates that the parameter list is normalized by dividing it by its minimum value.

- By visual inspection we considered that we obtain good extraction results when the weight is mostly dependent on dV and in a minor part on I. This is reflected by the 0.2 and 0.8 factors multiplying I_{norm} and dV_{norm}, respectively, in the definition of "w" in Eq 3.1.

- We chose the guess with the weight closest to unity.

- Similarly as for $\mathrm{S/N} < 5$, we extracted the spectra from $-\ 43\mathrm{km\,s^{-1}}$ up until the velocity of the chosen guess, and preserved the emission-free channels from $0.7\mathrm{km\,s^{-1}}$ to $6.7\mathrm{km\,s^{-1}}$.

Various examples of N_2H^+ spectra and isolated hyperfine component extraction are shown in Fig. 3.3, in which we can see spectra containing one (panel "c"), two (panel "e"), and three (panel "f") velocity components, all well extracted by our procedure. In Stutz et al. (in prep) this approach is generalized to all ALMA-IMF regions for N_2H^+, providing reliable results.

3.3.2 Filamentary identification

We use the `FilFinder` Python package (Koch & Rosolowsky, 2015) in order to detect the most prominent filaments in this region (green lines in Fig. 3.4). The procedure, including the parameters we used for the filamentary identification, is presented in Appendix A. In Fig. 3.4 we indicate the detected filaments with green lines, on top of the moment zero map of the multiple N_2H^+ isolated components. We see that G353 is a hub-filament system (HFS), composed by three main filaments converging at its center. The HFSs are a characteristic feature of early stages of star formation, in which gas flows through the filaments toward the central hub triggering star formation (Busquet et al., 2013; Galván-Madrid et al., 2010, 2013; Kumar et al., 2022; Myers, 2009; Peretto et al., 2014; Zhou et al., 2022).

We see that in the plane of the sky (POS) most of the 1.3 mm cores (red ellipses) are located on top of the filaments. This spatial agreement between filaments and protostelar cores is consistent with filamentary fragmentation (André et al., 2010; Busquet et al., 2013; Kuznetsova et al., 2015, 2018; Stutz & Kainulainen, 2015).

3.4 N_2H^+ isolated component velocity decomposition

In Fig. 3.3 we see that clear multiple isolated velocity components are present in our dataset. In this section we present our approach regarding the line modeling of these multiple velocity components. We also show how we use these models to determine core velocities.

3.4.1 Modeling of the isolated component emission

To characterize the complex dense-gas kinematics traced by N_2H^+ we followed the method in Álvarez-Gutiérrez et al. (2021), and we used the spectroscopic toolkit `PySpecKit` (Ginsburg & Mirocha, 2011; Ginsburg et al., 2022a) to model and decompose the isolated component emission. `PySpecKit` adjusts a fixed number of components set by the user, based on visual inspection of the data we imposed three velocity components to every spectrum and then remove false positives (see below). Given the kinematic complexity of the data and cursory inspection of the spectra, a simpler analysis with only two components contradicts the data. In essence, three components is the simplest possible choice, given the data. While this might fail for a small number of spectra that could require ≥ 4 velocity components, the residuals indicate that this could occur in a severe minority of cases, and hence more components is not warranted given the S/N and resolution of this particular dataset. To improve the convergence of `PySpecKit`, we created a set of ranges for the parameters that define each of the three Gaussian velocity components, namely the peak intensity, central velocity, and velocity dispersion. After testing different parameter ranges, we set the intensity range between 1.76 K (four times the mean RMS) and 30 K, the velocity centroid from $-30\,\mathrm{km\,s^{-1}}$ to $-20\,\mathrm{km\,s^{-1}}$, and the velocity dispersion from $0.22\,\mathrm{km\,s^{-1}}$ to $1\,\mathrm{km\,s^{-1}}$.

From the results using the ranges defined above, we notice that some modeled components do not fit any emission. These fits are the result of imposing to the fitter a fixed number of components, given these spectra can be better represented by one or two velocity components. In these fits there is no uncertainty estimation for both the peak intensity and velocity dispersion. Based on these two criteria we removed those velocity fits from the modeled cube. With this cleaning approach we are left with spectra characterized by one ($\sim 34\%$), two ($\sim 53\%$), and three ($\sim 13\%$) Gaussian velocity components. We present the Gaussian fits of the high S/N spectra from Fig. 3.3 in Appendix B.

In Fig. 3.5 we show the spatial distribution of the multiple Gaussian velocity components. In gray we indicate the main filamentary structure in the region (see § 3.3.2). The first and second velocity components, in blue and green, respectively, present most of the high intensity emission and they also spatially dominate over the third, most red-shifted component. Both the first and second components trace mostly the filaments F1 and F3 from Fig. 3.4, where most of the 1.3 mm cores are located. The position of these cores coincide with high integrated intensity regions in these isolated velocity components. The most redshifted component is compact and less intense compared to the first and second velocity components. This velocity distribution is located mostly along the filament F2 and the central hub (see Fig. 3.4). In Fig. 3.6 we present the number of Gaussian velocity components for each spectrum, where we highlight that:

- Most of the N_2H^+ data presents emission characterized by two velocity components.

- Most of the spectra described by three velocity components are located in the innermost parts of the region.
- Most of the cores (black ellipses; Louvet et al., 2023) are located in regions with spectra presenting two to three Gaussian velocity components, indicating kinematic complexity even at ∼4 kau (N_2H^+ spatial resolution).
- Single velocity component spectra are located preferentially in the outskirt of the protocluster.

In Fig. 3.7 we show the histogram of the fitted velocity centroid of each Gaussian velocity component. The peaks of these distributions are located at −27, −24.7, and −23.3 km s^{-1}, respectively, well-separated in velocity. From hereafter we refer to these distribution as blue, green, and red, respectively. Most of the velocity components appear to be associated with the blue and green distributions. For consistency with the different tracers used in further analysis, we shift the isolated component velocities by +8 km s^{-1}, to the reference frame of the main line components of N_2H^+ (Cazzoli et al., 1985).

3.4.2 DCN and N_2H^+ derived core velocities

In this section our goal is to increase the sample of core velocities from the already published DCN catalog, aiming to explore all the potential in these types of dataset. Given the relatively high n_{crit} of DCN (3−2) (∼ 10^7 cm^{-3}) compared to N_2H^+ (1−0) (2×10^5 cm^{-3}), DCN (3−2) is known to coincide well with continuum peaks associated with cores (Cunningham et al., 2016; Liu et al., 2015; Minh et al., 2018), while N_2H^+ is characterized by tracing the dense gas at the innermost parts of star-forming regions (Fernández-López et al., 2014; González Lobos & Stutz, 2019; Hacar et al., 2018).

In Cunningham et al. (2023) they use ALMA-IMF 12 m observations of DCN (3−2) to study cores kinematics. They apply line emission fits for the DCN spectra inside the 1.3 mm cores from Louvet et al. (2023). For this procedure they determine core velocities in all ALMA-IMF targets. They classify as DCN single and complex core velocities, spectra that can be fitted with one or multiple Gaussian velocity components, respectively. Due to a global conservative S/N threshold the DCN fitting process missed the velocity estimation of some cores. For G353 only 15 out of the 45 cores present DCN velocity fits.

We used the ALMA-IMF DCN 12 m data from Cunningham et al. (2023), which presents a velocity resolution of ∼ 0.34 km s^{-1}. For each DCN core velocity described by a single component (Cunningham et al., 2023) we compared the emission of the DCN and modeled N_2H^+ isolated spectra. We found an average velocity offset between the DCN peak and the closest N_2H^+ isolated component peak of ∼ 0.65 km s^{-1}, less than two DCN channel widths. We used this approach for the remaining 30 cores, in order to determine their DCN velocities.

Here we estimated the RMS of the DCN data in emission-free channels in the range of −42 km s^{-1} to −25 km s^{-1} and we obtain the S/N map by dividing the peak intensity by the RMS. For the procedure below we only used DCN spectra with S/N > 3. Next, we extracted the average DCN and modeled N_2H^+ isolated component spectrum of these 30 cores. We identified the N_2H^+ isolated

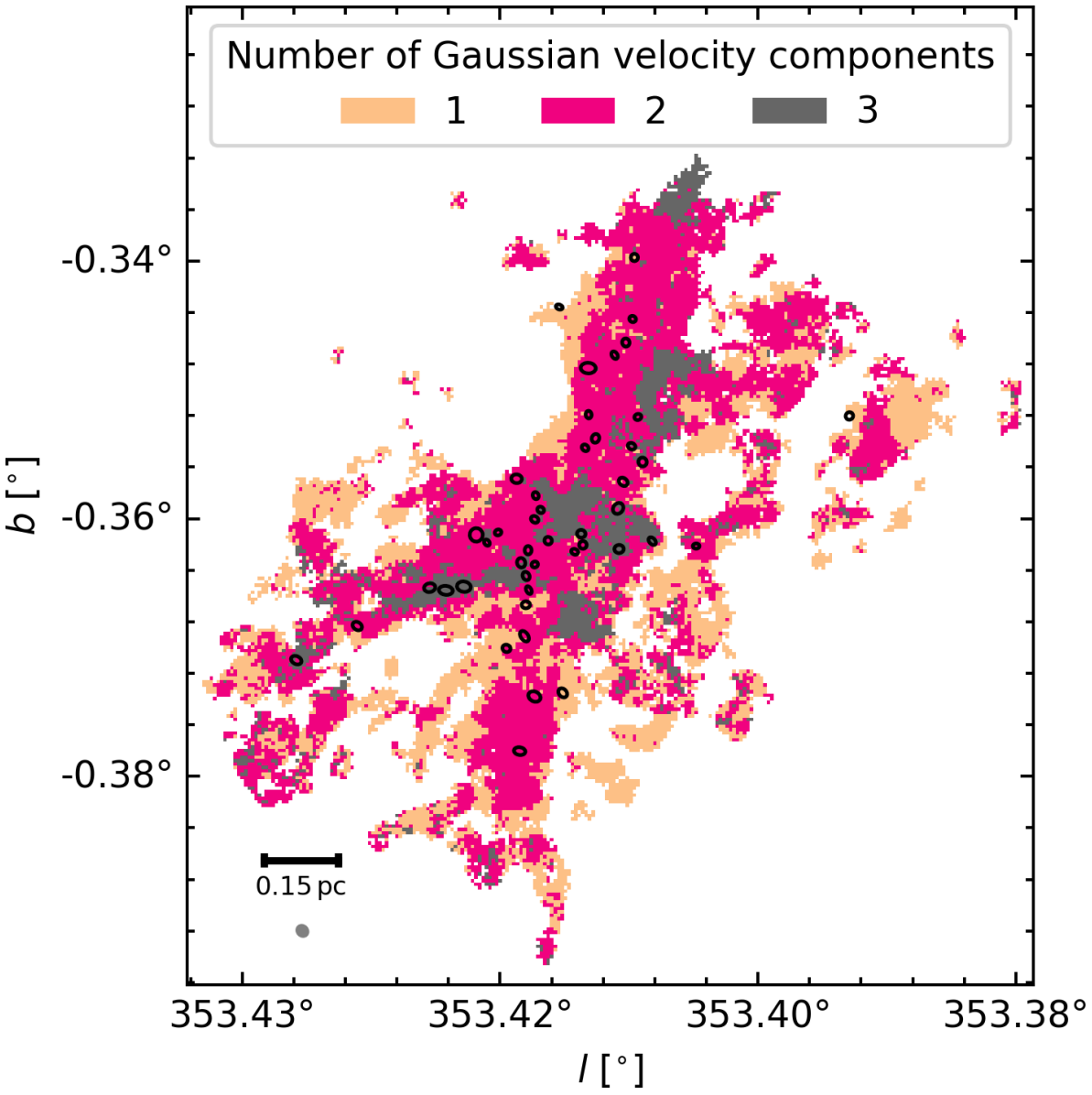

Figure 3.6: Spatial distribution of the modeled N_2H^+ isolated component spectra. These models are composed by up to three Gaussian velocity components. The 1.3 mm cores and beam size are the same as in Fig. 3.2. Most of the 1.3 mm cores are located in regions with spectra presenting two to three velocity components (see § 3.4.1).

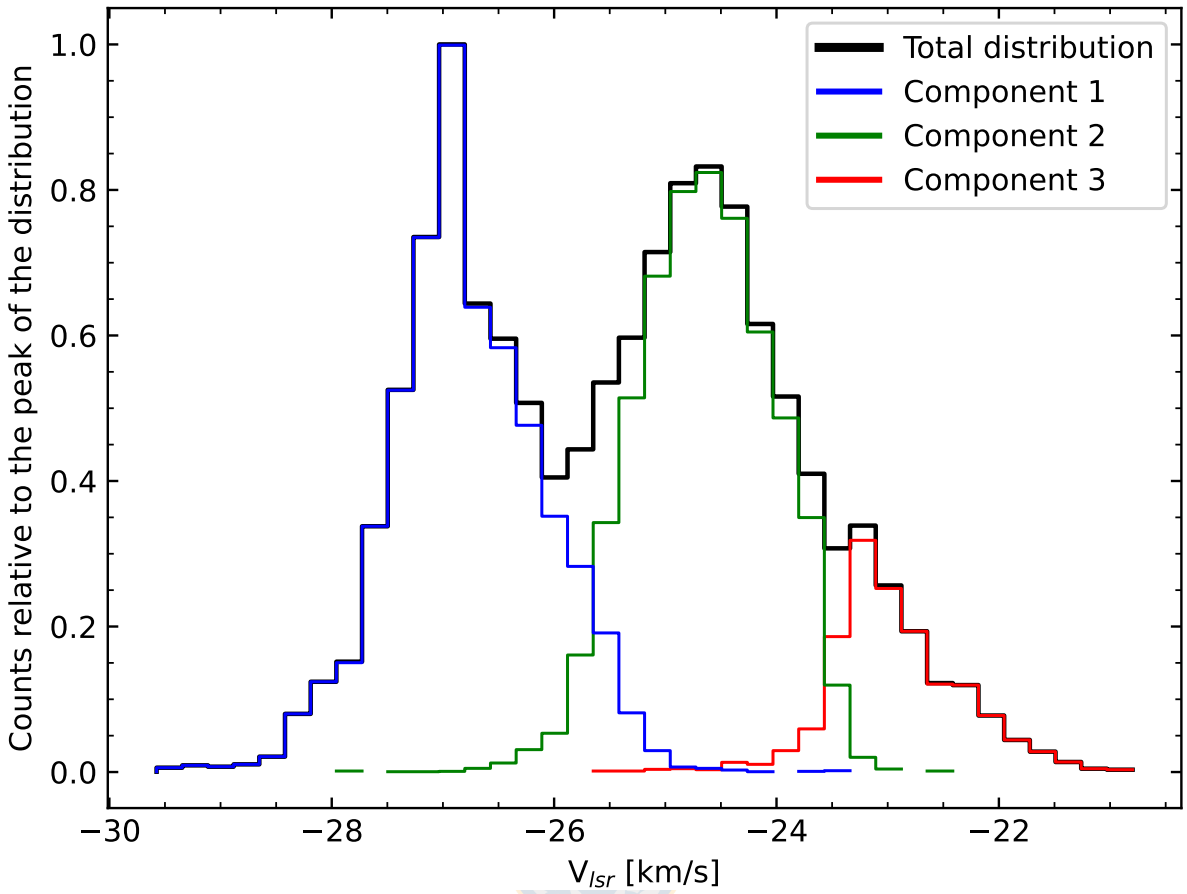

Figure 3.7: Normalized velocity centroid distributions of each N_2H^+ Gaussian velocity component. The velocities at the peak of the distributions are $-$ 26.9km s^{-1}, $-$ 24.7km s^{-1}, and $-$ 23.3km s^{-1} for component 1 (blue), 2 (green), and 3 (red), respectively (see § 3.4.1).

velocity component closest to the DCN peak within three DCN channel widths. We found that 11 out of these 30 cores present DCN with S/N $>$ 3 close to one N_2H^+ velocity component. Here, we defined the velocity of these cores as the velocity where the DCN emission peaks. On average, these cores have a velocity offset between these two tracers less than 0.8 km s^{-1} ($<$ 2.5 DCN channels), similar to the results obtained for the 15 cores with DCN velocities from Cunningham et al. (2023), and they present an average velocity offset of 0.38 km s^{-1}. Throughout this paper we refer to these cores as "DCN & N_2H^+ cores" given they are derived from the comparison of these two tracers. In Appendix C we present two examples of the comparison of the DCN and N_2H^+ spectra in cores in which we see clear agreement between these tracers (Fig. C.1). In Table C.1 we show these obtained core velocities from our comparison between DCN & N_2H^+ spectra, complementing the DCN catalog from Cunningham et al. (2023).

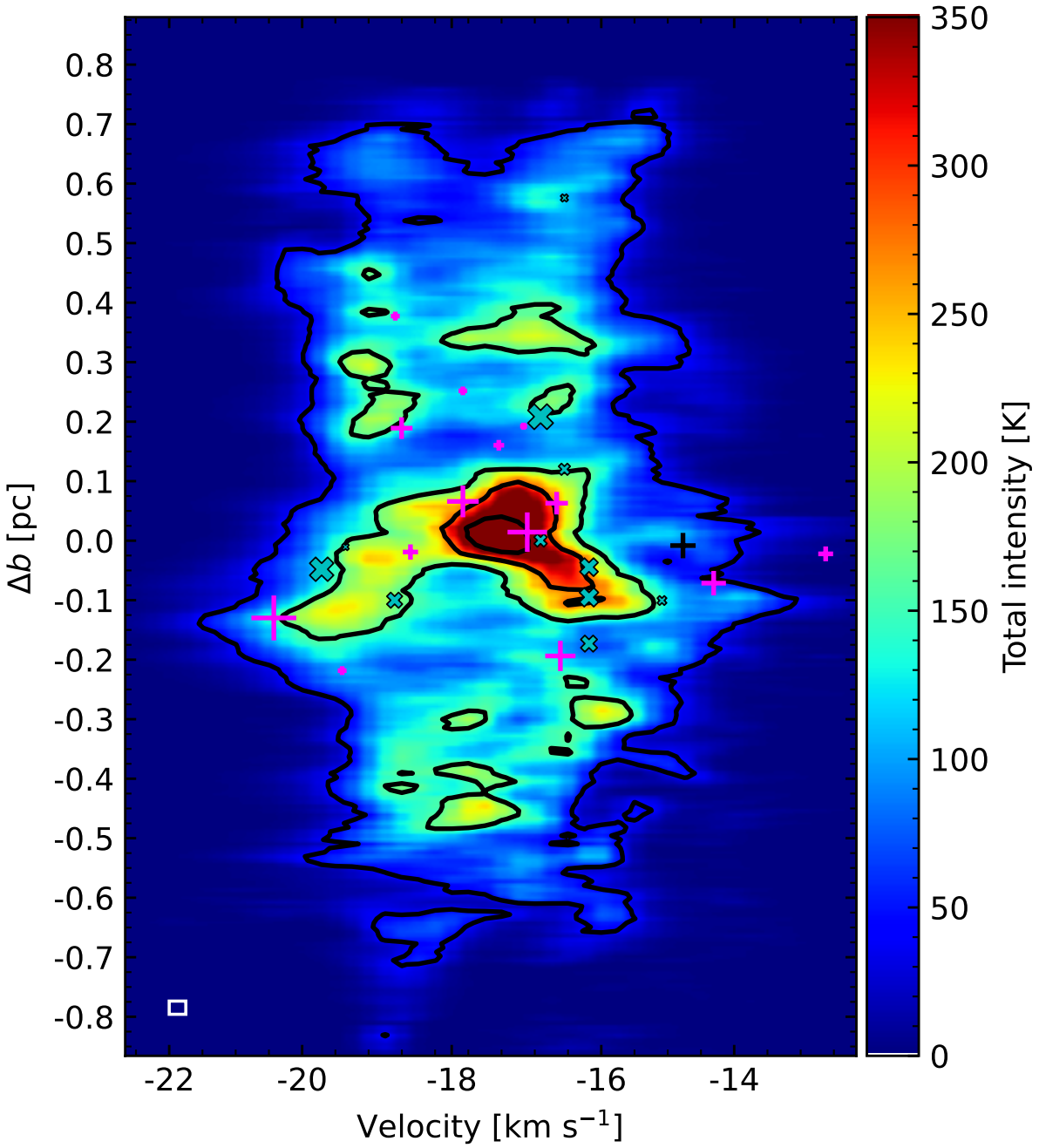

Figure 3.8: "Traditional" PV diagram of the N_2H^+ modeled isolated components, created by collapsing the l coordinate. Δb indicates the distance along b in pc, relative to the center of G353, assuming a distance of 2 kpc (Motte et al., 2022). The colormap indicates the total intensity along l. With fuchsia and black crosses we show the 1.3 mm cores with single and complex DCN velocities detections, respectively (Cunningham et al., 2023). With dark cyan "×" markers we show the 1.3 mm cores with velocities derived from DCN and N_2H^+ data (see § 3.4.2). The size of the markers indicate relative mass (Louvet et al., 2023). Black contours indicate total intensities at 40, 160, 280, and 400 K. We see a large-scale velocity spread ($\Delta V \sim 8\,km\,s^{-1}$) around $\Delta b \sim -0.3$ pc $-$ 0.13 pc (see also § 3.5.2). We show the major axis of the beam and the channel width with a white rectangle at the bottom left corner.

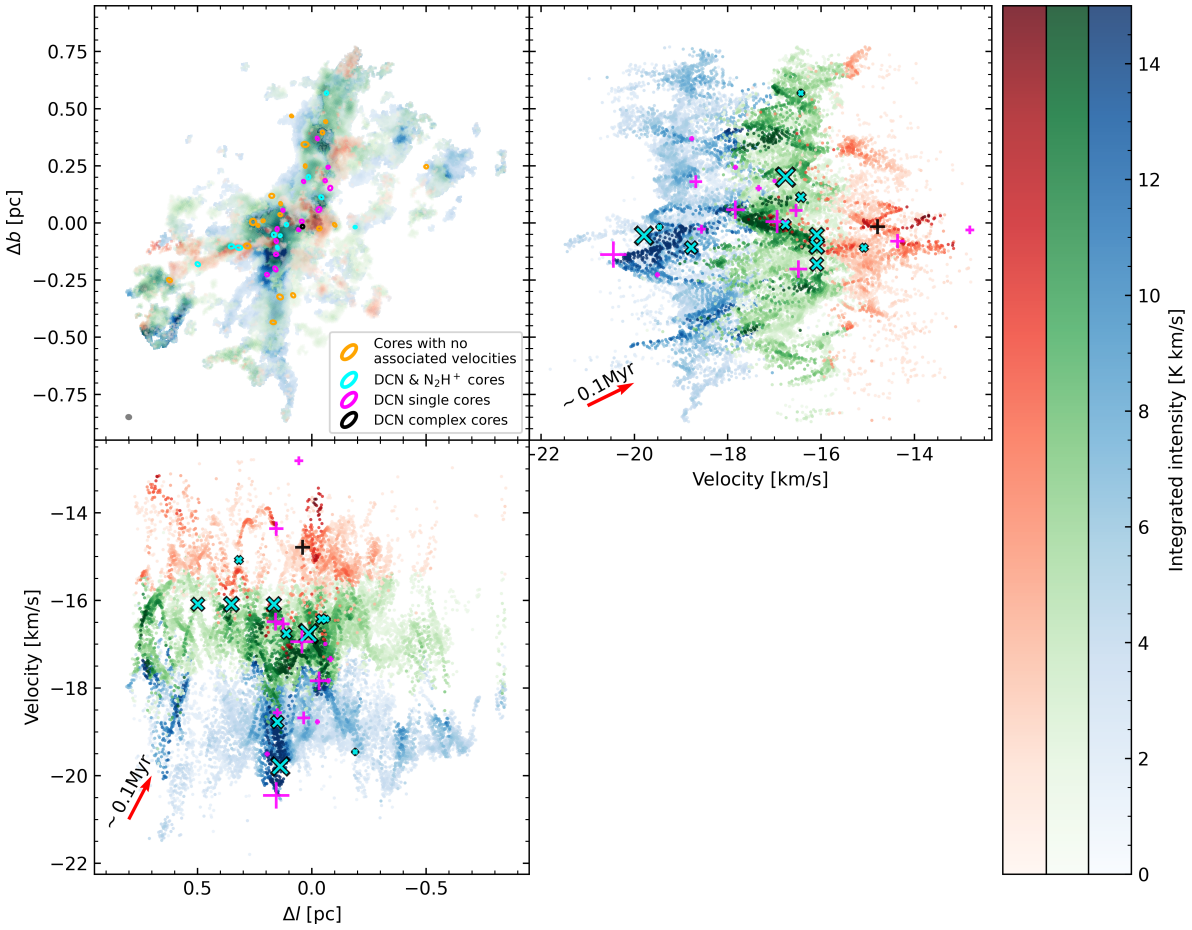

Figure 3.9: N_2H^+ intensity-weighted position-position and PV diagrams of G353. **Top Left:** Spatial distribution of the fitted N_2H^+ Gaussian isolated velocity components (blue, green, and red, see § 3.4.1). Ellipses indicate the location of the 1.3 mm continuum cores (Louvet et al., 2023). Orange indicates cores with no DCN detections. Fuchsia and black represent cores with single and complex DCN velocities (Cunningham et al., 2023). DCN & N_2H^+ cores are indicated with cyan. We show the beam size with a gray ellipse in the bottom left corner. **Top right and bottom left:** Intensity-weighted PV diagrams along the b and l coordinates, respectively. For the 1.3 mm core velocities we use the same colors and markers convention from Fig. 3.8. For reference we indicate with a red arrow, in both the top right and bottom left panels, a VG of 10 $\mathrm{km\,s^{-1}\,pc^{-1}}$ corresponding to a timescale of $\sim$ 0.1 Myr. We see multiple V-shapes near the location of cores across all velocities in the PV diagrams, more prominently in the top right panel (see Fig. D.1). The most prominent V-shape is located in the blue component, at $(\mathrm{V}, \Delta\mathrm{b}) \sim (-20.5\mathrm{km\,s^{-1}}, -0.14\,\mathrm{pc})$ (see § 3.5.2). We provide an interactive 3D PPV diagram at: `rodrigoalvarez.space/research/figures`.

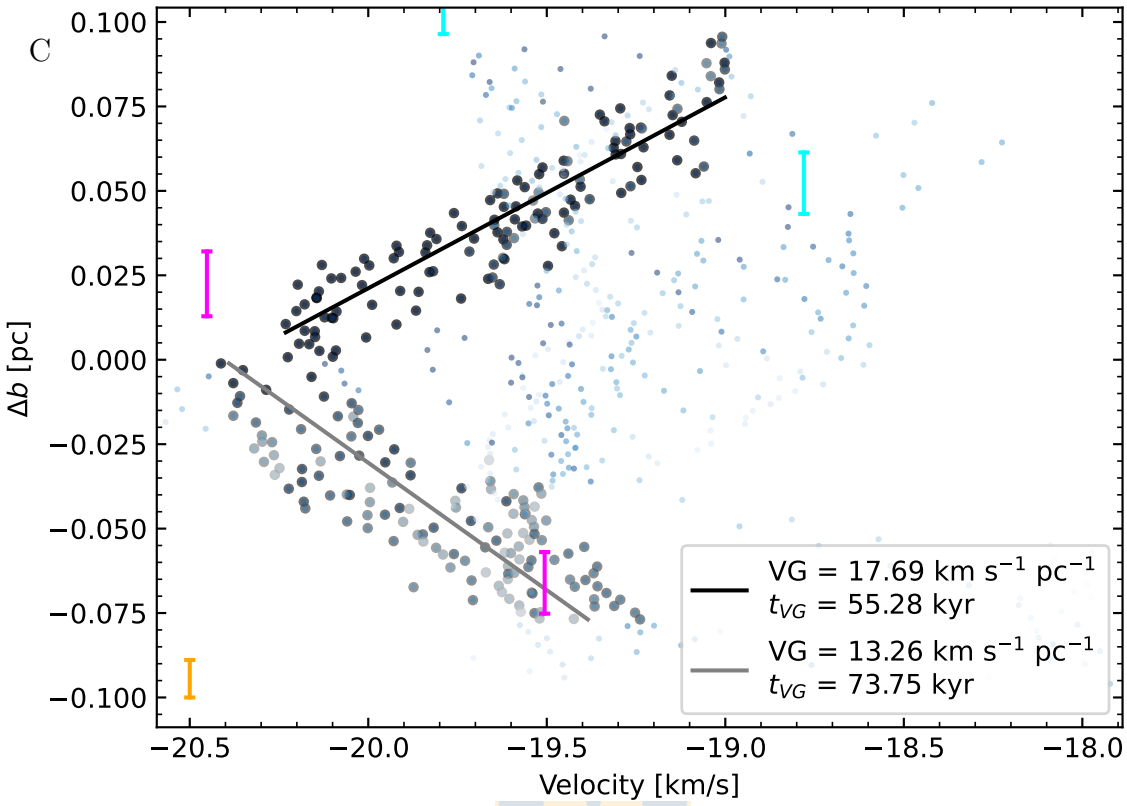

Figure 3.10: Zoomed-in version of the top right panel of Fig. 3.9, centered at the prominent blue V-shape ("C") located at $(\Delta b, \mathrm{V}) = (-0.14\,\mathrm{pc}, \text{-}20.5\mathrm{km\,s^{-1}})$. We indicate the major axis of the cores with vertical lines in fuchsia (DCN single) and cyan (N_2H^+), similarly we represent the major axis of the beam with a vertical orange line. We apply linear fits to the upper and lower distributions, represented by darker points. These points are selected based on an integrated intensity threshold (see § 3.5.3). We weight each point by their integrated intensity and derive VGs from the slope of these linear fits. The range of the obtained VGs is $\sim\ 13 - 18\,\mathrm{km\,s^{-1}\,pc^{-1}}$. We defined the timescale associated with the VG as $t_{VG} = \mathrm{VG}^{-1}$, being in the range of $\sim 50 - 70\,\mathrm{kyr}$. We show eight more well characterized V-shapes in Appendix D.

3.5 Analysis of position-velocity diagrams

3.5.1 Traditional position-velocity diagram

We start by analyzing the "traditional" PV diagram shown in Fig. 3.8. We created this diagram by taking the total intensity along the Galactic longitude, in which Δb indicates the distance in parsec relative to the center of G353, assuming a distance to the protocluster of of 2 kpc (Motte et al., 2022). We see general agreement between the DCN core velocities and the N_2H^+ velocity distribution. This suggests that most of the cores are still kinematically coupled to the dense gas in which they formed. As is presented in § 3.4.2, the DCN and N_2H^+ velocities match within $0.8\,\mathrm{km\,s^{-1}}$ (< 2.5 DCN channels).

Regarding the dense gas velocity distribution, in Fig. 3.8 we see a velocity spread of $\sim\ 8\ \mathrm{km\,s^{-1}}$

in the subregion between $\Delta b \sim -0.3$ pc to 0.1 pc. Most of the intensity on this diagram is located at the upper part of this subregion, at $\Delta b \pm 0.1$ pc. This spread is also present in the PV diagram along Δb and Δl shown in the top right and bottom left panel of Fig. 3.9. We explore the possible origin of this structure in § 3.6.

3.5.2 Intensity-weighted PV diagrams

In the top left panel of Fig. 3.9 we show the spatial distribution of the fitted Gaussian velocity components (see § 3.4.1). The blue, green, and red color maps indicate the integrated intensity of the first, second, and third velocity components of the N_2H^+ spectra, respectively. We note that the spatial overlap between any of these components is presented in Fig. 3.6.

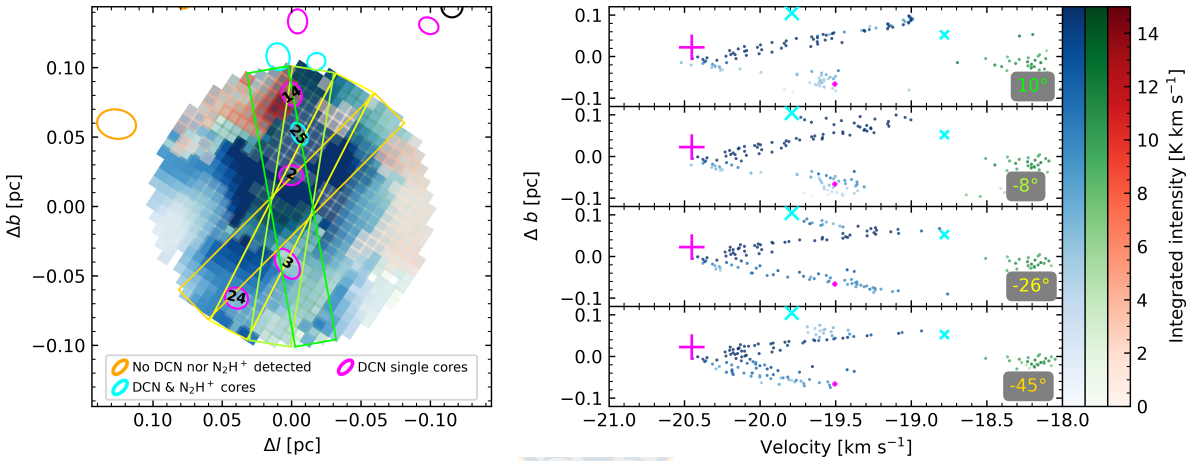

Figure 3.11: **Left panel:** Integrated intensity map of the modeled N_2H^+ isolated component within a region of radius of 0.1 pc, centered at V-shape "C". With boxes in shades of green and yellow, we indicate the different paths taken to create the PV diagrams shown on the right panel. The area covered by these four PVs matches the extent of this V-shape (see Fig. 3.12). The 1.3 mm cores are indicated using the same convention from Fig. 3.9. For the cores within the radius of 0.1 pc we indicate their IDs in black. **Right panel:** PV diagrams associated with the colored rectangles in the left panel. At the bottom right corner of each sub panel, with colored values, we indicate the angle (counter-clockwise) of each PV path. The PV paths match the V-shape coverage (right panel of Fig. 3.12). We see the overall structure of this V-shape persists at different angles, indicating that these structures are not a result of projection in the POS.

As is seen in Fig. 3.8, the traditional PV diagram provides information on the dynamics on the large, protocluster-scale, environment. Meanwhile, the intensity-weighted PV diagram (Fig. 3.9), in which the color of each point indicates its integrated intensity, highlights the small core-scale kinematics. Similarly as in González Lobos & Stutz (2019) and Álvarez-Gutiérrez et al. (2021), from the isolated component line decomposition (§ 3.4.1), we derived the integrated intensity and velocity centroid for each Gaussian velocity component. Using these parameters we created intensity-weighted PV diagrams along the b and l coordinates. We present these N_2H^+ PV diagrams in the bottom left and top right panels of Fig. 3.9. The key features on the position-position (PP) and on the top right PV diagram, are:

- The agreement between the DCN core velocities and the overall N_2H^+ PV structures suggests that cores are still kinematically coupled to the dense gas in which they formed.
- We see at least nine clear and prominent V-shaped velocity gradients (see Appendix D), across all velocity components. The orientation of these V-shape, pointing to the left/right (top right panel) or up/down (bottom left panel), follow no clear preference.
- In some cases, the vertex of these V-shapes is close spatially and in velocity to the location of cores.
- In the plane of the sky (POS), all three velocity components overlap in most of the region.
- This technique recovers the large-scale velocity spread present in Fig. 3.8 and highlights small-scale structures.
- The most prominent V-shape is located at $(\Delta b, \mathrm{V}) = (-0.14\,\mathrm{pc}, -20.5\,\mathrm{km\,s^{-1}})$, between two 1.3 mm cores with DCN detections (see § 3.6).

For a better visualization of the 3D structure of these V-shapes we provide an interactive 3D PPV diagram at: `rodrigoalvarez.space/research/figures`.

3.5.3 Velocity gradients

In this section we focus on the most prominent blue V-shape (Fig. 3.9, top right panel). In Fig. 3.10 we show this velocity distribution, named V-shape "C", in detail. Given the visual linearity of the VGs composing the V-shape, we applied a linear fit to these distribution in order to characterize them. For these fits we considered data only above an integrated intensity threshold of 8 $\mathrm{K\,km\,s^{-1}}$ and 3 $\mathrm{K\,km\,s^{-1}}$, for the upper and lower gradient, respectively. We removed data not related with the VG, clustered in the ranges of $(\Delta b, \mathrm{V}) \sim (-0.025 - 0.04\,\mathrm{pc}\ ,\ -19.5 - -18.5\,\mathrm{km\,s^{-1}})$, which lie just outside the filament hosting this V-shape on the POS. Additionally, we weighted each point based on their integrated intensity to make our fits more robust. The slopes of the linear fits represent the VGs in $\mathrm{km\,s^{-1}\,pc^{-1}}$. These linear fits follow the VGs distribution and these are somewhat asymmetric, the upper gradient is slightly shallower than the bottom gradient. Given the unknown inclination angle (θ) of these structures relative to the POS, the observed VG is just a fraction of the original VG. These are related as $\mathrm{VG} = \mathrm{VG}_{original} \cdot \sin(\theta)$. These VGs present values between ~ 13 to ~ 18 $\mathrm{km\,s^{-1}\,pc^{-1}}$ (see Fig. 3.10). Additionally, we estimated the center of this V-shape as the velocity-weighted mean position of the points composing this structure. With this approach the position of the points closest to the V-shape apex present more weight, obtaining the center of this V-shape at $(l, b) = (353.4135$ -0.3657. This position is located between "core 2" and "core 3", both of them having DCN velocity fits (Cunningham et al., 2023). These cores present masses of 20.7 and 9.4 $\mathrm{M_\odot}$, respectively. We inspected the core catalog from Louvet et al. (2023) and concluded that the location of this V-shape do not coincide with any core.

In the left panel of Fig. 3.11 we show the integrated intensity of the multiple modeled N_2H^+ isolated components. With colored boxes we show the areas where we create the different PV diagrams

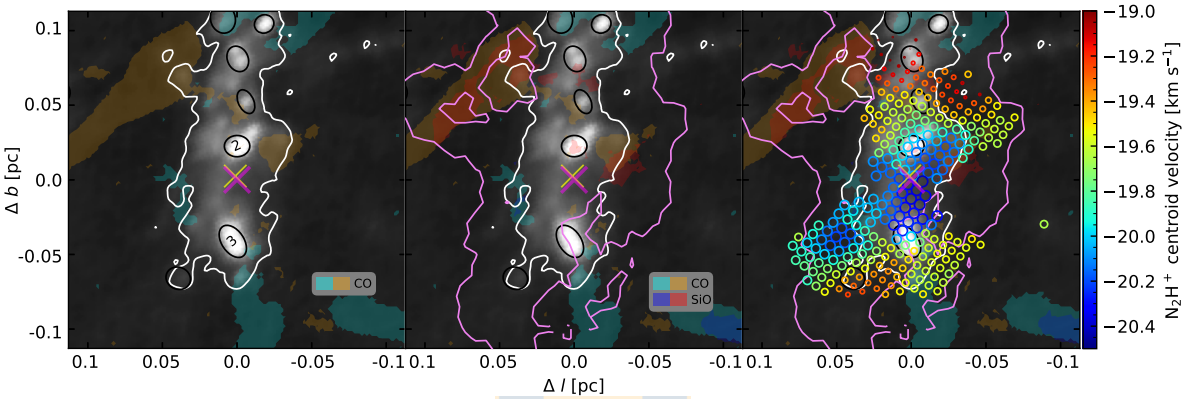

Figure 3.12: Multi-tracer diagram at the location of the main blue V-shape of G353 (§ 3.5.3). The different panels show the step by step construction of the final plot (right panel). **Left panel:** The black to white background shows the 1.3 mm continuum emission from Díaz-González et al. (2023). With black ellipses we show the 1.3 mm continuum cores from Louvet et al. (2023). With black text we indicate the IDs of the cores closest to the center of the V-shape, marked with a fuchsia "×". We indicate the barycenter of cores 2 & 3 (see Fig. 3.11) with a yellow "×". Filled contours represent the CO (2-1) emission in the velocity ranges of $-50\,\mathrm{km\,s^{-1}}$ to $-15\,\mathrm{km\,s^{-1}}$ (cyan) and $15\,\mathrm{km\,s^{-1}}$ to $50\,\mathrm{km\,s^{-1}}$ (beige), relative to the $\mathrm{V}_{LSR} = -17\mathrm{km\,s^{-1}}$ of G353. With a white contour we indicate the $log(N(\mathrm{H_2})\ \mathrm{cm^2}) = 23.3$. **Middle panel:** In addition to the left panel, we include the SiO $(5-4)$ emission with blue and red contours in the same (negative and positive) velocity range as with CO. The pink contour indicates the integrated intensity of the most blueshifted modeled $\mathrm{N_2H^+}$ Gaussian velocity component (see Fig. 3.9; blue distribution), at a value of $7\,\mathrm{K\,km\,s^{-1}}$. **Right panel:** With open circles we show the location of the data composing the main $\mathrm{N_2H^+}$ blue V-shape. The colors indicate their velocity centroid, and their (increasing) size indicates how close the gas velocities are to the velocity apex of the V-shape. This VG seems to converge to the barycenter of cores 2 & 3, and it is oriented along filament "F3".

presented on the right panel. These boxes are centered at the main blue V-shape, matching the area of this V-shaped structure (see Fig. 3.12). We show that the overall structure in PV space is conserved at different angles, excluding the possibility of this velocity feature being the result of projection effects.

For this V-shape we used its composing VGs to derive timescales as $t_{VG} = 1/\mathrm{VG}$, similar to the procedure for a rotating filament presented in Álvarez-Gutiérrez et al. (2021), and we suggest these can be interpreted as inflow timescales. The t_{VG} values for this V-shape range between $\sim\ 50 - 70\,\mathrm{kyr}$. These timescales are short compared to the $\sim 0.21\,\mathrm{Myr}$ free fall time (t_{ff}) of the protocluster (Motte et al., 2022), and a few times larger than the t_{ff} of nearby cores ($\sim 20\,\mathrm{kyr}$, within $0.1\,\mathrm{pc}$ of this V-shape). To determine the cores t_{ff}, we use the 1.3 mm core masses from Louvet et al. (2023).

We characterized eight more N_2H^+ V-shaped structures. In Fig. 3.13 we show the position of these V-shapes in the POS. Previous studies have detected VGs along filaments, toward a converging point (Pan et al., 2024; Peretto et al., 2014; Rawat et al., 2024). In the case of G353 we see that instead of detecting a single V-shape at the intersection of its filaments, the hub appears to be fragmented into multiple, small-scale V-shaped VGs. Only V-shapes "A", "D", and "E" are outside of the hub, with V-shape "D" located on top of filament "F3". This indicates that the V-shaped structures are not exclusive to the central parts of HFS, but are also present in comparatively isolated regions. We note that within a ∼beam size from the apex of V-shape "B" (see Fig. D.2), the continuum core "7" ($\sim 6\,\mathrm{M}_\odot$) is located.

In Henshaw et al. (2014), they propose two scenarios that might produce these V-shaped VGs (see their Fig. 12). One scenario suggests that gas in a filament is flowing toward a denser region (infall), while the other scenario suggests that a protostellar outflow moves the dense gas located in its vicinity. To analyze the different dynamical processes present in this region, we used the ALMA-IMF 12 m data of the shock, outflow tracer SiO (5−4), from Cunningham et al. (2023). From those data we created its intensity-weighted PV diagram, presented in Fig. E.1 (see Appendix E for more details). We note that there is almost no SiO emission nor outflow sources at the location of the N_2H^+ V-shape (see Fig. 3.12). The ΔV within $10''$ from this main blue V-shape is $\sim 40\,\mathrm{km\,s^{-1}}$, while for the whole SiO dataset is $\sim 80\mathrm{km\,s^{-1}}$, showing a clear difference in the SiO ΔV and the core velocities. Furthermore, the SiO ΔV is $\sim$ 10 times larger than the one of N_2H^+. This difference in traced velocities implies that these two molecules trace vastly different physical phenomena. We suggest that the small velocity range probed by N_2H^+ indicates that the VGs can be considered as infall signatures (see § 3.6). We discuss the possible morphology of the filaments hosting V-shapes in § 3.8.

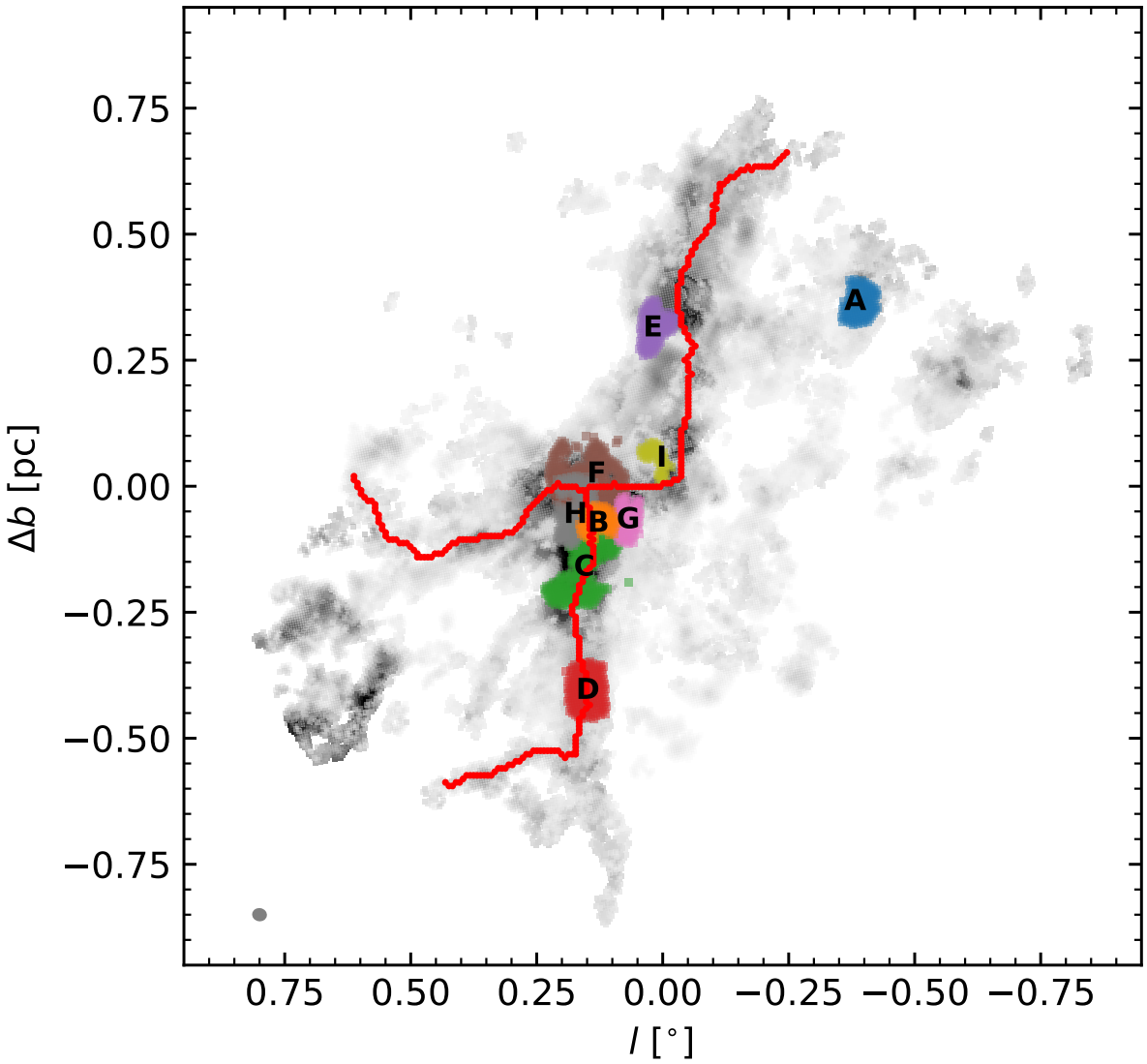

Figure 3.13: V-shapes location on the plane of the sky. We indicate the position of each V-shape with colored points and their ID with black text. With red lines we show the filamentary structure identified in § 3.3.2. In the background we show the integrated intensity map of all three velocity components, similarly as in Fig. 3.9. We see most of of the V-shapes are located at the hub.

3.6 G353 as a collapsing region

We used the SiO $(5-4)$ and CO $(2-1)$ data from Towner et al. (2024) and Cunningham et al. (2023) to identify possible outflows near the V-shape presented in Fig. 3.10. For CO we measured the RMS in the emission-free velocity range of 145 to 286 $\mathrm{km\,s^{-1}}$. We used only CO data with S/N > 3 for our analysis. The cleaning of the SiO data is described in Appendix E. In Fig. 3.12, with a fuchsia "×" we indicate the center of the V-shape from § 3.5.3, located between two 1.3 mm cores 2 & 3 (black ellipses), which present DCN velocity detections. From these diagrams we see there is neither SiO nor CO outflow detection at the location of the main blue V-shape $(\Delta l,\ \Delta b) = (0\,\mathrm{pc},\ 0\,\mathrm{pc})$. In the right panel we show the position of the data composing this V-shape, where the velocity peaks toward the center of this velocity feature.

We derived the mass-weighted mean position of the two cores (2 & 3) closest to the V-shape to determine their barycenter (yellow "×" in Fig. 3.12). We found that the difference between the center of the V-shape and the barycenter of these cores is $\sim 0.3''(\sim 600\,\mathrm{au})$, well below the beam size of the N_2H^+ data. A similar offset is also present in the intensity and velocity profiles along filaments from ATOMS data (Zhou et al., 2022, see their Fig. 6). This small spatial offset might suggest that the gas flowing in the V-shape is produced by the gravitational pull toward the barycenter of cores 2 & 3, where the N_2H^+ radial velocities peak. This interpretation is similar to the one proposed in Zhou et al. (2023) in their kinematic analysis of the G333 complex. They describe the V-shaped VGs as the result of gas funneling from the molecular cloud to clumps which is then funneled onto cores (see their Fig. 9) consistent with gravitational acceleration.

In Fig. 3.14 we show the mean spectrum of different tracers at the central position of the main blue V-shape. These spectra were measured over a circular region with diameter equal to the major axis of the N_2H^+ beam ($2.28''$; $\sim$ 0.02 pc). This circular area results in a coverage of 1.14 times the N_2H^+ beam, and ∼5.6 times the beams of the H_2CO, DCN, and $H_2{}^{13}CO$ data. We see N_2H^+ and H_2CO present double component spectrum with asymmetric peaks. Between these peaks we detect DCN and $H_2{}^{13}CO$ emission. The asymmetric spectrum present in N_2H^+ and H_2CO is consistent with the "blue asymmetry" spectral feature, usually interpreted as infall signature, suggesting that this region is under gravitational collapse (e.g., Anglada et al., 1987; Lee et al., 1999, 2001; Mardones et al., 1997; Smith et al., 2012). Based on the idea that the V-shapes are the result of flowing gas along filaments toward denser regions, the blue-asymmetry detected at the center of the main blue V-shape suggests that gravitational collapse is taking place at the apex of the V-shaped structure.

Regarding large scales, in the traditional PV diagram presented in § 3.5.1 (see Fig. 3.8), we see a clear velocity spread around $\Delta\ b\ \sim\ -0.1\,\mathrm{pc}$, also present in the top right panel of Fig. 3.9. Below we compare this velocity spread with the velocity distribution produced by infall, in which the gas velocities increase as the distance to the center of infall ("r") decreases:

$$V_{infall} \quad = \quad -\sqrt{\frac{2G\,M}{r}} \tag{3.2}$$

For this comparison, we modeled a sphere with a total mass of 150 $M_\odot$, a radius of 0.5 pc, and a power

law density profile described by:

$$\rho(r) \;=\; \rho_0 \left(\frac{r}{\mathrm{pc}}\right)^{-\gamma}, \;\; \gamma \;=\; 5.65, \;\; \rho_0 \;=\; 6.1 \times 10^{-5} \; \frac{\mathrm{M}_\odot}{\mathrm{pc}^3}. \tag{3.3}$$

We provide the derivation of $\rho(r)$ in Appendix F. $\gamma = 5.65$ was determined by visual inspection by comparing the obtained radial velocities of the model (see below), at different γ values, with the overall shape of the PV distribution.

We then estimated the infall velocity of each point, based on the cumulative mass distribution ("M") at any given distance to the center (Eq. 3.2). We obtain the radial component of the infalling velocities as:

$$V_r \;=\; V_{infall} \times \cos(\arctan(X/Z)), \tag{3.4}$$

in which X represents the horizontal coordinate in the POS, while Z represents the (unobserved) depth of the sphere. The spatial coordinates for this model range from -0.5 pc to 0.5 pc.

In Fig. 3.15, we show the coverage of the PV distribution from our model, described in Eqs. $3.2 - 3.4$, with a solid white line. We find good agreement between the PV distributions of our approach and the data. The PV distribution of our infall model is consistent with previous work that provide the expected PV distributions for spherical protostellar envelopes under infall (Tobin et al., 2012). At large scales, we interpret the agreement between the PV diagrams of our model and the data as protocluster scale collapse due to gravitational contraction. It is worth noting that the inferred mass from our model is ∼5.5 times lower than the one derived from the $N(\mathrm{H_2})$ map (Díaz-González et al., 2023). We speculate that a model considering complex processes such as turbulence, radiative transfer, and magnetic fields might solve this mass discrepancy while still matching the observed PV distribution.

3.7 Mass accretion rates in the V-shaped structure

Based on the idea that the V-shapes are a result of gas flowing toward cores, in this section we provide estimates of their mass accretion rates ($\dot{M}_{\rm in}$) for N_2H^+ and H_2.

3.7.1 H_2 mass accretion rate

Here we describe our approach for V-shape "C", and to ensure that we estimate the V-shape $M(H_2)$ on the area of this structure, we used the `CASA` task `imregrid` to obtain the continuum-derived $N(H_2)$ map from Díaz-González et al. (2023) at the resolution of the N_2H^+ data. We determined that in this V-shape the total $N(H_2)$ $\sim 1.17 \times 10^{26}$ cm^{-2} in an area of 0.013 pc^2. Here, we derived a $M(H_2)$ map using Eq. 3.5:

$$M(H_2) \quad = \quad 2 \times N(H_2) \times \mathrm{area_{pixel}} \times \mathrm{m_{proton}}, \tag{3.5}$$

from this $M(H_2)$ map we considered only the points that are part of the V-shape. To determine the mass associated with flowing motions we subtracted the core masses (from Louvet et al., 2023) that are located inside this V-shape. We note here that this mass map is an upper limit given that we do not apply a background correction. We obtained a total of $M(H_2)$ ~ 53 M$_\odot$. Considering $t_{VG\ mean}$ used in Eq. 3.8, we derived the $\dot{M}_{\rm in}$ (H_2) as:

$$\dot{M}_{in}(H_2) \ = \ \frac{M(H_2)}{t_{VG\ mean}} \ = \ 8.22 \times 10^{-4}\ \mathrm{M_\odot\ yr^{-1}}. \tag{3.6}$$

We used the procedure described above to estimate the $\dot{M}_{\rm in}$ (H_2) of the other eight V-shapes shown in Fig. D.2. We include these values in Table D.1. The average $\dot{M}_{\rm in}$ (H_2) of these V-shapes is 3.4×10^{-4} M$_\odot$ yr^{-1}. We note that V-shapes "H", "C", "F", and "B" present the largest $\dot{M}_{\rm in}$ (H_2) and they are located near or at the convergence point of the filaments (see Fig. 3.13)

For comparison, using the core masses from Louvet et al. (2023) we estimate the free-fall time of all 45 1.3 mm cores and their mass accretion rates. These values present large scattering, ranging from $(0.07 - 25) \times 10^{-4}$ M$_\odot$ yr^{-1}, with 28 of these cores presenting $\dot{M}_{\rm in}$ (H_2) $< 10^{-4}$ M$_\odot$ yr^{-1}. For cores 2 & 3, the average $\dot{M}_{\rm in}$ (H_2) is 15.5×10^{-4} M$_\odot$ yr^{-1}, about twice the $\dot{M}_{\rm in}$ (H_2) of the main blue V-shape, located between these two cores.

3.7.2 N_2H^+ mass accretion rate and relative abundance

To derive the N_2H^+ $\dot{M}_{\rm in}$ associated with the main blue V-shape (Fig. 3.10), we need to estimate its N_2H^+ mass. For this procedure we used `PySpecKit` with the `n2hp_vtau` fitter, to fit the full N_2H^+ line. The fitted parameters (see below) allow us to derive the $N(N_2H^+)$. The V-shape structure contains 77, 143, and 25 N_2H^+ spectra with one, two, and three velocity components, respectively. The bluest velocities in the three velocity component spectra accounts for ∼2% of the total number of velocities in this V-shape. For this reason, we modeled the full N_2H^+ hyperfine line structure with one and two velocity components. In Table 3.1 we list the parameters and ranges used for this procedure.

Table 3.1: N_2H^+ full line fitting parameter ranges.

Excitation temperature [K]	(T_{ex})	2.73 − 80
Opacity	(τ)	0.01 − 40
Centroid velocity [km s^{-1}]	(v)	−25 − 15
Velocity dispersion [km s^{-1}]	(Δv)	0.20 − 3

After obtaining the modeled N_2H^+ cube, we removed modeled components that presented $\tau_{\rm RMS}/\tau > 0.3$, in which τ and $\tau_{\rm RMS}$ represent the estimated opacity and its associated error, respectively. This criterion is to ensure that we use reliable fitted parameters to determine our $N(N_2H^+)$ values. For the fitting of two N_2H^+ components we only analyzed the most blueshifted component. The resulting opacities follow a log-normal distribution with a peak at $\tau = 0.13$.

We derived the $N(N_2H^+)$ of the V-shape by using Eq. 3.7 (Caselli et al., 2002b):

$$N(N_2H^+) = \frac{8\pi^{3/2}\Delta v}{2\sqrt{\ln 2}\lambda^3 A}\frac{g_l}{g_u}\frac{\tau}{1-\exp\left(-h\nu/k{\rm T_{ex}}\right)}\frac{Q_{\rm rot}}{g_l\exp(-E_l/k{\rm T_{ex}})}, \tag{3.7}$$

in which τ, T_{ex}, and Δv are the opacity, excitation temperature, and velocity dispersion, respectively, obtained from the full line fitting. The Planck and Boltzmann constants are represented by h and k, respectively, ν and λ are the frequency and wavelength of N_2H^+, A is the Einstein coefficient of the N_2H^+ (1−0) transition, g_l and g_u are the statistical weights of the lower and upper energy levels, E_l is the energy of the lower level, $Q_{\rm rot}$ is the partition function estimated using the excitation temperature of the full N_2H^+ fits (see Eq. A2 from Caselli et al., 2002b).

From the above procedure, inside the V-shaped structure, we get a total $N(N_2H^+) = 5.24\times10^{15}$ cm^{-2} and a total $M(N_2H^+) = 5.9\times10^{-8}$ M$_\odot$, within its extent of 0.013 pc^2. We used the average timescale of the VGs from § 3.5.3 (Fig. 3.10), $t_{VG\ mean} = 64.5$ kyr, to determine the $\dot{M}_{\rm in}$ (N_2H^+) as:

$$\dot{M}_{\rm in}(N_2H^+) = \frac{M(N_2H^+)}{t_{VG\ mean}} = 9.1\times10^{-13}\ {\rm M_\odot\,yr^{-1}}. \tag{3.8}$$

The $\dot{M}_{\rm in}(N_2H^+)$ estimate (and $\dot{M}_{\rm in}(H_2)$ below) should be multiplied by $\sin(\theta)$, in order to account for the unknown inclination angle (θ) of the protocluster/filaments relative to the POS.

For the main blue V-shape (Fig. D), we derived the N_2H^+ relative abundance $X(N_2H^+)$, using the N_2H^+ and H_2 column densities obtained above, as:

$$X(N_2H^+) = \frac{N(N_2H^+)}{N(H_2)} = 4.8\times10^{-11}. \tag{3.9}$$

The $X(N_2H^+)$ value obtained above appears lower than typical estimates in massive Galactic star-forming regions reported in different works ($[1.6-3.8]\times10^{-10}$; Caselli et al., 2002a; Henshaw et al., 2014, Sandoval-Garrido et al. in prep.). We consider it a good agreement taking into account the uncertainties of the involved measurements (i.e., column density estimates). For a comparison of the N_2H^+ relative abundance between regions composing the V-shapes and the rest of protocluster we would require to model the full N_2H^+ line emission in the whole region.

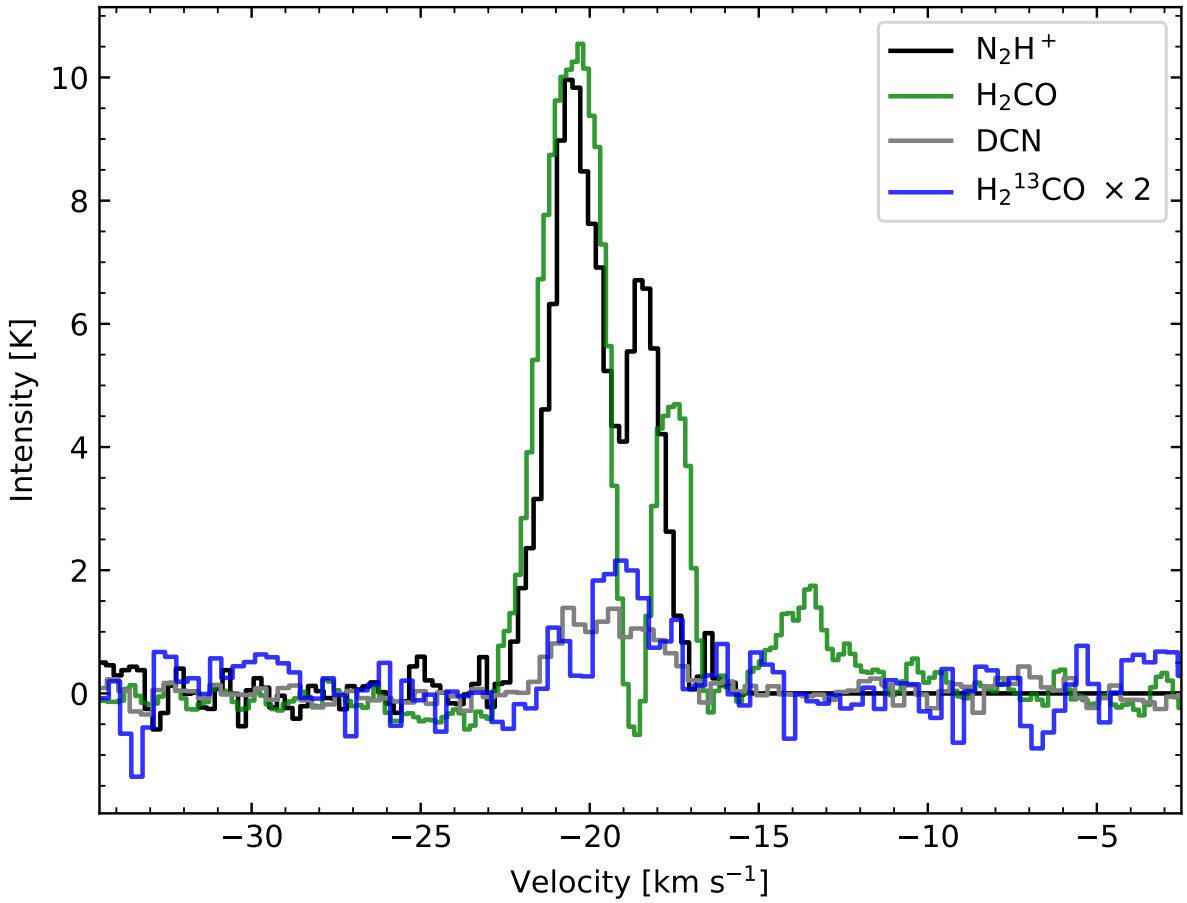

Figure 3.14: Mean spectra within a 1.14″ (∼ 0.01 pc) radius around the location of the main blue V-shape (pink "×" in Fig. 3.12). Both N_2H^+ and H_2CO show blue asymmetry, known to characterize infall motions. The difference in velocity between the two N_2H^+ peaks is ∼ 2.5 km s^{-1}.

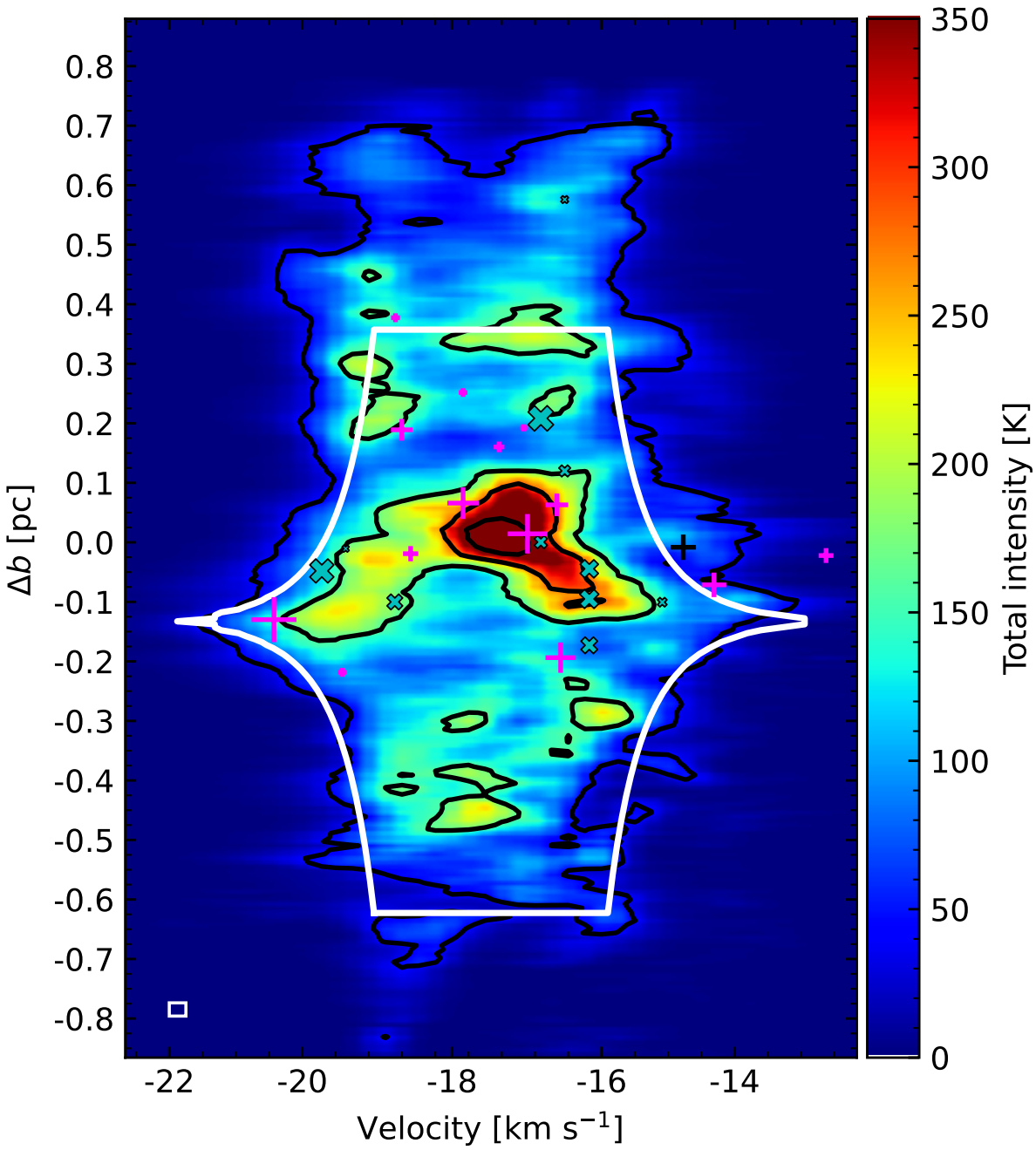

Figure 3.15: PV coverage of a gravitationally collapsing sphere. The white contour represents the coverage of the synthetic radial velocities derived from this model (§ 3.6). The background and cores are the same as in Fig. 3.8. For the modeled sphere we set its total mass to 150 $M_{\odot}$, within a radius of 0.5 pc.

3.8 Discussion

3.8.1 V-shaped velocity gradients in the literature

The V-shaped VGs described in this work have been detected across multiple Galactic star-forming system. Stutz & Gould (2016) introduced the Slingshot mechanism in the Integral Shaped Filament (ISF) located in Orion A. They show undulations of the region in both position and velocity, suggesting that these features appear to be ejecting protostars (see their Fig. 2). Furthermore, Stutz (2018) characterize a standing wave in the neighborhood of the ISF, consistent with the Slingshot mechanism. It is possible that the undulations in the works above might result in the observed V-shaped structures seen in different studies (see below). González Lobos & Stutz (2019) identify six evenly spaced (every ~ 0.44 pc) velocity peaks along the spine of the ISF in Orion A. They suggest that this periodicity is consistent with the wave-like perturbation in the gas caused by the Slingshot mechanism. In Álvarez-Gutiérrez et al. (2021) they analyze the L1482 filament located in the California Molecular Cloud. In all of the analyzed tracers there is a clear velocity peak in their north region (length ~ 1.8 pc, mass $\sim 10^3$ M$_\odot$). This subregion contains a higher gas density and higher number of YSOs compared to the more quiescent south part.

While the two regions described above are considered nearby (both at D $\lesssim 500$ pc), more distant regions also present these velocity features which we list below. Zhou et al. (2022) study the velocity profiles along filaments from the ATOMS survey (Liu et al., 2020b). The median mass of their sources is $\sim 1.4 \times 10^3$ M$_\odot$ with a median length of the filaments at $\sim$ 1.35 pc. By analyzing the H^{13}CO$^+$ (1−0) emission they find converging VGs along filaments (see their Figs. 6 & 10), which they also detected using simulations from Gómez & Vázquez-Semadeni (2014). These VGs at scales comparables to the V-shapes presented here are consistent with our VGs estimates (see their Fig. 7 & 8). In Zhou et al. (2023) they analyzed ^{13}CO (2−1) APEX/LAsMA data of the G333 complex. They identify multiple V-shaped VG (see their Fig. 7) which they describe as the PV projection of a funneling structure in PPV space (see their Fig. 9). The origin of this structure is due to material inflowing toward the central hub and also due to gravitational contraction of star-forming clouds or clumps.

Redaelli et al. (2022) use ALMA N_2H^+ (1−0) isolated component data of the high-mass (5200 M$_\odot$) clump AGAL014.492-00.139 identifying multiple coherent structures in PPV space (trees "B" and "G"; right panel of their Fig. 7 & 9). These are characterized by multiple undulations, and possible V-shaped VGs. For their "G" PV distribution, they suggest that one scenario is where the dense gas is flowing along the filament (of length ~ 0.2 pc) from protostar "p3" toward the protostar "p2". This motion has an $\dot{M}_{\rm in} = 2.2 \times 10^{-4}$ M$_\odot$ yr^{-1}, being in the range of the $\dot{M}_{\rm in}$ we derive for our VGs (see Table D.1).

In Rawat et al. (2024) they analyze ^{13}CO(1−0) data obtained with the Purple Mountain Observatory, as part of the Milky Way Imaging Scroll Painting survey. They detect a V-shaped VG (see their Fig. 14) along the ridge of the G148.24+00.41 (G148) cloud. This V-shape peaks toward the dense clump at the center of this region, possibly indicating gas inflow along their filaments F2 and F6 toward the hub. The length of the V-shape in G148 is ~ 15 pc, while our most prominent V-shape (Fig. 3.10) is $\sim$ 0.2 pc. Also the masses and lengths of their identified filaments are (1.3 to 6.9) $\times 10^3$ M$_\odot$ and 14

to 38 pc, respectively, large compared to the total mass (2.5×10^3 $M_\odot$) and extent of G353 (~ 1.2 pc). This difference in probed lengths and masses might be reflected by their mean VG ~ 0.05 km s^{-1} pc^{-1}, ~ 2.5 orders of magnitude smaller than our VGs. This is consistent with the analysis presented in Zhou et al. (2022, 2023), in which they observe an inverse relation between the spatial scale of a region and their VGs (see their Fig. 8).

In Pan et al. (2024) using APEX $C^{18}O$ (2−1) data of the filamentary cloud G034.43+00.24 (G34) they identify converging VGs of lengths ~ 1 pc toward the "middle ridge" see their Fig. 3, top panel). They interpret these VG as gas flowing from the filaments onto dense clumps, located at the center of G34. These VGs of their southern and northern filaments are in the range of $\sim 0.3 - 0.4$ km s^{-1} pc^{-1}, and they estimate the total mass inflow rate toward the middle ridge as $\sim 5.5 \times 10^{-4}$ $M_\odot$ yr^{-1}, similar to our $\dot{M}_{\rm in}$ estimates.

Current work by Sandoval-Garrido et al. (in prep.) in G351.77 (intermediate protocluster, located at 2 kpc; Motte et al., 2022; Reyes-Reyes et al., 2024) use a similar analysis as we present in this work, in which they identify multiple V-shaped velocity structures. In Salinas et al. (in prep) they analyze the kinematics of the evolved protocluster G012.80 (located at 2.4 kpc; Motte et al., 2022), in which they implement similar techniques and find velocity signatures of filamentary rotation.

3.8.2 Filamentary 3D morphology

V-shaped VGs appear to be a generic feature across a wide range of star-forming environments, probing VGs with differences of up to ∼two orders of magnitude in spatial scales ranging from 0.1 to ∼10 pc. Despite being commonly detected in recent studies, it is still not clear how they are produced. Henshaw et al. (2014) highlights the degeneracy regarding the opposite interpretations of these V-shaped velocity structures. They suggest that these VGs can be a signature of gas flows along kinked filaments toward a core located at their convergence point. From our analysis regarding the most prominent V-shape (see § 3.5.3 & 3.6) we see that no core is located at its apex, although cores 2 & 3 are within ~ 0.05 pc. Also the spatial offset between the center of the V-shape with the barycenter between these two cores is ~ 600 au. This is consistent with the idea of small-scale gravitational collapse within the protocluster, similar to clump decoupling from their parent molecular cloud (Peretto et al., 2023). Based on this, we conclude that cores may be located in the vicinity of the velocity apex, and not necessarily on top of it. This gas flows toward denser regions may result in the formation of high-mass cores in later stages during the evolution of the protocluster.

Regarding the kinked morphology of the regions hosting V-shapes, one scenario regarding magnetized shocks is presented in Inoue & Fukui (2013) and Inoue et al. (2018). They use magnetohydrodynamics simulations to characterize the interaction of molecular clouds and a magnetized shock produced by a cloud-cloud collision. They find that the shock layer decelerates as it collides with denser regions. This deceleration reshapes the shock layer to be oblique, leading to the formation of kinked filaments and converging flows, which are oriented toward the apex of these filaments. They predict that magnetic fields present in the region should be perpendicular to these filaments and bend with the shock around the filament (Inoue et al., 2018, see their Fig. 3). In Bonne et al. (2020) and Bonne et al. (2023) they propose that this scenario takes place in the Musca and the DR21 filaments.

In both of these regions they detect V-shaped VGs which they suggest are the result of cloud-cloud collisions bending the magnetic field (Bonne et al., 2020, see their Fig. 22 & 23). Further observations of magnetic field polarization in the POS, along with information along the line of sight is required to evaluate these models.

Another possibility is that these kinked structures could be caused by mechanisms such as the Slingshot. This mechanism proposes a standing wave, longitudinal gravitational instabilities, or large-scale oscillations possibly caused by a possibly helical magnetic field morphology, causing ejections of protostars and protoclusters from their maternal filament (Liu et al., 2019; Stutz, 2018; Stutz et al., 2018; Stutz & Gould, 2016).

A different interpretation is that they are the product of out-flowing material coming from a forming protostar interacting with the surrounding dense gas (see their Fig. 12). To shed light into this degeneracy in G353 we compare the N_2H^+ (dense gas tracer) radial velocities and SiO (shock/outflow tracer) as a proxy for energies. The velocity range ΔV covered by the N_2H^+ emission is $\sim 8\,\mathrm{km\,s^{-1}}$, while for SiO is $\sim 80\,\mathrm{km\,s^{-1}}$. Given the difference in probed velocities between SiO and N_2H^+ (see § 3.5.3) and the analysis presented in § 3.6 we suggest that the V-shapes in G353 are a signature of infall.

The multiple VGs that conform the V-shapes present in G353 have values of $\sim$ 8 to $\sim$ 31 $\mathrm{km\,s^{-1}\,pc^{-1}}$, with timescales ranging from $\sim$ 35 to 173 kyr, and $\dot{M}_{\rm in}$ values ($\sim$ 0.4 − 9) × 10^{-4} $M_\odot$ $\mathrm{yr^{-1}}$. These values are similar to VGs in other regions with comparable sizes and masses. In G353 it is likely that these VGs are the result of dense gas moving through filaments, possibly increasing the density of the central regions, shaping the overall velocity field at large and small scales, and leading to a further increase in the core population and star formation activity.

3.8.3 Timescales and mass accretion rates

One important aspect of the V-shapes that is still not well understood is the timescale associated with the VGs (t_{VG} = $\mathrm{VG^{-1}}$). It is not clear if nor how these timescales determine core formation lifetimes or impact the star formation environment in general. In our sample of V-shapes the timescales are in tens of kyrs with the average value of $\sim$ 67 kyr, $\sim$ two times the cores t_{ff}, while the t_{ff} of the whole protocluster is $\sim$ 0.21 Myr. In Rawat et al. (2024) they estimate the longitudinal collapse timescales for their filaments, being in the range of $5 - 15$ Myr. Using their derived VGs we estimate their associated timescales to be between $\sim$ 16 and $\sim$ 50 Myr, $\sim$ one to two orders of magnitude larger than our small-scale V-shapes timescales. We suggest that the VG timescales might serve as an upper limit for filamentary collapse timescales. In Zhou et al. (2022) they determine gas accretion times as a function of the lengths of their filaments, assuming that the VGs produced by gas inflow (see their Fig. 11). At filament lengths comparable to our V-shapes ($\sim$ 0.1 pc) their gas accretion timescales are on the order of our estimates (see Table D.1).

3.8.4 Depletion timescales

It is also interesting to consider the mass accretion rates measured here compared to the available protocluster mass reservoir to explore implications for the duration of the gas dominated phase. The total mass accretion rate of our V-shaped structures is $\dot{M}_{\rm in,\ Tot} = 3 \times 10^{-3}\,{\rm M}_{\odot}\ {\rm yr}^{-1}$ (see Table D.1). Considering the total mass ($\rm M_{Tot}$) of G353 as a mass reservoir, we estimated the depletion timescale (t_{dep}) as the time needed fully consume the gas. Here we assumed that $\dot{M}_{\rm in,\ Tot}$ is representative of flows feeding gas onto cores. We estimated $t_{dep} = {\rm M_{Tot}}/\dot{M}_{\rm in,\ Tot}$, in which the total mass of the region is $2500\,{\rm M}_{\odot}$ (Motte et al., 2022). We obtained a $t_{dep} = 0.8\,{\rm Myr}$, of similar magnitude but about four times larger than the t_{ff} of the protocluster. Considering that our estimate of $\dot{M}_{\rm in,\ Tot}$ is certainly a lower limit (see discussion above), the actual value value of t_{dep} is likely to be shorter, so closer to the free-fall time estimate. Given that the protocluster does not appear to be in a state of free-fall (see § 3.6) but instead undergoing comparatively slow gravitational contraction, the similarity in these relatively crude estimates seems remarkable. While we do not yet have an explanation for why relatively good match in timescales, it would seem to indicate that protocluster evolution may be a self-regulating process. Larger samples and similar analysis will test this hypothesis.

Moreover, the approximate concordance of t_{dep} and t_{ff} may indicate that the "phase transition" of protocluster gas mass being converted into stellar mass could contribute a relevant "negative pressure" counteracting effects of, for example, feedback over the lifetime of the protocluster.

Chapter 4

Complementary and ongoing projects

4.1 L1482

In Álvarez-Gutiérrez et al. (2021) we characterized part of the L1482 filament located in the California molecular cloud (CMC; see Fig. 4.1). Using *Herschel* continuum data we derived a $N_{\rm H}$ from which we derived mass density profiles. We concluded that L1482 as a whole is less dense than other active star forming regions such as Orion and it can be separated into the north and south subregions. The north region, compared to the south, hosts most of the YSOS of the probed area and it presents a higher line mass density profile.

We used the IRAM 30m radiotelescope to probe the kinematics in this region, tracing dense and diffuse gas (N_2H^+, HNC, HCO^+, $C^{18}O$). We implemented the intensity-weighted PV diagram technique developed by González Lobos & Stutz (2019) (right panel in Fig. 1.2). With this approach we remove the noise in the diagram, increase the visibility of the small scale structures in PV space, and maintain the large scale distribution detected in the traditional PV diagram (left panel in Fig. 1.2). Where in the south we found a VG consistent with filamentary rotation. We characterized this velocity feature and derived the expected centripetal acceleration and compared it to the gravitational acceleration. We found that rotation opposes gravity at scales close to the spine of the filament ($r < 0.25\,{\rm pc}$) and it dissipates at larger scales.

We concluded that L1482 has not reached the densities required to trigger active star formation at the level observed in environments of similar masses such as Orion. Processes such as helical magnetic fields may induce filamentary rotation, opposing gravitational collapse, and halting star formation.

In 2020 we mapped the southern extent of L1482 (red boxes in Fig. 4.1). We carried out these observations in pool mode during during three weeks in the months of January, March, and April. For the 2^{nd} and 3^{rd} weeks of observations, the E090 band in the FTS backend presented a -320 MHz shift in the LSB-LO frequency coverage. This resulted in the lack of frequency coverage for the HNC (1-0) emission at 90.663574 GHz. We calibrated and imaged these new observations using the same approach as in Álvarez-Gutiérrez et al. (2021).

In the right panel of Fig. 4.1 we show the integrated intensity map of the whole $C^{18}O$ dataset.

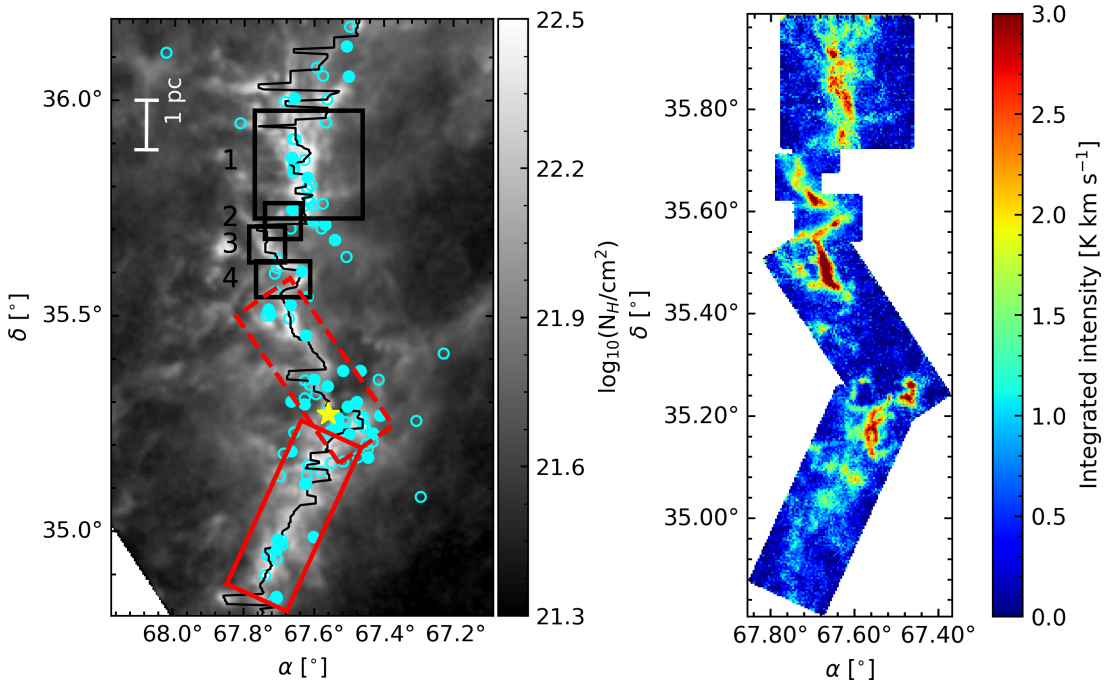

Figure 4.1: **Left:** $N_{\rm H}$ map of the L1482 filament located in the California molecular cloud. We indicate the extent of the north and south regions with white vertical lines. The black boxes indicate the area probed by the IRAM 30m radiotelescope in Álvarez-Gutiérrez et al. (2021). The red boxes indicate the regions mapped in our last observations. The filled (open) cyan circles indicate YSOs with (without) GAIA astrometry. The LkHα B star is indicated with a yellow star. We indicate the spine of the filament with a black line. **Right:** $C^{18}O$ integrated intensity map inside the areas indicated in the boxes from the left panel. We see that around $\delta \sim 35.30°$ the L1482 filament presents a discontinuity, probably associated to the NGC 1579 star cluster.

These recent observations show a large discontinuity between $35.24° < \delta < 35.40°$. Most of this area coincides with the YSOs over-densities associated to the NGC 1579 star cluster, where the B star lhkα 101 is located. It is possible that the filament collapsed into these YSOs originating the observed discontinuity in $C^{18}O$. Another scenario is that this part of the filament was disrupted from stellar winds of the lhkα 101 B star by pushing, dispersing, and ionizing its molecular gas.

We modeled the $C^{18}O$ and HCO^+ data with two Gaussian velocity components using `PySpecKit`. The parameter space for the peak intensity, velocity centroid, and velocity dispersion is [0.24 K, ∞], [$-2.5\,{\rm km\,s^{-1}}$, $1\,{\rm km\,s^{-1}}$], [$0.133\,{\rm km\,s^{-1}}$, $2\,{\rm km\,s^{-1}}$], respectively. From the resulting fitted parameters we flag spectra that present velocity components that are within 3 channels widths from each other, peak intensity is lower than three times the rms of their spectrum, and the intensity uncertainties are larger than 50 %. These constraints are set to ensure that our fitting results are robust, where we refit the flagged spectra with one velocity component. For this new single component fit we use the parameter space defined before and we merge the results with the double component fitted cube. For N_2H^+ we use the "`n2hp_vtau`" hyperfine component fitter of `PySpecKit`. The parameter space for the excitation temperature (T_{ex}), opacity (τ), velocity centroid, and velocity dispersion is [2.73 K, 50 K],

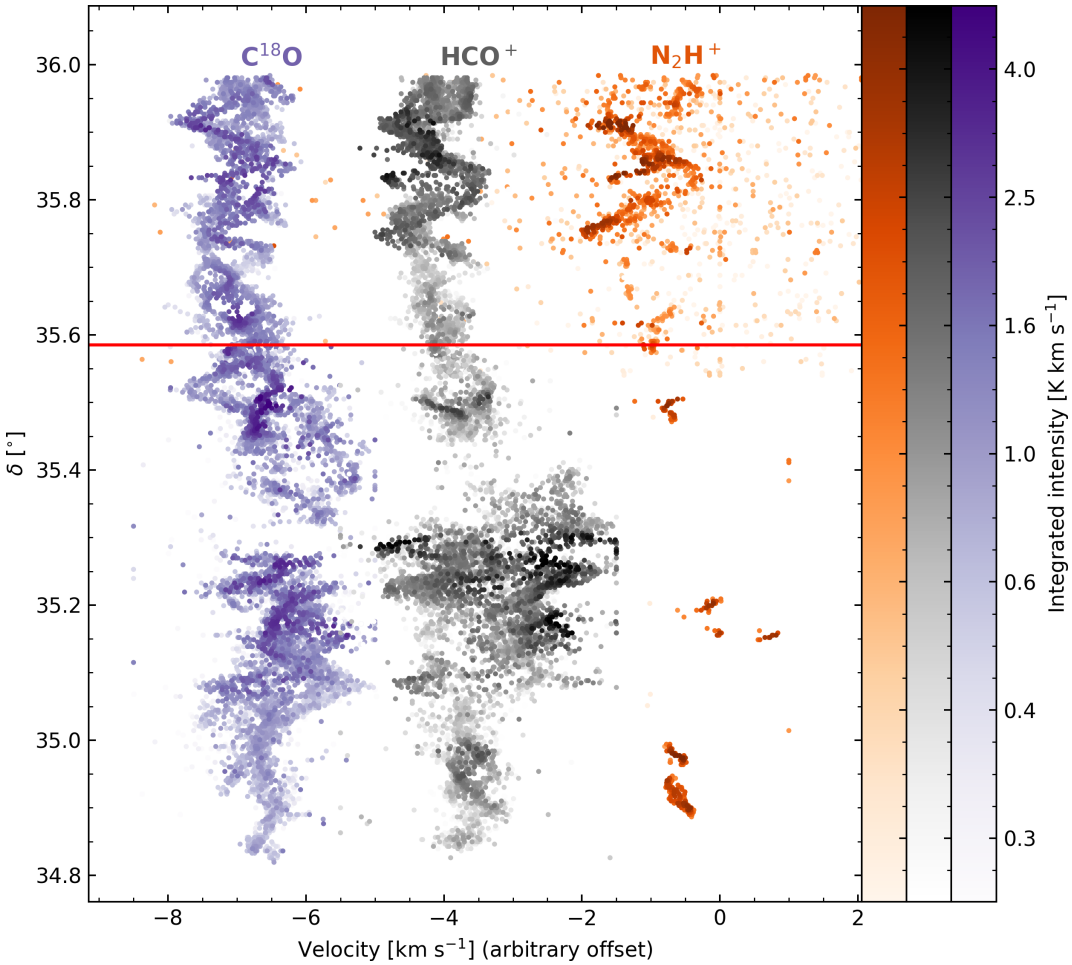

Figure 4.2: Intensity-weighted position-velocity diagram of L1482 using IRAM 30m data. With a red solid line we indicate the extent of the previous (north) and recent (south) observations. We note a remarkable lack of dense gas traced by N_2H^+ as well as a common filamentary discontinuity seen across all tracers around $\delta \sim 35.3°$. There is possibly a large V-shape in $C^{18}O$ and HCO^+ at $\delta \sim 35.1°$.

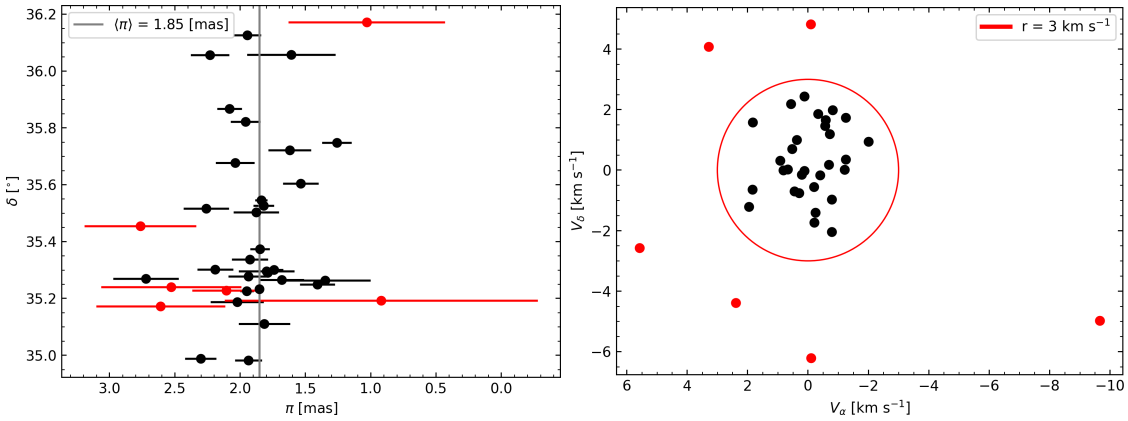

Figure 4.3: **Left:** Gaia parallax distribution as a function of declination. **Right:** Gaia-derived YSOs velocities in the POS. We estimate the average velocity on each axis using the clustered YSOs only (in black) and subtract it from the sample. We see that the outliers (in red) presents large parallax uncertainties and velocities compared to the main sample (in black).

[0.01, 50], [$-2.5\,\mathrm{km\,s^{-1}}$, $1\,\mathrm{km\,s^{-1}}$], and [$0.13\,\mathrm{km\,s^{-1}}$, $2\,\mathrm{km\,s^{-1}}$], respectively. In these results we found large uncertainties ($\Delta\tau/\tau > 1$) in our opacity estimations, probable caused by the limitations from the `n2hp_vtau` fitter, where there are degeneracies between the possible values for both the excitation temperature and opacity. We refit the N_2H^+ spectra with large uncertainties in the opacity, fixing their excitation temperature to 12.46 K, the mean T_{ex} value from the fits that do not present this issue. We merge these results with the previous fit obtaining a fully modeled N_2H^+ cube.

Using the modeled cubes described above we create tables containing the coordinates, the intensity, and velocity centroid of each velocity component. In Fig. 4.2 we show the intensity-weighted PV of the whole L1482 dataset for $C^{18}O$, HCO^+, and N_2H^+. In $C^{18}O$ and HCO^+ there a few PV distribution that resemble the V-shaped structures seen in Álvarez-Gutiérrez et al. (2024). These are located at $\delta = 35.3°$, $35.3°$, and $35.1°$. We note a lack of dense gas traced by N_2H^+ at higher levels compared to $C^{18}O$, where there are only a few regions of localized N_2H^+ emission. One possibility is that the filament already used the dense gas to form stars, as we would expect in the case of the NGC 1579 star cluster. Another possibility is that the south region of L1482 presents multiple stages of star formation, where in some parts the density of the filament increased, leading core and star formation through filamentary collapse, while other nearby regions have not reach high enough densities to trigger star formation.

We crossmatched the YSO catalog from Lada et al. (2017) with the GAIA DR3 (Gaia Collaboration et al., 2023) and APOGEE (Majewski et al., 2017) detections in order to obtain the radial velocities of the compact sources located in the L1482 filament. For the crossmatch between these catalogs we use a conservative maximum spatial offset between the sources of 0.5″. At the end we obtain GAIA astrometry and APOGEE radial velocities for 36 YSOs in L1482. We find that most of our sample is clustered within a radius of $1.2\,\mathrm{mas\,yr^{-1}}$ from the mean proper motion on each axis. Six outlier sources present proper motions larger the $1.2\,\mathrm{mas\,yr^{-1}}$ radius. We derive an error weighted mean parallax to L1482 of 1.85 ± 0.14 mas, in a similar manner as presented in Álvarez-Gutiérrez et al. (2021). We

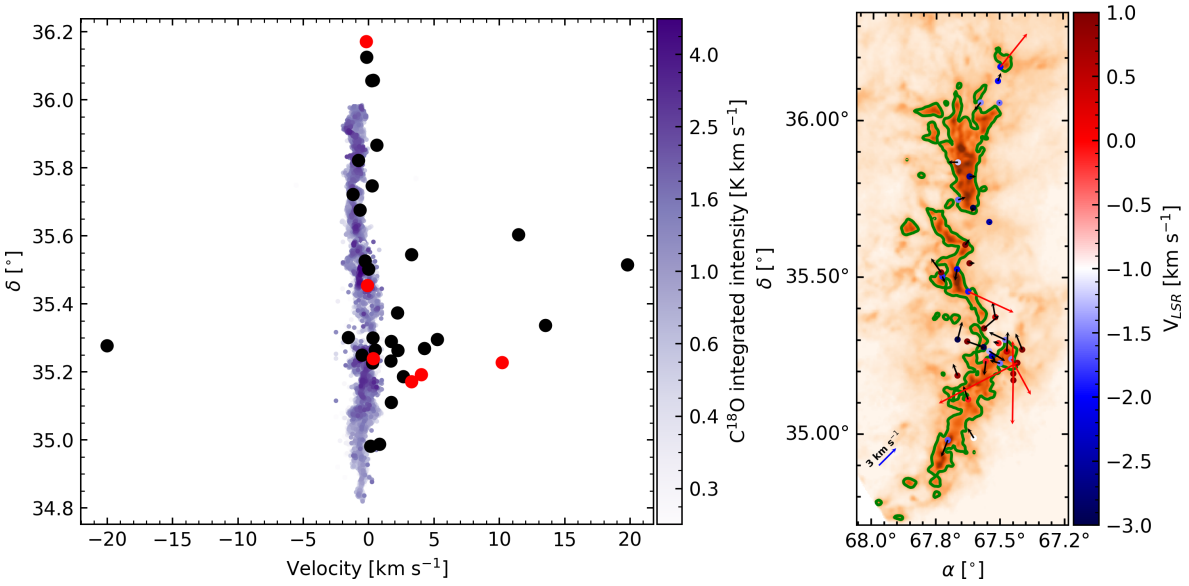

Figure 4.4: **Left:** $C^{18}O$ PV diagram including YSOs velocities from APOGEE. Most of the YSOs match the gas velocities traced by $C^{18}O$, where some sources clump near the location of NGC 1579, in which the filament presents a discontinuity. **Right:** N_H column density map of L1482. We indicate the YSOs POS velocities with arrows. With colored solid circles we indicate their radial velocity relative to L1482 ($V_{LSR} = -1\,km\,s^{-1}$). The YSOs velocities present large scatter near the location of the star cluster. Green contour indicates a $N_H = 10^{22}\,cm^{-2}$.

exclude these outliers for this parallax estimate. Using the parallax value estimated above we derive a distance to L1482 of $539.5^{+44.75}_{-38.39}$ pc. We convert the proper motion of these sources to velocities using this distance estimate. We derive the V_{LSR} of each YSO using the heliocentric radial velocity from APOGEE and the relation presented in Reid et al. (2009). In Fig. 4.3 we show parallax distribution as a function of declination and the derived velocities in the POS. We represent the outliers described above with red markers.

We compare the estimated YSOs V_{LSR} with the gas velocities traced by $C^{18}O$. We find that most of the YSOs match the gas velocities and some are clumped at the location of the discontinuity, where the NGC 1579 star cluster is located (Fig. 4.4, left panel). We present the location and velocities in the POS of the YSOs in the right panel of Fig. 4.4. Most of our sources are located in the south extent of L1482, with large scatter in the velocities at the location of the star cluster. On average the sources in the region of the star cluster present radial velocities of $\sim 2\,km\,s^{-1}$, redshifted compared to the V_{LSR} of L1482 of $-1\,km\,s^{-1}$. This could imply that the star cluster is in the process of being detached from the filament, possibly being caused by internal interactions in the cluster.

4.2 Vela

We used the APEX 12m radiotelescope with the nFLASH receiver and its 230 GHz band to map the central region of Vela. With this band coverage we were able to detect $C^{18}O$, ^{13}CO, and ^{12}CO, all

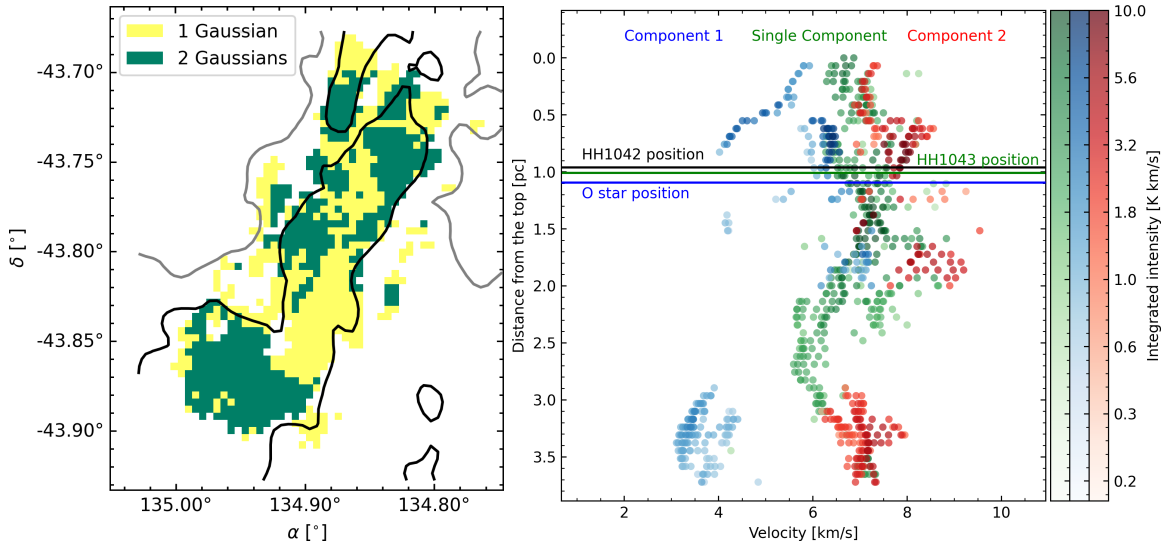

Figure 4.5: **Left:** Spatial distribution of the number of velocity components for the APEX $C^{18}O$ data. Yellow and green areas represent spectra with one and two velocity components, respectively. Grey and black contours indicate $\log(N_H)$ column densities of 22.1 and 22.4 respectively. We see that most the central region of Vela is well characterized by one velocity components, while the outskirts and the south region is better described by two velocity components. **Right:** Intensity-weighted PV of the central region of Vela. With green points we represent the spectra characterized with one velocity component. Blue and red points indicate the blue- and red-shifted emission of the two velocity components spectra. We indicate the projected location of the O star, as well with other objects in the RCW star cluster, with horizontal lines. We see a few twists in the PV distribution along the filament, at around 1.5 and 2.6 pc from the top of the region.

J = 2 − 1 transitions. We divided these observations into two main areas. We first mapped Vela C, indicated with a gray contour in Fig. 4.6, in the APEX project ID C-0108.F-9701C-2021. The southern area (white contour in Fig. 4.6) was mapped in collaboration with Friedrich Wyrowski, by mapping small subregions as part of backup observations, where weather constraints did not allow higher frequency observations. We imaged the $C^{18}O$, ^{13}CO, and ^{12}CO using scripts provided by the observatory staff.

By visually inspecting the $C^{18}O$ data, we determined that these observations are well characterized by spectra with one and two velocity components. For our kinematics analysis we started with the modeling of the $C^{18}O$ data using `PySpecKit` to fit up to two Gaussians. For both Gaussian components we defined the parameter space of the intensities and velocity dispersion as [3×RMS, 10 K] and [2.5 × Δv, 0.8 km s^{-1}], respectively. The RMS was measured in the emission-free velocity range of -33.84 km s^{-1} to -2 km s^{-1}, it presents a log-normal distribution and it peaks at 0.11 K, the value used for the intensity constraint. Δv represents the spectral resolution of the $C^{18}O$ data, which in this case is 0.16 km s^{-1}. For the centroid velocities we we defined the ranges of [2 km s^{-1} to 6.6km s^{-1}] and [4.8km s^{-1} to 8km s^{-1}] for the first and second velocity component, respectively.

In order to improve our fitting results we clean our modeled cube by identifying which fits are not reliable, refit these flagged problematic fits, and fit them with only one velocity component. The

cleaning mentioned above consists on applying a few criteria, these are:

- Velocity components should have uncertainties other than zero. The imposition of two velocity components leads to sometimes adding "ghost" components. These forced velocity components are characterized by their intensities presenting uncertainties equal to zero.
- The uncertainties of the intensity and velocity dispersion should not be higher than 45%.
- We also ensure that both velocity components should be separated by at least eight channel widths.

After flagging these spectra we fitted them with only one velocity component using the same velocity space we defined for the intensity and dispersion of the two velocity component fit. For the centroid velocity we defined a wider parameter space that covers part of both velocity components, that is from $1\,\mathrm{km\,s^{-1}}$ to $11\,\mathrm{kms}$. After obtaining this single component fit we inserted them in the modeled cube of two velocity components. We show the number of components for each $C^{18}O$ spectrum in Fig. 4.7. We see that there is an almost equal distribution of spectra with one and two components. The main filament appears to be described with only one velocity component, while the north and south extent are better described with two velocity components. We see a few twists in the velocities along the

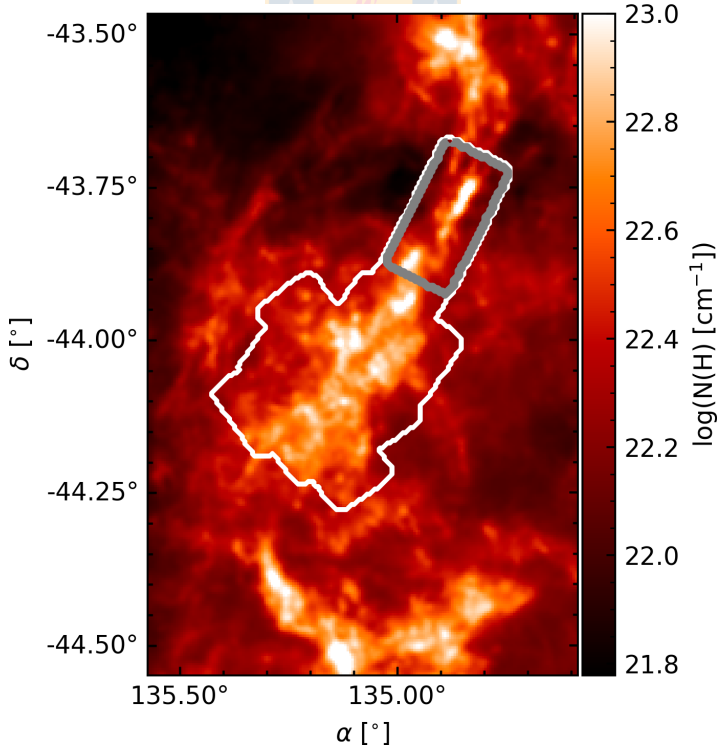

Figure 4.6: Mapped area of Vela using the APEX 12m radio telescope. The background shows the N_{H} column density map derived from *Herschel* data. The central region of Vela is indicated with a gray contour while the whole mapping, including the south coverage is shown with a white contour.

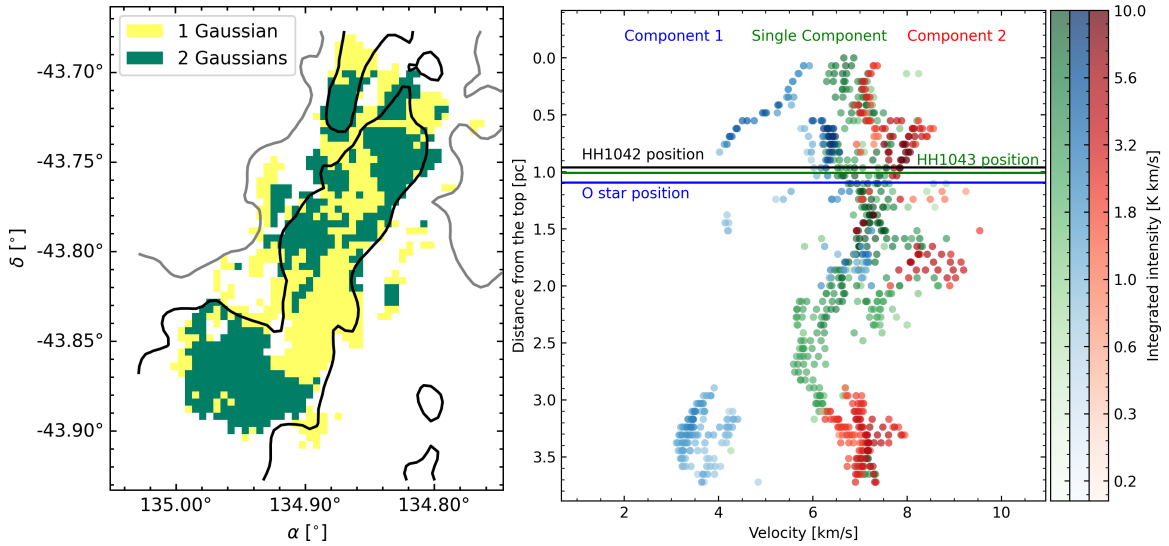

Figure 4.7: **Left:** Spatial distribution of the number of velocity components for the APEX $C^{18}O$ data. Yellow and green areas represent spectra with one and two velocity components, respectively. Grey and black contours indicate $\log(N_H)$ column densities of 22.1 and 22.4 respectively. We see that most the central region of Vela is well characterized by one velocity components, while the outskirts and the south region is better described by two velocity components. **Right:** Intensity-weighted PV of the central region of Vela. With green points we represent the spectra characterized with one velocity component. Blue and red points indicate the blue- and red-shifted emission of the two velocity components spectra. We indicate the projected location of the O star, as well with other objects in the RCW star cluster, with horizontal lines. We see a few twists in the PV distribution along the filament, at around 1.5 and 2.6 pc from the top of the region.

filament, that might be consistent with infall signatures (i.e., V-shaped structures Álvarez-Gutiérrez et al., 2024).

During 2022 we extended our original coverage towards the south of Vela. These observations were combined with the original measurements and we imaged all three tracers mentioned above. We estimated the RMS of the $C^{18}O$ cube by measuring the standard deviation along the spectral axis in the velocity range from 22 km s^{-1} to 11.5 km s^{-1}. We estimated the S/N map by dividing the peak intensity along the cube by the RMS (see Fig. 4.8). Using `SpectralCube` we determined the $C^{18}O$ moment zero and moment one maps in the velocity range between 1 km s^{-1} and 10 km s^{-1}. We show the first two moment maps in the middle and right panels of Fig. 4.8. From the integrated intensity map we see that we detect the filament continuity from the north towards the south of Vela. From the velocity centroid map we identify a velocity gradient in which velocities increase from south to north. This VG might suggest longitudinal gas flows towards the north of Vela, where the star cluster RCW 36 is located. Future analysis regarding the PV distribution is required in order to characterize and set constraints on this VG.

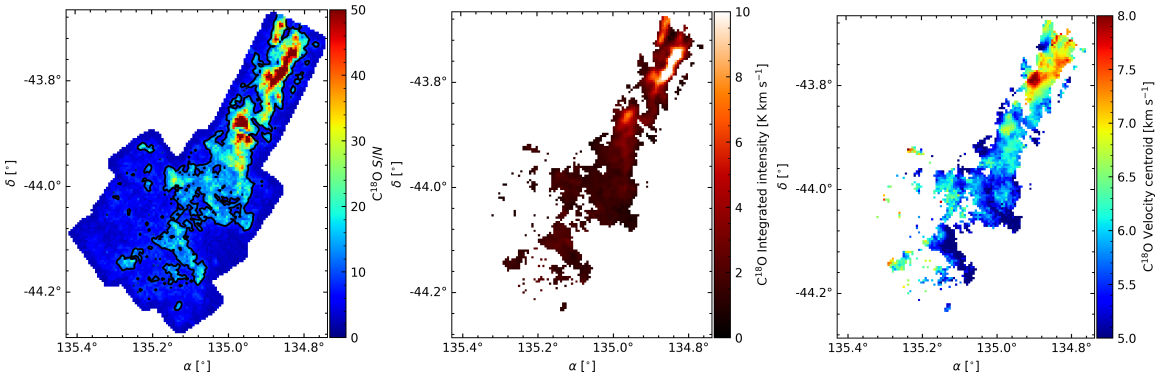

Figure 4.8: Maps derived from the $C^{18}O$ APEX Vela data. **Left:** We show the S/N map of the combined observations. With a black contour we indicate data with high S/N ($\geq$ 10). **Middle:** Moment zero map of the high S/N $C^{18}O$ data . From the integrated intensities we see that we are able to detect the filamentary continuity from north to the south area mapped in our most recent observations. **Right:** Moment one map using high S/N $C^{18}O$ data. We see a velocity gradient present along the filament, where velocities increase from south to north. This might suggest gas flows along the filament towards the star cluster RCW 36. For these diagrams we only use data with $S/N \geq 10$ (black contour).

4.3 Line-mass profiles of G353 and Vela

In order to compare different star forming filaments we estimated the line-mass (M/L) profile of the G353 parent filament as well as in the central region of Vela. From this approach we get a sense of their relative densities, which might be associated to their relative evolutionary state.

We implemented the procedure presented in Álvarez-Gutiérrez et al. (2021) to measure the mass distribution along both of these filaments. Specifically for Vela we only analyze the area mapped by our first APEX observations (gray area in Fig. 4.6). We started by converting the *Herschel*-derived $N_{\rm H}$ map of each region to mass units using distances of 2 kpc and 933 kpc for the G353 filament and Vela, respectively (Fissel et al., 2019; Motte et al., 2022). As presented in the left panels of Figs. 4.9 & 4.10, the mass distribution in both regions presents symmetry in along the parallel and perpendicular directions relative to the filamentary structures. From these symmetries we assume cylindrical morphology for these structures and we then estimate the M/L profiles, $\lambda(w)$, as presented in Álvarez-Gutiérrez et al. (2021); Reyes-Reyes et al. (2024); Stutz & Gould (2016). In the right panels of Figs. 4.9 & 4.10 we show the M/L distributions in black and the linear fits in red. From these fits we obtain the M/L profiles of G353 and Vela. We present the $\lambda(w)$ for both regions below:

$$\lambda(w)_{G353\ filament} = 1937.71 \left(\frac{w}{\rm pc}\right)^{0.54} \tag{4.1}$$

$$\lambda(w)_{Vela} = 560.16 \left(\frac{w}{\rm pc}\right)^{0.48}, \tag{4.2}$$

in which w indicates the radial distance from the filament ridgeline projected in the POS. From Eq. 4.1 we see that the M/L profile of the G353 filament is about four times denser and steeper than in Vela

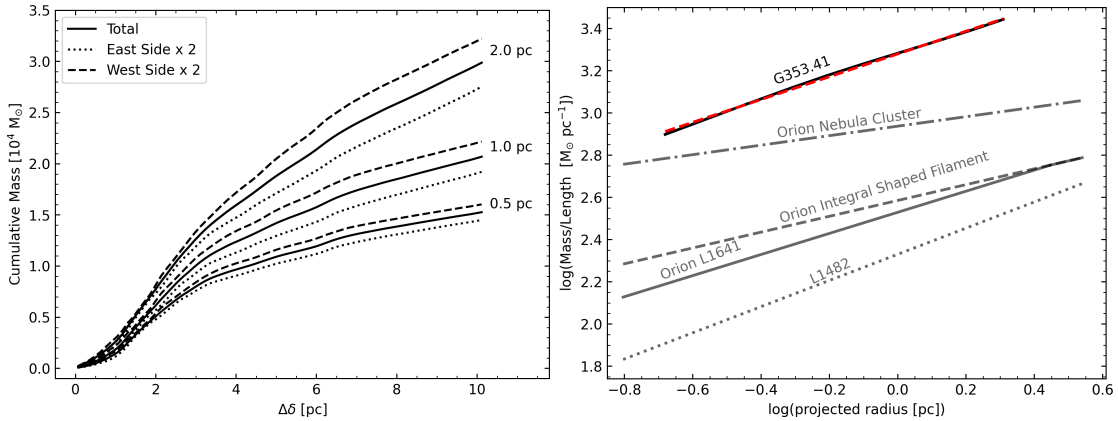

Figure 4.9: **Left:** Cumulative mass distribution of the parent filament of G353. We see symmetry in the directions along and perpendicular to the filament. **Right:** M/L distribution of the parent filament of G353 (in black) and the fitted profile (in red). The obtained M/L distribution is presented in Eq.4.1.

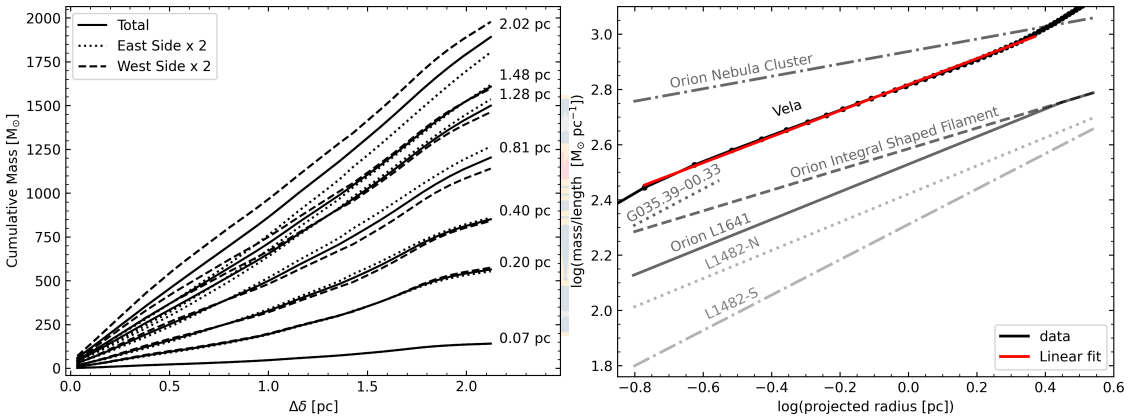

Figure 4.10: Cumulative (left) and M/L (right) profiles of Vela. The derived M/L profile is presented in Eq. 4.2. These are the equivalent diagrams from Fig. 4.9 derived using Vela data.

(Eq. 4.2). We present these estimated M/L profiles in Fig. 4.11 along with other Galactic filaments. We note here that active star forming regions are located at the middle of the diagram, while more dormant filaments are located at the top and bottom. This feature might indicate that these dormant filaments are in the early stages of star formation, where they have not reached high enough densities to trigger active star formation (i.e., L1482). For the G353 filament it is possible that its inefficient star formation rate it mostly dependent of phenomena such as magnetic fields, where despite its high density, external forces halt further gravitational collapse and fragmentation. We suggest that as these dormant structures evolve, their M/L profiles should move towards the center of this diagram, where the profiles of Vela and Orion are located. In time the M/L profile of these two active regions should decrease as its gas is depleted collapsing into cores and stars.

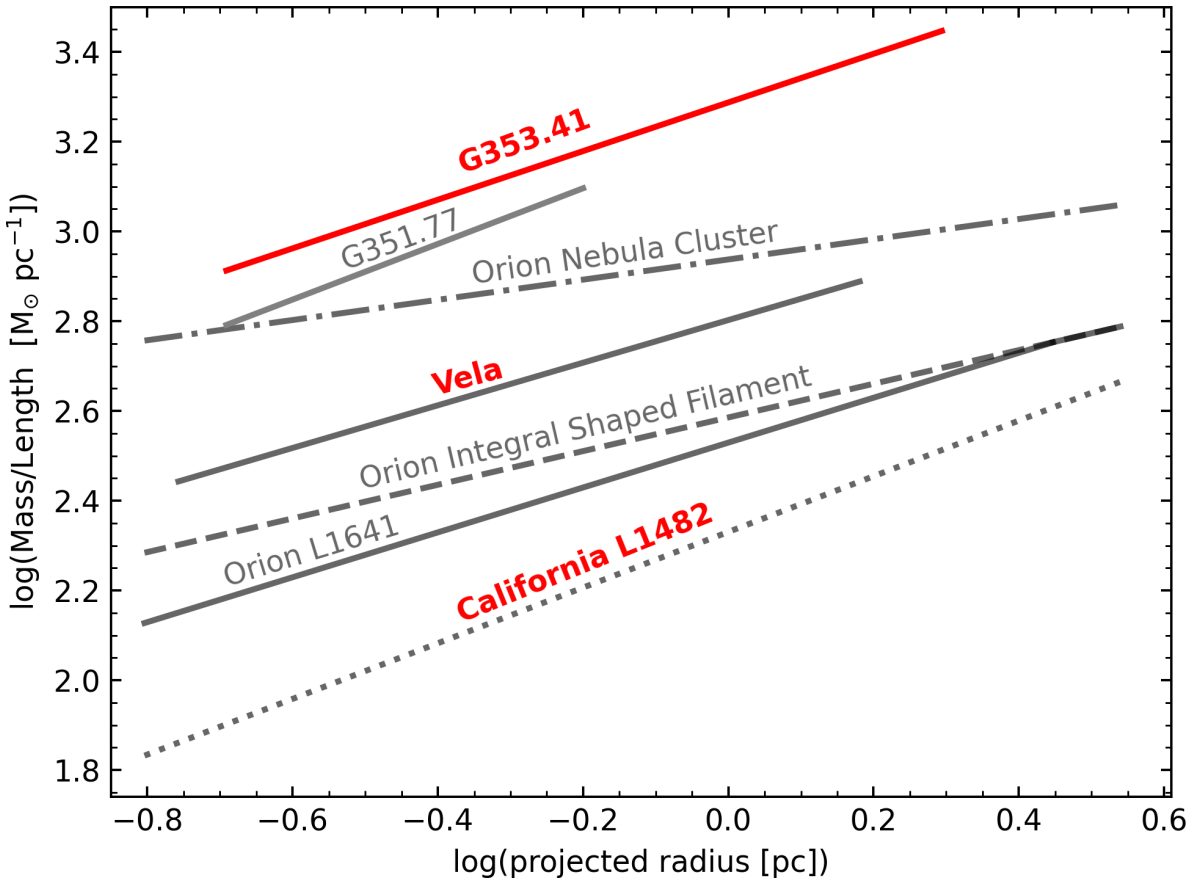

Figure 4.11: M/L profiles of multiple Galactic star forming filaments. In red we highlight the three main regions studied in this thesis. We include the M/L profile of G351 presented in Reyes-Reyes et al. (2024). Figure adapted from Álvarez-Gutiérrez et al. (2021).

Chapter 5

Summary and conclusions

In this thesis we presented the different projects carried out during my PhD program. We started by imaging the 15 ALMA-IMF Large Program regions in the N_2H^+ (1-0) transition (Motte et al., 2022). This LP contains a multitude of line transitions at 1 and 3 mm using Total Power and the arrays, probing the kinematics and continuum emission of massive ($[2.5 - 33] \times 10^3\,M_\odot$) Galactic protoclusters. For this imaging we combined the 7m and 12m observations first using the ALMA-IMF public pipeline. After removing the continuum from these results we combined these data with Total Power by feathering them, in order to recover the emission at large scales. This procedure fixed or improved the "negative bowls" present in some spectra at the V_{LSR} of the clouds. This data will be publicly available in Stutz et al. (in prep).

After the imaging presented above we focus on characterizing the complex dense gas kinematics of G353 using N_2H^+ ALMA-IMF LP observations. This region is classified as intermediate by Motte et al. (2022), with a mass of $2.5 \times 10^3\,M_\odot$ at a distance of 2 kpc. The data used in this project mainly consist of the fully combined N_2H^+ data cube. We also include 1.3 mm continuum cores and DCN cores velocity catalogs, SiO 12 m observations, and a $N(H_2)$ 1.3 mm continuum-derived map. We summarize the main results of this main project below.

- With our N_2H^+ isolated component modeling, we find that most of the 1.3 mm cores are located in regions with two to three velocity components. This indicates kinematic complexity down to $\sim$4 kau scales.

- We increase the number of cores with a V_{LSR} estimate in this region by further examining the DCN emission and comparing it with the N_2H^+ data extracted toward the core positions. We find that 11 cores that were previously undetected in the in the DCN background-subtracted fitting from Cunningham et al. (2023) are identified with our method. With this approach we increase our core velocities sample from 15 to 26, accounting for $\sim$ 58% of the total 45 1.3 mm continuum cores. These are presented in Table C.1.

- We show that the traditional PV diagram highlights large, protocluster scale kinematics. In contrast, the intensity-weighted PV diagram allows us access to the small, core scale dynamics

(see Figs. 3.8 & 3.9).

- From the PV diagrams, we see the DCN core velocities are in agreement with the N_2H^+ velocity distribution (within a few DCN channel widths). This suggests coupling between the cores and the dense gas in which they formed.

- In the intensity-weighted PVs we see clear V-shaped velocity structures, composed by two linear VGs converging into a common point. These VGs are present across all N_2H^+ velocity components. Some of them are near the location of cores in both position and velocity (see § 3.5.2)

- We successfully characterize nine V-shaped VGs well detected in our N_2H^+ data (see Figs. 3.13 & D.2). These structures are located mostly at the center of the protocluster, where three filaments converge.

- V-shape "C" (see Fig. 3.10, 3.11, and 3.12) is the most prominent across our sample. It is centered between cores 2 & 3, two of the most massive cores in this region.

- We estimate the barycenter of cores 2 & 3, presenting an offset relative to the center of the V-shape of $\sim 0.3''(\sim 600\,\mathrm{au})$ well below the beam size of our N_2H^+ data.

- For V-shape "B" we find that core "7", with a mass of $6\,M_\odot$, is located within a ∼beam size from its apex.

- We suggest that the dense gas is flowing along the filament, producing the V-shaped structure toward the derived barycenter.

- We characterize the VGs composing our sample of V-shapes by applying linear fits to these distributions. We estimate timescales associated with the VGs as $t_{VG} = \mathrm{VG}^{-1}$. These timescales are between ∼35 to ∼170 kyr, with an average of ∼67 kyr. These values are short compared to the t_{ff} of the protocluster ($\sim 0.21\,\mathrm{Myr}$), and $\sim$ 2 times larger that the cores average t_{ff} ($\sim 32\,\mathrm{kyr}$).

- We suggest that at small scales the N_2H^+ V-shaped structures indicate gas motions along filaments, toward denser regions. Thus we interpret t_{VG} as inflow timescales.

- Using an H_2 mass map and the V-shapes mean timescales, we derive H_2 mass accretion rates of $(0.35\,\mathrm{to}\,8.77) \times 10^{-4}\ M_\odot\ \mathrm{yr}^{-1}$, consistent with previous studies on regions that present gas flows along filaments toward denser object or regions, such as protostars and clumps. Moreover, V-shapes "H", "C", "F", and "B" present the largest $\dot{M}_{\rm in}$ (H_2) and they are located near or at the convergence point of the filaments (see Fig. 3.13).

- In SiO, the PV structure covers a velocity range (ΔV) of $\sim$ $80\,\mathrm{km\,s^{-1}}$, while for N_2H^+ ΔV is $\sim 8\,\mathrm{km\,s^{-1}}$. This difference suggests that N_2H^+ is tracing infall, a less energetic processes compared to SiO, a shock and outflow tracer.

- We model the protocluster as a gravitationally collapsing sphere. The derived radial velocities are consistent with the large-scale morphology of the traditional PV diagram. This agreement suggests that at large scales the G353 protocluster is undergoing gravitational contraction.

The L1482 filament is located in the California molecular cloud (CMC) at $\sim 500\,\mathrm{pc}$. The CMC along with Orion are the most massive ($\sim 10^5\,\mathrm{M}_\odot$) and nearby Galactic molecular clouds, making them the ideal targets to study high mass star formation. Despite having similar masses, Orion present an order of magnitude more YSO content than the CMC (Lada et al., 2010). In this context Álvarez-Gutiérrez et al. (2021) characterized the mass distribution and kinematics of the north part of the L1482 filament, one of the most dense structures in the CMC, containing $\sim 60\%$ of the CMC YSO content. They suggest that filamentary rotation as well as the filament being less dense than Orion are halting star formation in the region, indicating that L1482 and California are in a younger evolutionary state compared to Orion.

During my PhD we carried out observations of the L1482 south filament using the IRAM 30m radiotelescope. We probed the same tracers as in Álvarez-Gutiérrez et al. (2021) with the exception of HNC. We also crossmatched a previous YSO catalog with Gaia DR3 and APOGEE data, in order to get the astrometry and radial velocity of these sources. We present the main results of our analysis on the L1482 filament below:

- We modeled the $C^{18}O$, HCO^+, and N_2H^+ $(1-0)$ data with Gaussian velocity components.
- $C^{18}O$ and HCO^+ data is well characterized by two velocity component spectra, while N_2H^+ present compact single component emission.
- N_2H^+ is only detected in small regions, suggesting that L1482 south has no dense material for further star formation.
- In $C^{18}O$ and HCO^+ there is a discontinuity in the filament, closely matching the location of the star cluster NGC 1579 and the lhkα 101 B star.
- This discontinuity might be the result of an early stage of the filament, where it used its gas to form the star cluster.
- In velocity space there are multiple V-shaped velocity gradients that may indicate gas flows at small scale, similarly as in Álvarez-Gutiérrez et al. (2024).
- The radial velocities provided by APOGEE show that most of the YSOs match the gas velocities traced by $C^{18}O$.
- The YSOs cluster in velocity at the location of NGC 1579, with a mean radial velocity of $\sim 2\,\mathrm{km\,s^{-1}}$.

Using the APEX 12m radiotelescope we observed the Vela region with a mass of $\sim 8\times10^4\,\mathrm{M}_\odot$ at a distance of $\sim 1\,\mathrm{pc}$. We started our coverage of the central region of Vela and after completing these observations we expanded our mapping to the south in collaboration with Friedrich Wyrowski. These

observations probe the $C^{18}O$, ^{13}CO, and ^{12}CO all $(2-1)$ transitions. We focused on analyzing the kinematics of the central region of Vela which. Our main results are:

- We modeled the $C^{18}O$ (2-1) the central filamentary region with two velocity components.
- We found that the spine of the filament is characterized by spectra with one velocity component, while at the outskirts and the south are well described by two velocity components.
- There are a few V-shaped velocity gradients along the filament, possibly indicating small scale collapse probed by small scale converging gas flows.
- At the south the filament connects to a wider region and in PV space we see a clear velocity separation between the main filament velocities and the south region.

Regarding the mass distribution of star forming regions, we looked at the parent filament of the G353 protocluster as well as the central region of Vela. Specifically I measured the M/L profile along these two massive filamentary structures. We see that G353 is the densest filament in our sample (Fig. 4.11) while Vela is located between two structures in Orion. The lack of star formation activity in the parent filament of the G353 protocluster might be an indicator of its young evolutionary state as well as external factors affecting the star formation efficiency of the region. It is important to note that Vela and Orion present active star formation as well as similar M/L. We suggest that as filaments increase their star formation activity, their M/L profiles should move towards the center of the diagram presented in Fig. 4.11.

Overall, to better understand the different processes that take place in high mass star formation it is required to replicate the kinematic analysis presented in this thesis in a multitude of Galactic star-forming regions. By increasing the sample of analyzed fields we might find correlations between evolutionary state (young, intermediate, or evolved; see Motte et al., 2022), star formation activity, cores and outflow population properties, and their velocity field. By also integrating the gas kinematics analysis with the gas mass distribution in these regions, the approaches presented here will allow us to better describe high mass star formation environments.

Chapter 6

Appendix

A Filamentary identification with FilFinder

Here we describe the procedure to identify the main filamentary structures presented in § 3.3.2 using `FilFinder` (Koch & Rosolowsky, 2015).

For this approach we used the moment 0 map of the extracted N_2H^+ isolated components that present a S/N ≥ 5. To estimate the moment 0 map we used the `moment` task from the `SpectralCube` Python package, within the velocity range of $-31.5\,\mathrm{km\,s^{-1}}$ to $0\,\mathrm{km\,s^{-1}}$. As part of the pre-processing of the moment 0 map before the filamentary detection, we decreased the contrast in the image by using the `preprocess_image` task and its argument `flatten_percent` set to 90. Now, in order to indicate to `FilFinder` the area in which to identify filaments, we used the subtask `create_mask` with the following parameters: `glob_thresh:` $4.5\,\mathrm{K\,km\,s^{-1}}$, `size_thresh:` $0.25\,\mathrm{pc}^2$, `smooth_size:` $0.12\,\mathrm{pc}$, `border_masking: False`, `fill_hole_size:` $0.013\,\mathrm{pc}^2$. The resulting mask is presented in Fig. A.1 with a white contour.

Then, we obtained the skeletons of the mask by using `medskel`. The derived structures are presented with red and green lines in Fig. A.1. Given we are only interested in the large-scale filaments, we used `analyze_skeletons` in order to "prune" the small-scale structures.For this pruning we used `branch_thresh:` $0.3\,\mathrm{pc}$, `prune_criteria: 'length'`, `max_prune_iter: 0`. This approach results in removing the small filaments (red lines in Fig. A.1) from the original skeleton and to obtain the main filamentary structure in G353 (green lines in Fig. A.1).

B Examples of the isolated components fitting

In § 3.3.1 we decomposed the multiple isolated component emission using `PySpecKit`. In Fig. B.1 we present the results of the Gaussian fitting for the high S/N spectra shown in Fig. 3.3 (panels c, e, and f).

C DCN and N_2H^+ derived core velocity

In Table C.1 we provide the 1.3 mm core velocities obtained from DCN & N_2H^+ data (see § 3.4.2), complementing the published DCN core velocities catalog from Cunningham et al. (2023). In the last column we indicate the number of N_2H^+ velocity components detected in these cores.

D V-shaped structures

In § 3.5.3 we characterized the most prominent V-shaped structure we detect in Fig. 3.9. We repeated this process for the other eight different V-shaped structures, including the linear fits to the velocity gradients. In Fig. D.1 we indicate the V-shapes location in PV space with dark points, arrows, and

their IDs. In Fig. D.2 we present individual close-ups for each V-shape. In Table D.1 we list their VGs, timescales, H_2 masses, and mass accretion rates.

Here we list a few clarifications due to projection effects seen in these V-shaped structures:

- In position-position space, only V-shape "B" presents a core within a ∼beam size from its apex. This continuum core, core "7", has a mass of $\sim 6\,M_\odot$.
- For V-shape "A", the 1.3 mm core with DCN single velocity component, located at the apex of this V-shape, is not spatially related with it.
- In V-shapes "G" and "H" we see the same 1.3 mm cores with N_2H^+ velocities. These V-shapes are not the same distribution. They are overlapped in PV space and spatially separated by $\sim 10''$.
- We improve the clarity of V-shape "B" by rotating the data in PP space by 80ounter-clockwise. We apply this process for V-shapes "E", "G", and "H" with an angle of 33lockwise.
- V-shapes G and H overlap in PV space but these are structures spatially separated.

E SiO Intensity-weighted position-velocity diagram

To create the SiO intensity-weighted PV diagram, first, we removed most of the noisy spectra by considering data with S/N $\geq$ 2.5. Then, we estimated the integrated intensity and velocity centroid at each pixel. We found improvements in our cleaning by using only spectra with integrated intensity $\geq$ 4 K km s^{-1}. Using the coordinate, integrated-intensity, and velocity centroid of each spectrum, we create the SiO intensity-weighted PV diagrams we show in E.1.

F G353 power law density profile

Here we provide the derivation of the density profile used for the gravitationally collapsing sphere. We assumed a power law density profile defined as:

$$\rho(r) \quad = \quad \rho_0 \left(\frac{r}{\mathrm{pc}}\right)^{-\gamma}, \tag{F.1}$$

in which $\gamma = 5.65$ provides a good fit to the edges of the PV distribution seen in Fig. 3.8.

To determine the value of ρ_0, we integrated this expression in a sphere (Eq. F.2), with $r_{min} < r < 0.5$ pc. Based on different tests, probing total masses from $50 - 10^3\,M_\odot$ and γ values from $2 - 6$, we set the total mass of the sphere to $150\,M_\odot$. We defined $r_{min} \sim 0.007$ pc which

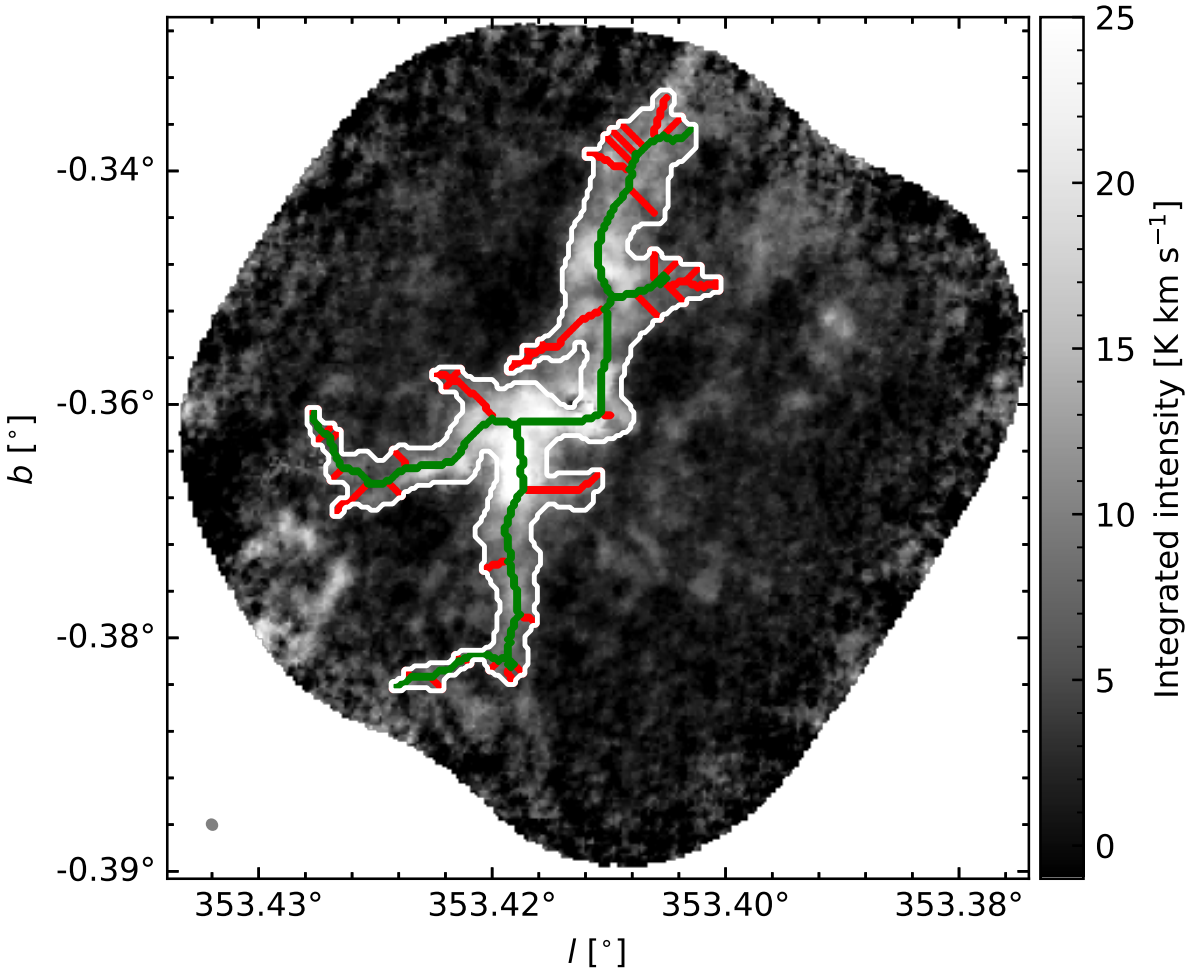

Figure A.1: `FilFinder` filamentary identification. The background indicates the moment 0 map of the extracted N_2H^+ isolated components. The white contour shows the area where `FilFinder` identifies multiple filamentary structures (red and green lines). We remove the small-scale structures (in red) by "pruning" the skeleton structure from `medskel`, obtaining the main filaments of G353. We represent these filaments with green lines.

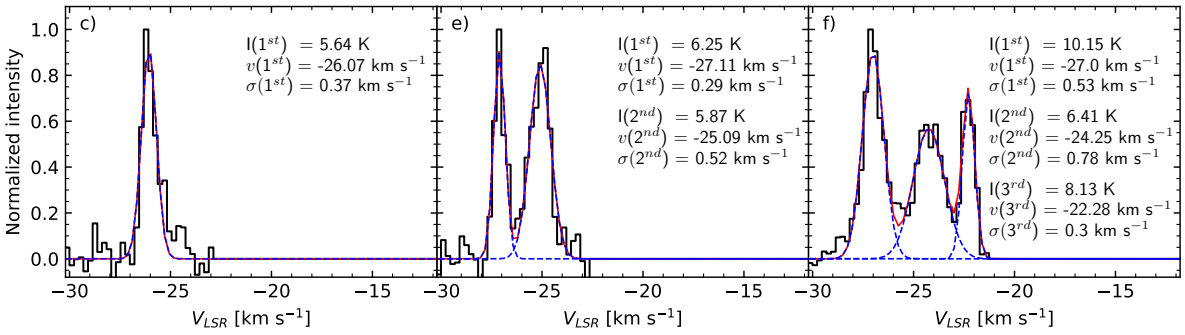

Figure B.1: Gaussian velocity fits of the extracted N_2H^+ isolated components. In black we show the high S/N isolated components from panels c), e), and f) in Fig. 3.3. The individual Gaussian components and the obtained model are represented with dashed blue and solid red lines, respectively. On the right side of each panel we indicate the peak intensity (I), the velocity centroid (v), and velocity dispersion (σ) of each Gaussian component. The notations 1^{st}, 2^{nd}, and 3^{rd} indicate the Gaussian velocity components from left to right.

corresponds to the pixel size of the N_2H^+ data at a distance of 2 kpc.

$$M_{enc}(r = 0.5 \text{ pc}) = 4\pi\rho_0 \int_{r_{min}}^{0.5\,\text{pc}} \left(\frac{r}{\text{pc}}\right)^{-\gamma} r^2 dr \tag{F.2}$$

$$= 4\pi\rho_0 \frac{r^{3-\gamma}}{3-\gamma}\Bigg|_{r\,=\,r_{min}}^{r\,=\,0.5\text{ pc}} \text{pc}^{\gamma} \tag{F.3}$$

$$= \frac{4\pi\rho_0}{3-\gamma}(0.5^{3-\gamma} - {r_{min}}^{3-\gamma})\ \text{pc}^{\gamma}, \tag{F.4}$$

in which $M_{enc}(r = 0.5\,\text{pc}) = 150\ \text{M}_\odot$, $r_{min} = 7 \times 10^{-3}\,\text{pc}$, and $\gamma = 5.65$, from Eq. F.4, we obtained:

$$\rightarrow \rho_0 = 6.1 \times 10^{-5} \frac{\text{M}_\odot}{\text{pc}^3}. \tag{F.5}$$

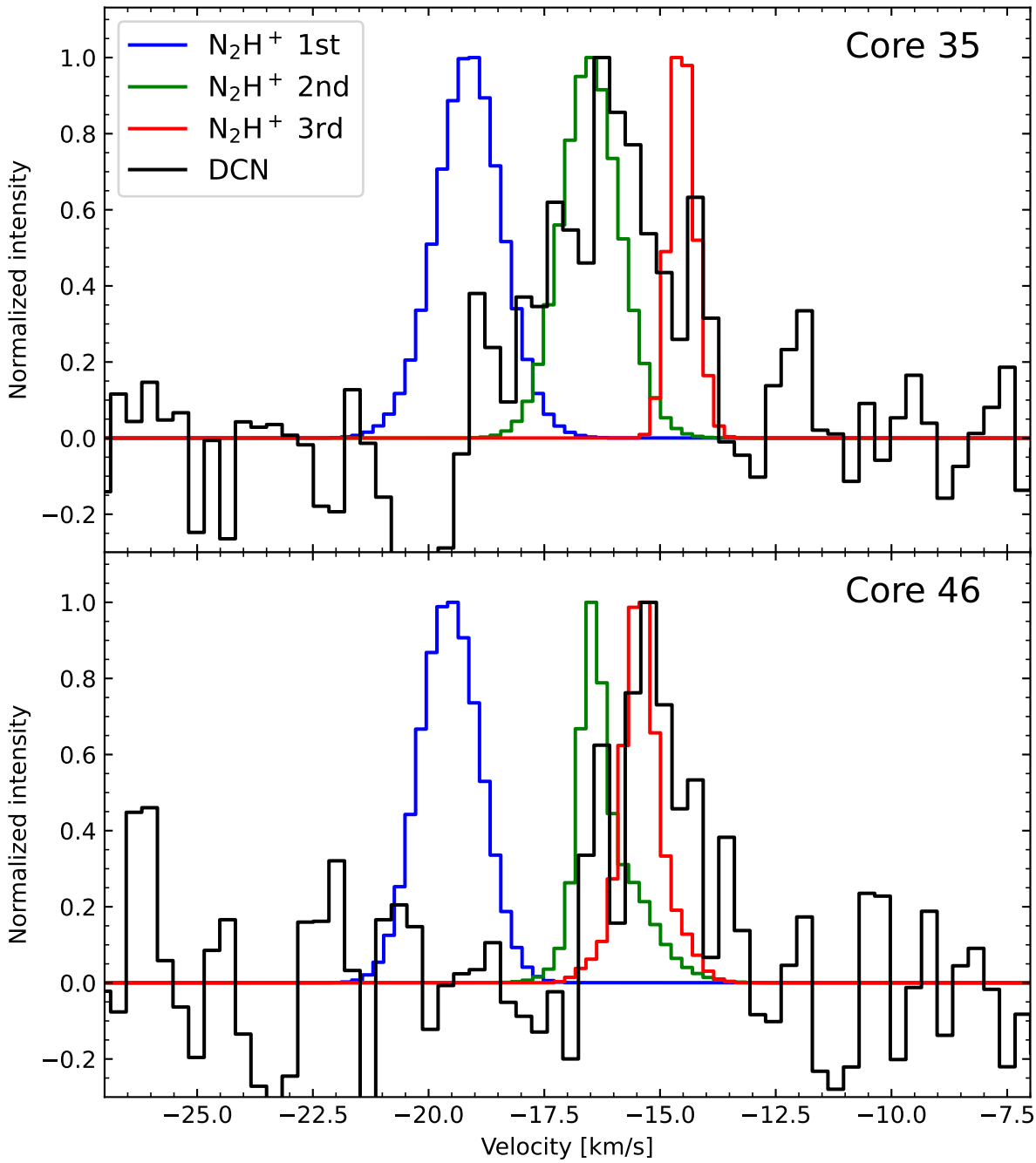

Figure C.1: DCN and N_2H^+ normalized mean spectrum of cores 35 (top) and 46 (bottom). We show the multiple N_2H^+ isolated velocity components with blue, red, and green colors. We present the DCN emission in black. We see a match between the DCN emission and one of the N_2H^+ velocity components. We determine the N_2H^+ velocity for 11 cores with no DCN velocity fits. These are listed in Table C.1.

Table C.1: 1.3 mm core catalog of DCN & N_2H^+ velocities.

Core Number	RA [°]	DEC [°]	F_A [″]	F_B [″]	PA [°]	Mass [$M_\odot$]	V_{LSR} [km s^{-1}]	Type	Number of N_2H^+ components
2	262.6165032	-34.6955865	1.98	1.59	64.00	20.7	-20.450 ± 0.065	DCN, Single	2
3	262.6184156	-34.6965240	2.59	1.79	146.00	9.4	-16.480 ± 0.040	DCN, Single	2
4	262.6103159	-34.6932659	1.56	1.46	104.00	5.2	-16.530 ± 0.155	DCN, Single	3
5	262.6101515	-34.6960014	2.03	1.75	79.00	16.0	-16.940 ± 0.087	DCN, Single	3
6	262.6049155	-34.6934384	1.60	1.48	129.00	4.9	-18.680 ± 0.126	DCN, Single	2
7	262.6137738	-34.6947298	1.63	1.27	80.99	6.0	-19.79	DCN & N_2H^+	3
8	262.6039531	-34.6936374	2.26	1.56	97.32	6.6	—	—	—
9	262.6192359	-34.6903650	2.69	1.96	62.96	3.7	-16.09	DCN & N_2H^+	3
11	262.6243189	-34.6880780	2.12	1.95	172.70	2.8	-16.09	DCN & N_2H^+	3
12	262.6072148	-34.6969795	2.98	2.02	86.00	10.3	-17.830 ± 0.019	DCN, Single	3
13	262.6078228	-34.6996836	1.91	1.48	153.90	2.7	—	—	—
14	262.6147937	-34.6946762	2.00	1.58	124.00	6.2	-14.360 ± 0.090	DCN, Single	3
15	262.6107433	-34.6964412	1.96	1.59	93.00	6.6	-14.780 ± 0.087	DCN, Complex	—
16	262.6215941	-34.6989408	2.68	2.49	19.37	1.5	—	—	—
17	262.5954514	-34.6916168	1.57	1.42	87.50	0.9	—	—	—
18	262.5927434	-34.7052494	1.97	1.56	89.26	0.8	—	—	—
19	262.6064012	-34.7019756	1.55	1.20	57.74	0.5	—	—	—
20	262.6111096	-34.6932787	1.67	1.63	178.00	1.3	—	—	—
21	262.6131910	-34.6939495	2.10	1.48	108.00	2.4	-18.560 ± 0.063	DCN, Single	3
22	262.6118441	-34.6946150	1.89	1.59	96.65	1.7	-16.76	DCN & N_2H^+	3
23	262.6028175	-34.6925438	1.84	1.31	112.70	0.8	—	—	—
24	262.6198349	-34.6960383	1.88	1.72	76.00	0.8	-19.500 ± 0.089	DCN, Single	2
25	262.6155222	-34.6952591	1.87	1.20	137.30	2.5	-18.78	DCN & N_2H^+	2
26	262.6143434	-34.6917027	1.49	1.24	137.30	0.8	—	—	—
27	262.6000802	-34.6910324	3.39	2.51	48.16	1.8	—	—	—
28	262.6253977	-34.6999713	2.56	1.87	39.31	0.8	—	—	—
29	262.6133074	-34.6919187	1.67	1.26	76.67	0.7	—	—	—
30	262.6114686	-34.6962602	1.52	1.41	30.00	2.3	-12.810 ± 0.074	DCN, Single	2
31	262.6096651	-34.6925680	1.72	1.34	119.10	0.7	—	—	—
32	262.6094126	-34.6910985	2.44	2.02	59.22	2.0	—	—	—
33	262.6287106	-34.6862068	2.32	2.00	16.64	1.7	—	—	—
34	262.5982914	-34.6919006	1.81	1.36	139.00	0.8	-18.770 ± 0.080	DCN, Single	2
35	262.6142011	-34.6940134	2.31	1.81	111.00	3.4	-16.09	DCN & N_2H^+	3
36	262.6202758	-34.7001995	2.19	1.88	141.00	0.8	—	—	—
37	262.6010398	-34.6950114	1.74	1.33	75.00	0.8	-17.830 ± 0.053	DCN, Single	3
38	262.5971034	-34.6920396	2.01	1.61	104.80	0.7	—	—	—
39	262.6054437	-34.6963773	2.05	1.88	158.50	1.4	-16.43	DCN & N_2H^+	3
40	262.5917454	-34.6897316	1.85	1.50	92.93	0.6	—	—	—
41	262.6095777	-34.6983259	2.23	1.83	72.51	1.3	—	—	—
42	262.5975992	-34.6876666	1.51	1.22	24.46	0.3	—	—	—
43	262.6035166	-34.6966807	2.48	1.78	95.00	1.2	-17.330 ± 0.062	DCN, Single	3
44	262.6030115	-34.6956424	1.76	1.55	96.00	0.5	-16.990 ± 0.091	DCN, Single	3
45	262.6143008	-34.6909376	3.40	2.75	94.93	2.6	—	—	—
46	262.6187648	-34.6912377	3.10	2.15	40.67	0.9	-15.08	DCN & N_2H^+	3
47	262.6178453	-34.6919943	3.09	2.48	45.43	1.6	—	—	—

Table D.1: Characterized V-shaped structures.

V-shape ID	l [°]	b [°]	$M(H_2)$ [$M_\odot$]	Upper / lower VG [km s^{-1} pc^{-1}]	Mean VG [km s^{-1} pc^{-1}]	Upper / lower t_{VG} [kyr]	$t_{VG\ mean}$ [kyr]	$\dot{M}_{in}(H_2)$ [10^{-4} $M_\odot$ yr^{-1}]
A	353.3981	-0.3506	8.13	20.85 / 17.04	18.95	46.89 / 57.39	52.14	1.56
B	353.4127	-0.3632	13.29	25.34 / 17.22	21.28	38.59 / 56.77	47.68	2.79
C	353.4135	-0.3657	53.02	17.69 / 13.26	15.48	55.28 / 73.75	64.52	8.22
D	353.4133	-0.3727	7.96	12.85 / 21.22	17.15	76.07 / 46.07	61.07	1.31
E	353.4096	-0.3521	6.27	12.47 / 3.63	8.05	78.38 / 269.57	173.98	0.36
F	353.4128	-0.3604	27.24	15.75 / 15.61	15.68	62.09 / 62.64	62.37	4.37
G	353.4110	-0.3630	3.24	22.59 / 24.46	23.53	43.29 / 39.97	41.63	0.79
H	353.4140	-0.3627	31.46	21.28 / 39.68	30.48	45.94 / 24.64	35.29	8.91
I	353.4091	-0.3595	16.13	22.34 / 11.22	16.78	43.77 / 87.17	65.47	2.46

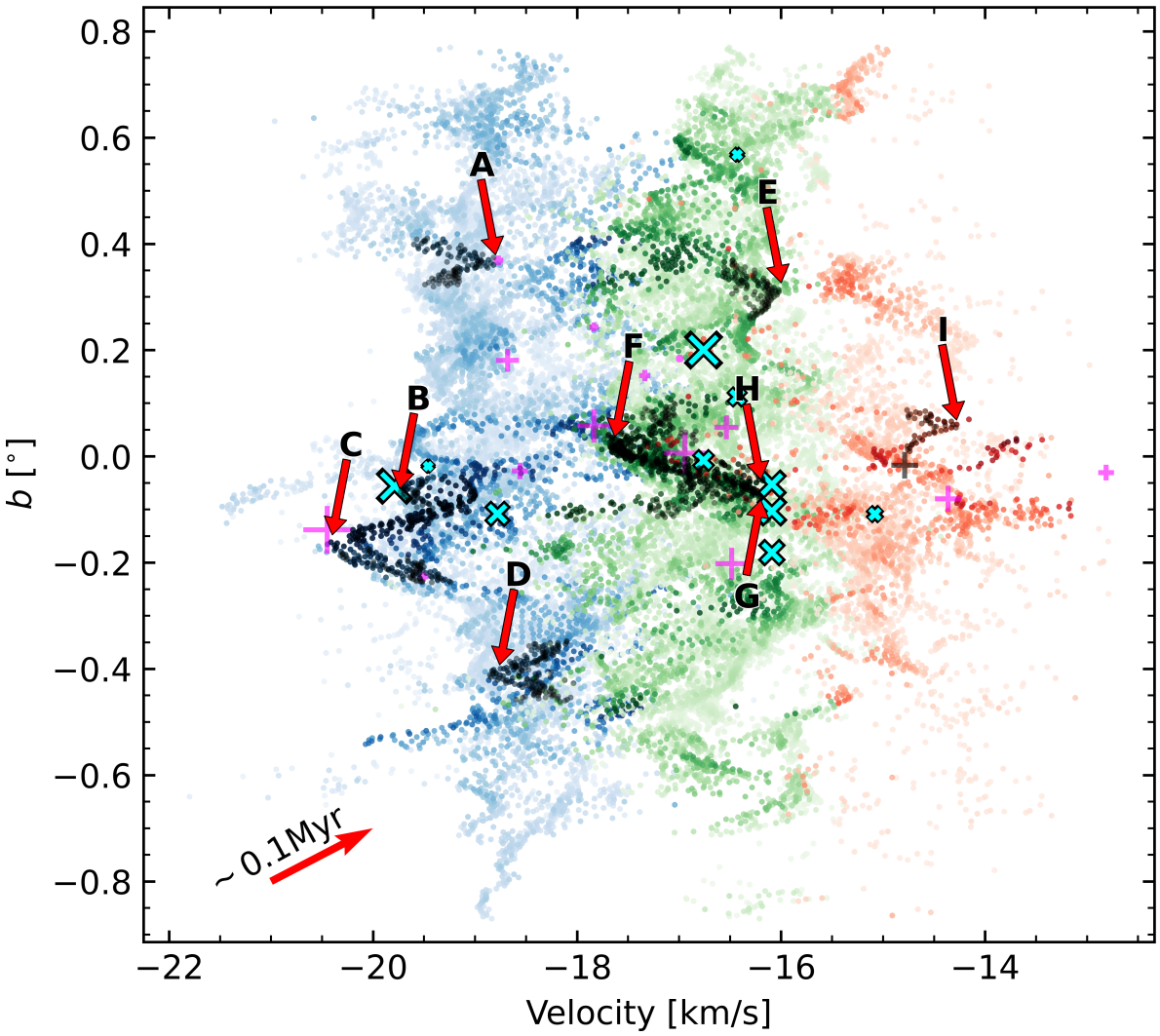

Figure D.1: V-shapes location in PV space. We highlight the V-shapes listed in Table D.1 with black points and indicate them with red arrows and their ID. The core velocities and the N_2H^+ velocity distributions follow the same definitions from the top right panel in Fig. 3.9. V-shapes G and H overlap in PV space but these structures are spatially separated (left panel).

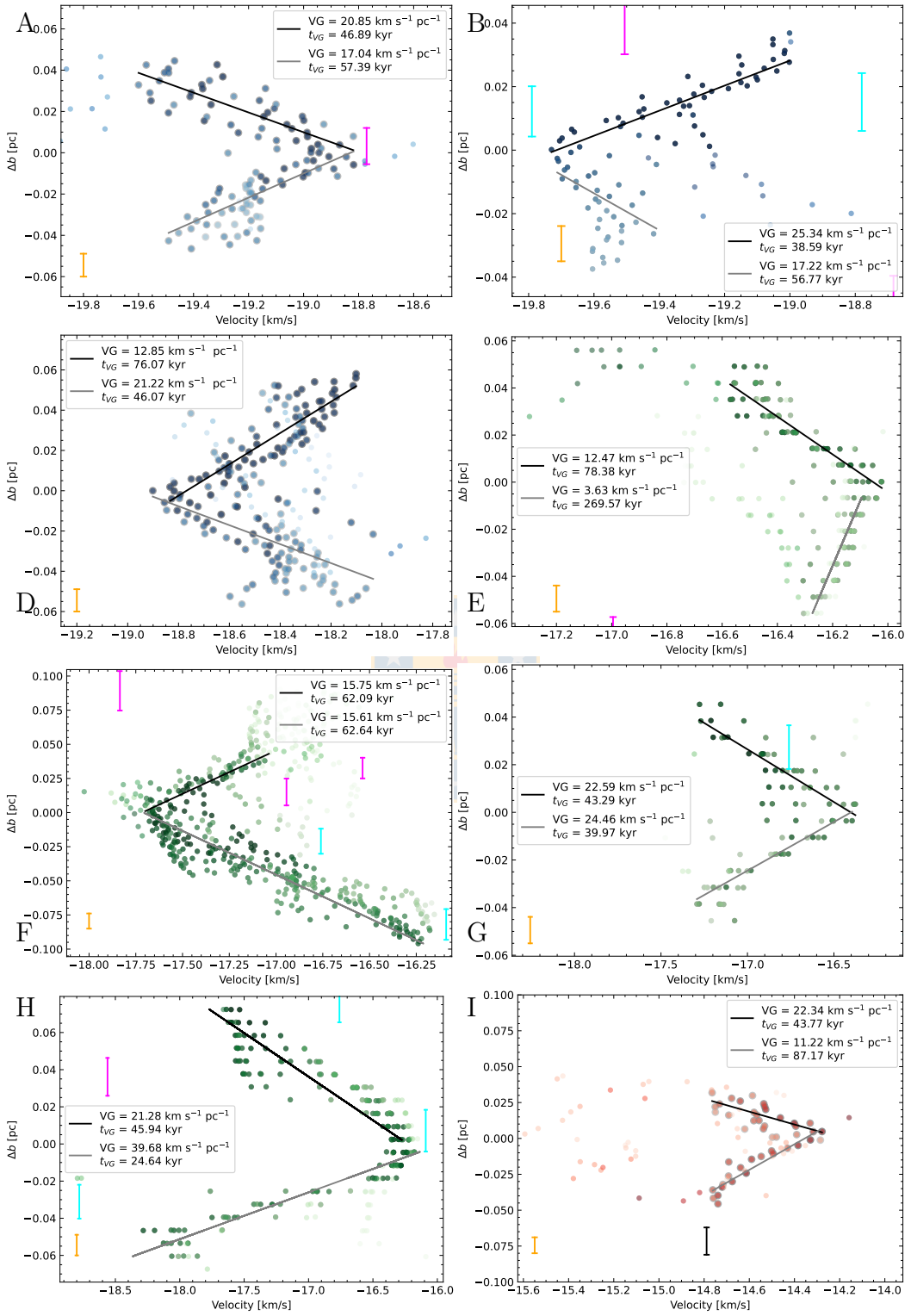

Figure D.2: V-shaped structures listed in Table D.1, with the exception of "C" shown in Fig. 3.10. We indicate the "V-shape ID" from Table D.1 at the top/bottom left corner of each plot. The colors of the distributions, DCN and DCN & N_2H^+ derived core velocities, and beam size follow the same color and marker convention from Fig. 3.9. See Appendix D for clarifications regarding projection effects on these diagrams.

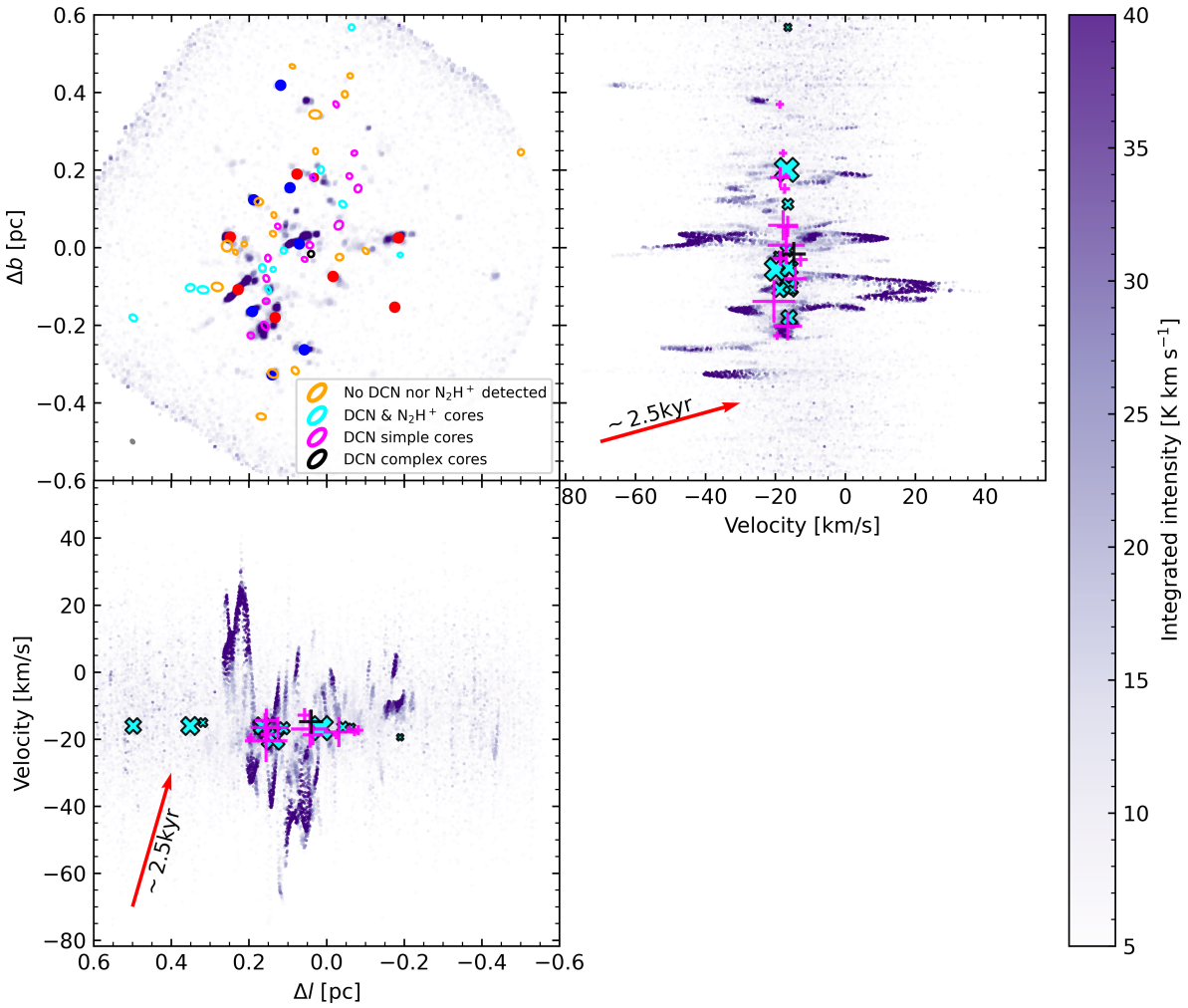

Figure E.1: ALMA-IMF 12 m SiO equivalent of Fig. 3.9 using data from Cunningham et al. (2023). For the cores, we use the same marker and color convention from Fig. 3.9. With filled blue, red, and 'red+blue' circles we represent the SiO outflow candidates (Towner et al., 2024). With red arrows we indicate a VG = 400 $\mathrm{km\,s^{-1}\,pc^{-1}}$ corresponding to a timescale t_{VG} = 2.5 kyr. The velocity range (ΔV) covered by the SiO emission is $\sim$80$\mathrm{km\,s^{-1}}$, about 10 times the velocity range traced by N_2H^+. This velocity difference suggests that SiO is tracing processes (outflows) $\sim$ 100 times more energetic (e_k = ΔV/2) than N_2H^+ (possibly infall).

Bibliography

Álvarez-Gutiérrez, R. H., Stutz, A. M., Law, C. Y., et al. 2021, ApJ, 908, 86

Álvarez-Gutiérrez, R. H., Stutz, A. M., Sandoval-Garrido, N., et al. 2024, arXiv e-prints, arXiv:2404.07363

André, P., Men'shchikov, A., Bontemps, S., et al. 2010, A&A, 518, L102

Anglada, G., Rodriguez, L. F., Canto, J., Estalella, R., & Lopez, R. 1987, A&A, 186, 280

Armante, M., Gusdorf, A., Louvet, F., et al. 2024, A&A, 686, A122

Bastian, N., Covey, K. R., & Meyer, M. R. 2010, ARA&A, 48, 339

Bergin, E. A., Alves, J., Huard, T., & Lada, C. J. 2002, ApJ, 570, L101

Bonfand, M., Csengeri, T., Bontemps, S., et al. 2024, arXiv e-prints, arXiv:2402.15023

Bonne, L., Bontemps, S., Schneider, N., et al. 2020, A&A, 644, A27

—. 2023, ApJ, 951, 39

Busquet, G., Zhang, Q., Palau, A., et al. 2013, ApJ, 764, L26

Caselli, P., Benson, P. J., Myers, P. C., & Tafalla, M. 2002a, ApJ, 572, 238

Caselli, P., Myers, P. C., & Thaddeus, P. 1995, ApJ, 455, L77

Caselli, P., Walmsley, C. M., Zucconi, A., et al. 2002b, ApJ, 565, 344

Cazzoli, G., Corbelli, G., Degli Esposti, C., & Favero, P. 1985, Chemical Physics Letters, 118, 164

Chen, H.-R. V., Zhang, Q., Wright, M. C. H., et al. 2019, ApJ, 875, 24

Csengeri, T., Bontemps, S., Schneider, N., Motte, F., & Dib, S. 2011, A&A, 527, A135

Csengeri, T., Bontemps, S., Wyrowski, F., et al. 2017, A&A, 601, A60

Cunningham, N., Lumsden, S. L., Cyganowski, C. J., Maud, L. T., & Purcell, C. 2016, MNRAS, 458, 1742

Cunningham, N., Ginsburg, A., Galván-Madrid, R., et al. 2023, A&A, 678, A194

Díaz-González, D. J., Galván-Madrid, R., Ginsburg, A., et al. 2023, ApJ, 269, 55

Fernández-López, M., Arce, H. G., Looney, L., et al. 2014, ApJ, 790, L19

Fissel, L. M., Ade, P. A. R., Angilè, F. E., et al. 2019, ApJ, 878, 110

Gaia Collaboration, Vallenari, A., Brown, A. G. A., et al. 2023, A&A, 674, A1

Galván-Madrid, R., Zhang, Q., Keto, E., et al. 2010, ApJ, 725, 17

Galván-Madrid, R., Liu, H. B., Zhang, Z. Y., et al. 2013, ApJ, 779, 121

Ginsburg, A., & Mirocha, J. 2011, PySpecKit: Python Spectroscopic Toolkit, Ver. 0.1.23, Astrophysics Source Code Library, ascl:1109.001

Ginsburg, A., Sokolov, V., de Val-Borro, M., et al. 2022a, AJ, 163, 291

Ginsburg, A., Csengeri, T., Galván-Madrid, R., et al. 2022b, A&A, 662, A9

Gómez, G. C., & Vázquez-Semadeni, E. 2014, ApJ, 791, 124

González Lobos, V., & Stutz, A. M. 2019, MNRAS, 489, 4771

Hacar, A., Tafalla, M., Forbrich, J., et al. 2018, A&A, 610, A77

Henshaw, J. D., Caselli, P., Fontani, F., Jiménez-Serra, I., & Tan, J. C. 2014, MNRAS, 440, 2860

Henshaw, J. D., Ginsburg, A., Haworth, T. J., et al. 2019, MNRAS, 485, 2457

Henshaw, J. D., Kruijssen, J. M. D., Longmore, S. N., et al. 2020, Nature Astronomy, 4, 1064

Hill, T., Motte, F., Didelon, P., et al. 2011, A&A, 533, A94

Inoue, T., & Fukui, Y. 2013, ApJ, 774, L31

Inoue, T., Hennebelle, P., Fukui, Y., et al. 2018, PASJ, 70, S53

Koch, E. W., & Rosolowsky, E. W. 2015, MNRAS, 452, 3435

Kumar, M. S. N., Arzoumanian, D., Men'shchikov, A., et al. 2022, A&A, 658, A114

Kuznetsova, A., Hartmann, L., & Ballesteros-Paredes, J. 2015, ApJ, 815, 27

—. 2018, MNRAS, 473, 2372

Lada, C. J., Lewis, J. A., Lombardi, M., & Alves, J. 2017, A&A, 606, A100

Lada, C. J., Lombardi, M., & Alves, J. F. 2010, ApJ, 724, 687

Lee, C. W., Myers, P. C., & Tafalla, M. 1999, ApJ, 526, 788

—. 2001, ApJ, 136, 703

Lippok, N., Launhardt, R., Semenov, D., et al. 2013, A&A, 560, A41

Liu, H. B., Galván-Madrid, R., Jiménez-Serra, I., et al. 2015, ApJ, 804, 37

Liu, H.-L., Stutz, A., & Yuan, J.-H. 2019, MNRAS, 487, 1259

Liu, T., Evans, N. J., Kim, K.-T., et al. 2020a, MNRAS, 496, 2790

—. 2020b, MNRAS, 496, 2790

Louvet, F., Sanhueza, P., Stutz, A., et al. 2023, A&A, submitted

Majewski, S. R., Schiavon, R. P., Frinchaboy, P. M., et al. 2017, AJ, 154, 94

Mardones, D., Myers, P. C., Tafalla, M., et al. 1997, ApJ, 489, 719

Men'shchikov, A. 2021, A&A, 649, A89

Minh, Y. C., Liu, H. B., Galvań-Madrid, R., et al. 2018, ApJ, 864, 102

Miville-Deschênes, M.-A., Murray, N., & Lee, E. J. 2017, ApJ, 834, 57

Motte, F., Bontemps, S., & Louvet, F. 2018, ARA&A, 56, 41

Motte, F., Bontemps, S., Csengeri, T., et al. 2022, A&A, 662, A8

Myers, P. C. 2009, ApJ, 700, 1609

Nony, T., Galván-Madrid, R., Motte, F., et al. 2023, A&A, 674, A75

Offner, S. S. R., Clark, P. C., Hennebelle, P., et al. 2014, in Protostars and Planets VI, ed. H. Beuther, R. S. Klessen, C. P. Dullemond, & T. Henning, 53–75

Olguin, F. A., Sanhueza, P., Chen, H.-R. V., et al. 2023, ApJ, 959, L31

Pan, S., Liu, H.-L., & Qin, S.-L. 2024, ApJ, 960, 76

Peretto, N., Rigby, A. J., Louvet, F., et al. 2023, MNRAS, 525, 2935

Peretto, N., Fuller, G. A., André, P., et al. 2014, A&A, 561, A83

Pouteau, Y., Motte, F., Nony, T., et al. 2023, A&A, 674, A76

Rawat, V., Samal, M. R., Walker, D. L., et al. 2024, MNRAS, 528, 2199

Redaelli, E., Bovino, S., Sanhueza, P., et al. 2022, ApJ, 936, 169

Reid, M. J., Menten, K. M., Zheng, X. W., et al. 2009, ApJ, 700, 137

Reyes-Reyes, S. D., Stutz, A. M., Megeath, S. T., et al. 2024, MNRAS, 529, 2220

Sanhueza, P., Contreras, Y., Wu, B., et al. 2019, ApJ, 886, 102

Sanhueza, P., Girart, J. M., Padovani, M., et al. 2021, ApJ, 915, L10

Schuller, F., Menten, K. M., Contreras, Y., et al. 2009, A&A, 504, 415

Smith, R. J., Shetty, R., Stutz, A. M., & Klessen, R. S. 2012, ApJ, 750, 64

Soler, J. D. 2019, A&A, 629, A96

Storm, S., Mundy, L. G., Fernández-López, M., et al. 2014, ApJ, 794, 165

Stutz, A. M. 2018, MNRAS, 473, 4890

Stutz, A. M., Gonzalez-Lobos, V. I., & Gould, A. 2018, arXiv e-prints, arXiv:1807.11496

Stutz, A. M., & Gould, A. 2016, A&A, 590, A2

Stutz, A. M., & Kainulainen, J. 2015, A&A, 577, L6

Tafalla, M., Myers, P. C., Caselli, P., & Walmsley, C. M. 2004, A&A, 416, 191

Tafalla, M., Usero, A., & Hacar, A. 2021, A&A, 646, A97

Tobin, J. J., Hartmann, L., Bergin, E., et al. 2012, ApJ, 748, 16

Towner, A. P. M., Ginsburg, A., Dell'Ova, P., et al. 2024, ApJ, 960, 48

Ungerechts, H., Bergin, E. A., Goldsmith, P. F., et al. 1997, ApJ, 482, 245

Zhou, J.-W., Liu, T., Evans, N. J., et al. 2022, MNRAS, 514, 6038

Zhou, J. W., Wyrowski, F., Neupane, S., et al. 2023, A&A, 676, A69